NORTHWESTERN UNIVERSITY

Mechanoacoustic Sensing at Suprasternal Notch

A DISSERTATION

SUBMITTED TO THE GRADUATE SCHOOL

IN PARTIAL FULFILLMENT OF THE REQUIRMENTS

for the degree

DOCTOR OF PHILOSOPHY

Materials Science and Engineering

By

Kun Hyuck Lee

EVANSTON, ILLINOIS

June 2021

ABSTRACT

Mechanoacoustic Sensing at Suprasternal Notch

Kun Hyuck Lee

Advanced wireless soft electronics integrate a wireless power transfer circuit and a small battery. It is skin-compliant, and lightweight accommodating the complex motion of the body. These unique features of the device provide a continuous physiological measurement without discomfort and spatial constraints. Using the device, we can observe and track the progression of the recoveries, development of diseases, and state of the sleep. Here, we demonstrate the design consideration and strategies for developing advance wireless soft electronics through wireless mechanoacoustic sensors. The sensor conforms to the skin surface of the suprasternal notch for the continuous measurement of mechanical and acoustic signals. We also show the impact of advanced soft electronics through its applications in a sleep study, stroke rehabilitation, and COVID-19 tracking.

ACKNOWLEDGMENT

I want to thank my research advisor and life mentor, Professor Rogers, for exposing me to many real-world problems and providing me a playground with bottomless resources to explore for most creative solutions that directly impact the community of today.

I also want to thank Samsung Scholarship for the financial support and the network that I have made in the past five years with many talented friends and researchers worldwide.

Finally, I want to thank my parents and the Dion family for giving me an abundance of love and support. With their help, I was fortunate enough to be in the right place at the right time to take the opportunities that are more than what I have deserved.

TABLE OF CONTENTS:

LIST OF FIGURES:

1. Introduction

The current biomedical device, with its rigid mechanical property, and bulky form factor with wires, limits its location of the operation to clinical settings (Fig. 1). This limitation inflicts episodical monitoring of patient's health and practice of care that misses many critical time points in the progression of the disease. However, many of the chronic diseases could have been avoided or delayed by preventative care.

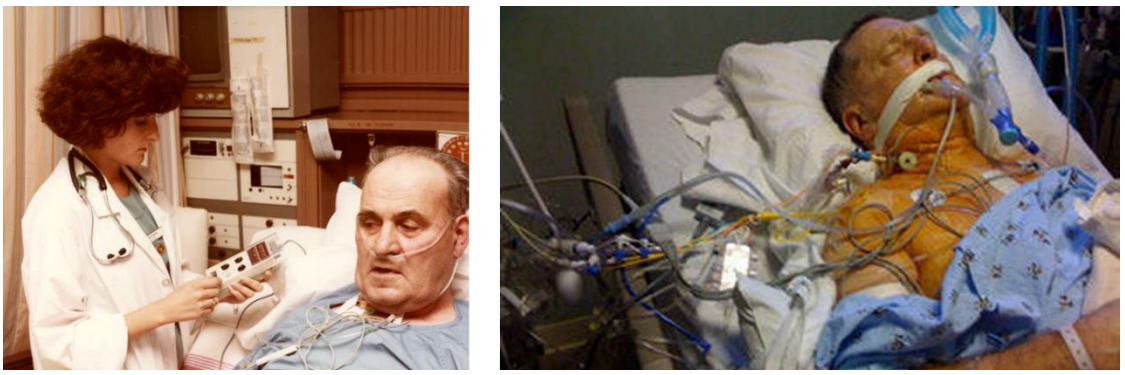

Fig. 1 | Pictures of patients in different hospital settings sharing many similarities. Patients are lying on the hospital bed, tethered to wires and hooked up to bulky instruments. Picture on the left is the look of ICU in 1975 [image from HSC Archives] and picture on the right is the look of ICU in today [image from Intensive Care Hotline].

This study demonstrates the method of translating the flexible skin-surface electronics or epidermal electronics technology into the biomedical sensor suited for clinical settings. With its flexible mechanics and wireless system, the sensor allows continuous monitoring without any spatial constraints, provides a rich set of information that has not been observable by the current medical device technology.

I. Skin Mechanics

The epidermal electronics directly interacts with the skin surface to measure the physiological signal noninvasively. Therefore first, we need to understand the skin mechanics to set our design reference clear.

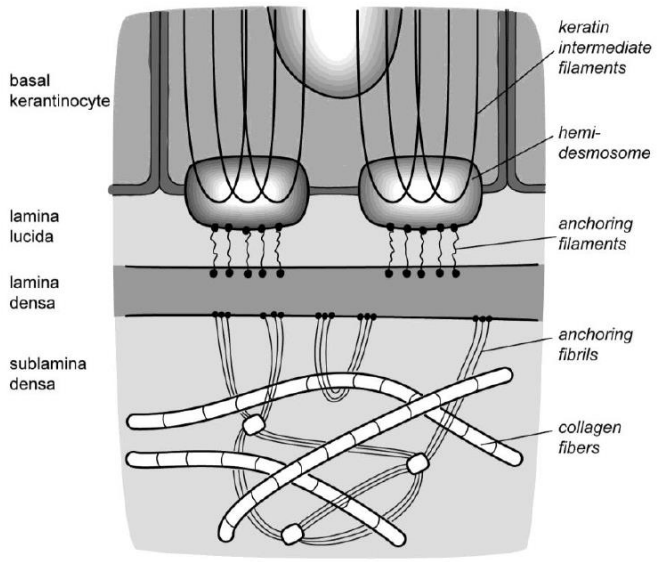

Fig. 2 | Skin's composite-like cell structure. It consists collagen fibers and other filaments functioning as fillers, and fibroblast functioning as matrix. In sum, they provide the viscoelastic nature of skin mechanics

Skin is one of the largest organs in the body in a surface area[1], providing the body with overall protection from many environmental factors. It consists of multiple layers; epidermis, dermal-epidermal junction, dermis, and hypodermis. Each of the layers has unique structures formed by different cell structures resulting in a specific mechanical property (Fig. 2). Together, it becomes a composite material that has the viscoelastic property necessary for skins to bind sophisticated motion, along with high resilience that protects the internal tissues from a wide range of external mechanical input.

The viscoelastic nature of the skin shows a nonlinear response to different mechanical loads (Fig. 3). Also, its specific mechanical property varies depending on the location of the skin and its hydration level. There is not an absolute value for the skin's mechanical property. Therefore, we focused on the skin property of the mounting locations (neck and chest), and specifically in the linear elastic phase. It has young's modulus of 130kPa and can deform 10% elastically.

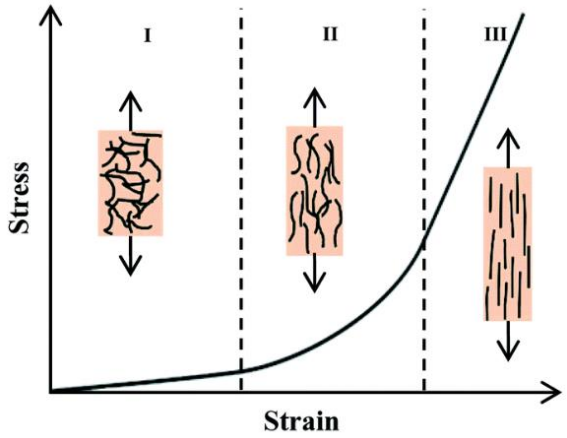

Fig. 3 | Stress-strain curve of skin. In phase I, fillers are anisotropically oriented and skin behaves as low modulus material. In phase 2, as the applied tensile load increases, the fillers start to align in the tensile load direction, and material's resistance to the deformation increases. In phase 3, with even more tensile load, skin behaves as linear elastic material.

II. Prior Arts

Mechano-Acoustic Sensing

The human body has a multitude of biological systems that perform voluntary and nonvoluntary dynamic motions of the organs. These motions generate both mechanical and acoustic or mechanoacoustic (MA) signals that attenuate at the skin-air interface[2–6] in wide range of magnitudes and frequency. They include nonvoluntary periodic subtle vibrations, such as cardiac activity (~10 Hz), respiration (~0.1 Hz), and strong irregular incidental activities, such as vocal fold vibrations (~100 Hz), gait and locomotion (~1 Hz), and body orientation (~0 Hz). This rich set of mechanoacoustic signals addresses many critical physiological information that are useful for diagnosis and rehabilitation.

However, many of the current monitoring systems impose spatial constraints on the monitoring event, resulting only non-continuous, episodical measurements[7]. For example, Polysomnography (PSG) and current vital signs monitor require table-top stationary electronic boxes that power the sensor directly from the wall-outlet and wires that channel the signal from the body to the box. Digital stethoscopes and inertial measurement units (IMU) are the sensors that specifically measure the MA signals but only capable of collecting a subset of these signals[7–10]. However the stethoscope is only capable of measuring signals in mid to high frequency band (20 to 1900 Hz)[7] and episodically. IMU is effective mainly to low frequency MA signals (0 – 100 Hz) owing to its loose coupling to the body[10,11]. Even with the confined bandwidth of their measuring capacity, these sensors can capture signatures of cardiac mechanics such as seismocardiograms or ballistocardiograms[12–15], respiratory rate and sounds[16–22], sounds of swallowing[23–26], vocals[27,28], changes in body position and motion[29–31] and others[32]. Therefore, they are clinically accepted and currently used in practice, particularly when implemented in devices that monitor multiple physiological signals[2,4,33].

Some of their applications are in monitoring the daily activity level and measuring athletic performance. However, the rigid, and planar form factors of these devices favor chest and wrist as their mounting location, thus require their forms to be straps, patches, or bands[27,34–38]. Other mounting location may be able to accommodate the devices' form factor but by sacrificing the comfort and reliable coupling to the body. For instance, IMUs adhere to the skin using wax and capture a few physiological information including movement and respiration for tracking sleep patterns[37]. Small microphone straps to the neck and captures speech and throat sounds for detecting swallowing events and different respiration characteristics[39]. With these coupling mechanisms, it is not feasible to have them on our body continuously for long period without causing skin irritation and discomfort and inducing poor signal quality.

Soft, lightweight skin-compatible mechanics can complement the limitations that the current technology has, and continuously monitor a full spectrum of MA signals without a large mechanical load on the skin. The device with such mechanics also has ability to measure the MA signals with high fidelity on most part of the body that provides the signal of interest.

With the recent advances in the soft electronics[2,40–44], we made a mechanoacoustic sensor that is skin compliant, lightweight and utilizing accelerometers that has high sampling rate and high resolution. The sensor utilizes elastomeric membrane functioning as the encapsulation, mounting interface and supporting structure for the functional components, including accelerometer, Bluetooth chip and wireless charging sub-system. A network of flexible circuit with serpentine shaped conductive traces maximizes the accelerometer's sensitivity to MA signals by mechanically separating it from other supporting components[2]. Combining these features, we have clinical-grade sensor that measures MA signal with high fidelity across wide range of frequencies, from 0 Hz body orientation to 1600 Hz audible signals without introducing any foreign objects or ambient noise inside of the packaging and the electronics.

This mechanoacoustic sensor uses the suprasternal notch (SN) as the mounting location. Taking advantage of this unique anatomical mounting location that offers a rich set of MA signal, having a single sensor mounted on a single location, we can simultaneously obtain the key parameters for many critical biological signals, including but not limited to respiratory, circulatory, digestive systems and ambulatory events. We validated the sensor data and its accuracy by comparing them to the data from clinically accepted conventional sensors, such as electrocardiogram, nasal cannula pressure transducer, chest band strain gauge and others. We also demonstrate its application in sleep study and many of unconventional studies that does not have a well-established gold-standard measurement, such as tracking COVID-19 disease progression, swallow, and speech therapy. Even further, by utilizing multiple accelerometers, we make the sensor that can reliably separate the motion artifacts and isolate the relatively subtle physiological information.

2. Mechanical Design of Flexible Wireless Electronics

The materials from this chapter is from: 'Lee, K., Ni, X., Lee, J.Y. *et al.* Mechano-acoustic sensing of physiological processes and body motions via a soft wireless device placed at the suprasternal notch. *Nat Biomed Eng* **4,** 148–158 [2020], [Nature Research]'

I. Mechanics of skin-device interface

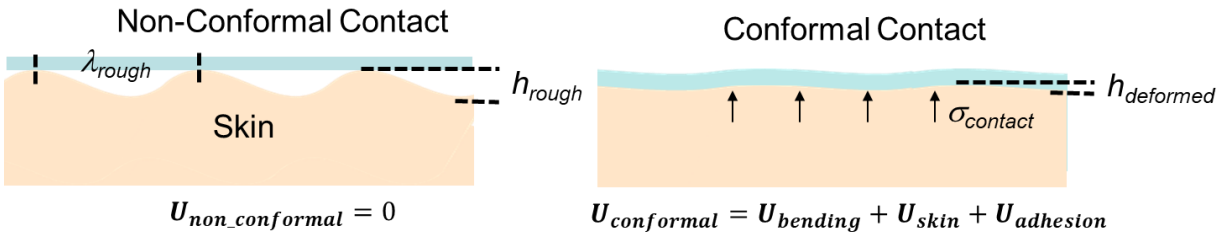

Fig. 4 | Theoretical model of the curved skin. The model assumes that the skin surface has periodic curvature with λ_{rough} as the wavelength and h_{rough} as the amplitude. When the skin makes conformal contact with a thin membrane, the interface does work on the skin and the membrane to match their interfacing topology, in addition to the energy require for the adhesion. As result, the conformal contact of the membrane puts contact stress on the skin and deform the surface geometry of the skin.

With the sensor that matches the skin's mechanical properties and has a small and thin form factor, we can minimize its mechanical load on the skin and enhance its wearability.

If the skin surface has periodic curvature with λ_{rough} as the wavelength and h_{rough} as the amplitude, when the sensor makes conformal contact with the skin, the contacting interface puts energy to bend the sensor and skin, in addition to the energy required for the sensor to adhere to the skin. As a result, the conformal contact changes the characteristics of the curvature, including $h_{deformed}$.

We express the $h_{deformed}$ at the equilibrium state of the conformal contact energy, $U_{conformal}$, as [4546]:

$$h_{deformed} = \frac{E_{skin} h_{rough}}{\frac{16\pi^3 E I_{device}}{\lambda_{rough}^3} + E_{skin}} \quad (1)$$

By substituting this expression to the analytical equation that relates normal stress on the top surface of the skin to the topology of the skin surface[47]:

$$\sigma_z = \frac{\pi E_{skin}(h_{rough} - h_{deformed})}{2\lambda_{rough}} \cos\left(\frac{2\pi x}{\lambda_{rough}}\right) \quad (2)$$

we obtain the following analytical expression describing the contact stress on the skin[46]:

$$\sigma_{contact} = \frac{8\pi^4 E_{skin} h_{rough}}{16\pi^3 \lambda_{rough} + \frac{E_{skin}\lambda_{rough}^4}{EI_{device}}} \cos\left(\frac{2\pi x}{\lambda_{rough}}\right) \quad (3)$$

It is important to highlight the contact stress's proportional relationship with the bending stiffness of the device.

II. Engineering mechanics of the device.

The thin, soft form factors of the systems introduced here allow skin-interfaced measurements of biosignals continuously and wirelessly at nearly any location across the body, including sensitive regions such as the SN. High data fidelity and comfortable, non-irritating interfaces are key features. Figs. 5a and b outline the overall device layout, with images that demonstrate its ability to deform naturally with movements of the neck when mounted on the SN. The design incorporates deformable, non-coplanar serpentine interconnects, a strain isolation layer at the base, a soft encapsulation overlayer and a hollow air-pockfdsaet configuration. Together, these features provide low modulus, elastic mechanics despite the incorporation of conventional rigid electronic components and flexible printed circuit board technologies with layouts that are compatible with high volume manufacturing.

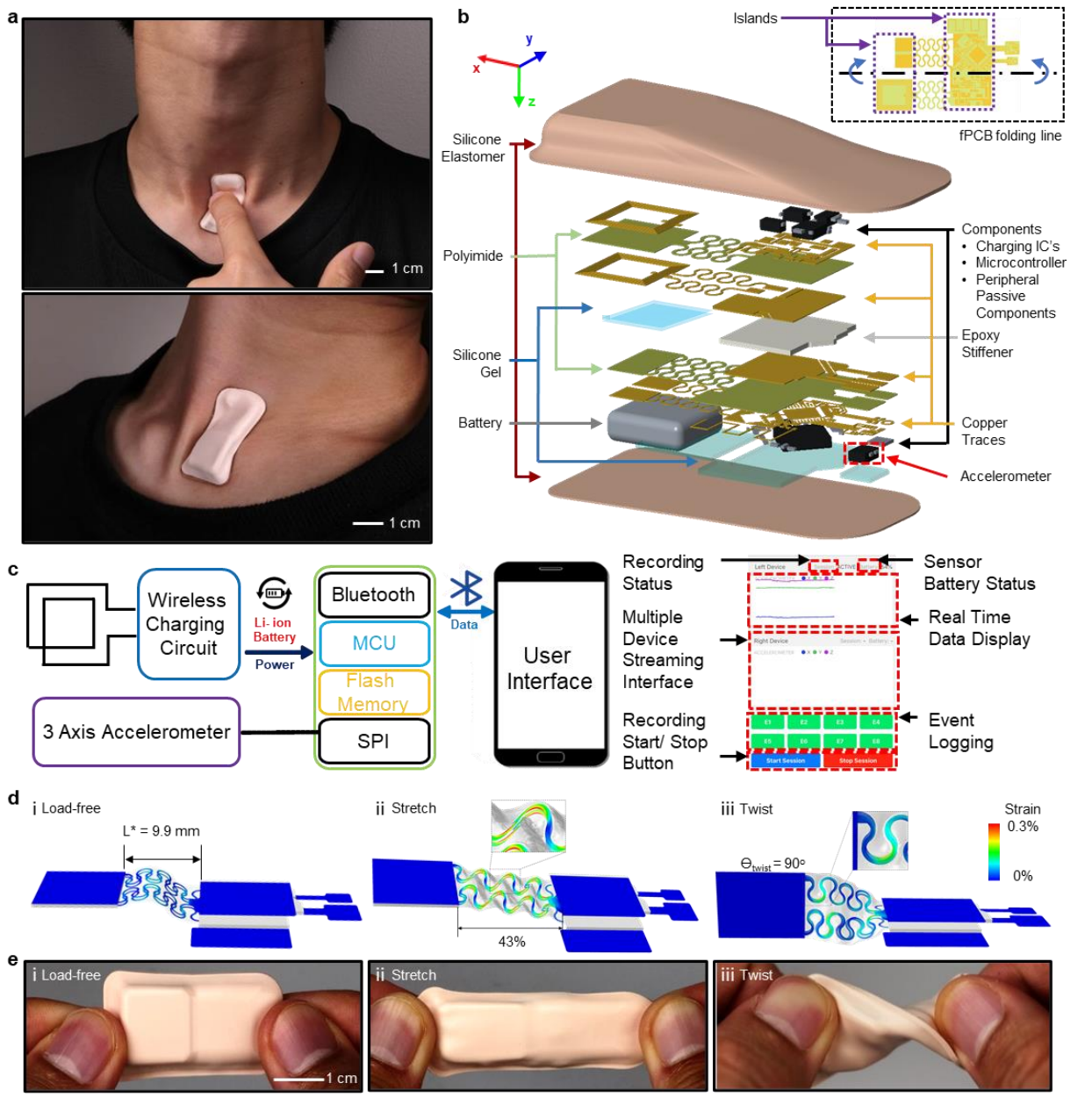

Fig. 5 | Images, schematic illustrations, functional flow charts and mechanical modeling results for a wireless, skin-interfaced mechano-acoustic (MA) measurement technology designed for mounting on the suprasternal notch (SN). **a**, Images that demonstrate soft device mechanics during movements of the neck while interfaced to the SN. **b**, Exploded schematic illustration of the active components, interconnect schemes and enclosure architectures. **c**, Block diagram of the system operation. **d**, Finite element modeling of the mechanics during uniaxial tensile and twisting deformations. **e**, Images of a device in undeformed (top), stretched (middle) and twisted (bottom) configurations.

Fig. 5b presents, more specifically, the overall structure of the system. The device consists of a flexible printed circuit board (fPCB) based on a 25 μm thick middle polyimide (PI) support

layer with patterned traces of 12 μm thick rolled, annealed copper (Cu) on the top and bottom surfaces (AP7164R, DuPont), each encapsulated with an insulating layer of PI (25 μm, FR1510, DuPont)[48]. The main electronic sub-systems include (1) a three-axis digital accelerometer (BMI160, Bosch) for measuring motions with a sampling frequency and resolution of 1600 Hz and 16 bits, respectively, a broad bandwidth response (0-1600 Hz) and a sufficient dynamic range (+/- 2 *g*) (*g* is the gravitational acceleration, 9.8 m/s^2), (2) a microcontroller (nRF52832, Nordic Semiconductor) for acquiring data from the accelerometer and communicating the results wirelessly via Bluetooth Low Energy (BLE) protocols and (3) a wireless inductive charging circuit to support a rechargeable 45 mAh lithium-polymer battery (Fig. 5c).

Because these sub-systems rely exclusively on rigid, planar off-the-shelf components, they must be carefully integrated in a manner that simultaneously offers soft, skin-compatible mechanics as well as effective mechanical coupling of the accelerometer to the body. The schemes used here exploit advanced versions of design concepts in stretchable electronics[44], adapted for use with the fPCB generally, and to its interconnects between the sub-systems specifically. As shown in Fig. 5b, serpentine-shaped interconnects mechanically and electrically join two rectangular regions of the fPCB (islands; 1 cm x 1 cm). One island supports the microcontroller and charging circuit. Here, the fPCB folds onto itself to minimize the area consumed by the rigid components (Fig. 5b). The other island includes the charging coil and connections to the battery. The coil includes two Cu traces (120 μm widths) in a rectangular spiral design (8 turns, 100 μm pitch) on both top and bottom sides of fPCB. This minimizes the overall size of the device while allowing larger electromagnetic flux to go through the coil as compared to a single layer coil with the same dimension. The top and bottom coils share the same polarity

and dimensions (9.55 mm by 10.7 mm). Electroplating (Contac S4) creates a conductive path across the two sides of fPCB through holes located at the ends of the coils.

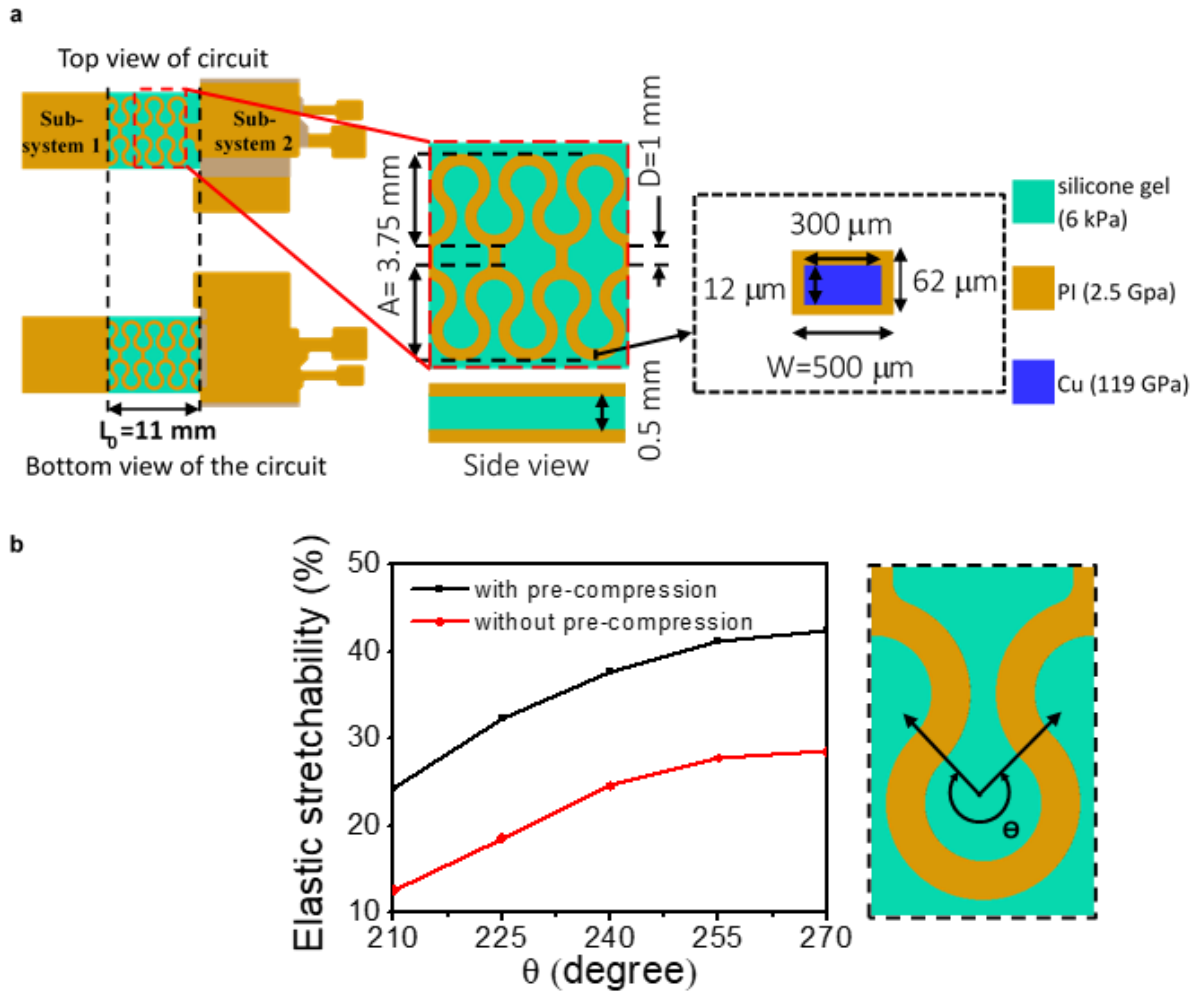

Fig. 6 | Optimized mechanical designs for the electrical interconnects. (a) Schematic illustration of a double layer serpentine interconnect with an arc angle of 270º **(b)** Relationship between the arc angle and the elastic stretchability of the interconnects with and without pre-compression.

Small pieces of rigid printed circuit board material (Garolite G-10/FR4; 381μm thick, 22 GPa modulus, McMaster Carr 1331T37) support each of the two main islands to increase their bending stiffness by three orders of magnitude (49 μm thick, 4.8 GPa modulus). This design effectively eliminates bending in these regions, thereby enhancing the robustness of the solder bonding joints between the components and the fPCB. These islands comprise 30% of the overall

area of the system, leaving ~70% for freely deformable regions including the serpentine-interconnect structures.

The accelerometer rests on a cantilever that extends from the component island by a thin, narrow region of the fPCB to allow effective coupling to the skin with minimal mechanical constraints from other parts of the system (dotted outline in Fig. 5b). To prevent entanglement, the interconnects consist of two layers of serpentine wires embedded in silicone gel (Silbione 4717 Gel A/B, Elkem, 0.4mm thick) with a low Young's modulus (6 kPa) to minimize constraints on deformation of the serpentine wires (Fig. 6a).

We used commercial software ABAQUS (ABAQUS Analysis User's Manual 2010, V6.10) to design the device and optimize its mechanical performance. The objectives are to ensure that (1) the Cu layer in the interconnects remains elastic, i.e., no plastic deformation, and (2) minimize the normal and shear stresses on the human skin to achieve a low somatosensory perception when the device undergoes different types of external loads (stretching, bending, and twisting).

The epoxy, silicone elastomer (Ecoflex), and silicone gel were modeled by hexahedron elements (C3D8R) while the thin Cu layer and PI films were modeled by composite shell elements (S4R). The number of elements in the model was ~2×10^7, and the minimal element size was 1/8 of the width of the narrowest interconnects (100 μm). The mesh convergence of the simulation was guaranteed for all cases. The elastic modulus (E) and Poisson's ratio (v) are E_{Cu}=119 GPa, v_{Cu}=0.34, E_{PI}=2.5 GPa, v_{PI}=0.34, E_{Gel}=5 kPa, v_{Gel}=0.49, E_{Ecoflex}=60 kPa, $v_{Ecoflex}$=0.49, E_{Epoxy}=22 GPa and v_{Epoxy}=0.32.

Finite element analysis (FEA) results highlight significant mechanical advantages of these non-coplanar interconnects compared to conventional planar serpentine layouts (Fig. 6). At the optimized arc angle $\theta = 270^{o}$ and with pre-buckling, the elastic stretchability, $\varepsilon = (L_y\text{-}L^*)/L^*$, where

L* is initial length (Fig. 5di) and L_y is the length where the Cu layer reaches the limit of plastic yielding, improves to 43% from 14% stretchability with arc angle $\theta = 210^o$ and without pre-buckling (Figs. 5dii and 6b).

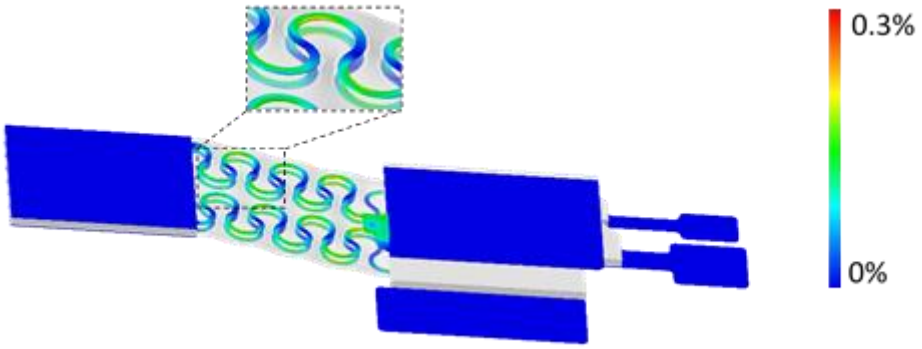

Fig. 7 | The strain distribution in the Cu layer of the interconnect after stretching to 11 mm. The interconnects straighten back to their nominal (non-buckled) length from the pre-buckled state at 11% strain of the overall device

A pre-buckled, out-of-plane, arc-shaped geometry allows the serpentine interconnects to assume traction-free architectures that absorb tensile deformations in two distinct modes (Figs. 7 and 5dii) in a manner largely decoupled from the device's bottom substrate.

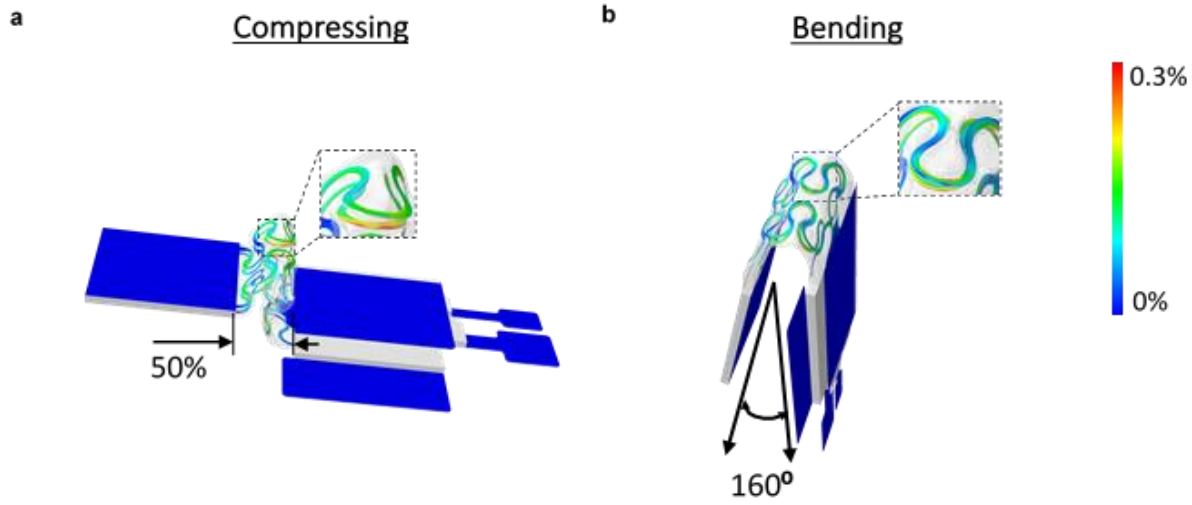

Fig. 8 | The strain distribution in the Cu layer for the device after deformations. (a) 50% compression and **(b)** 160° bending angle. For both loading cases, the computed strain in the Cu layer of interconnects is lower than the 0.3% yielding strain

Additional FEA results indicate that the maximum effective strain in the Cu layer is significantly less than the yield strain (0.3%) under various mechanical loads (Figs. 5diii and 8).

III. Design of the Encapsulating Enclosure.

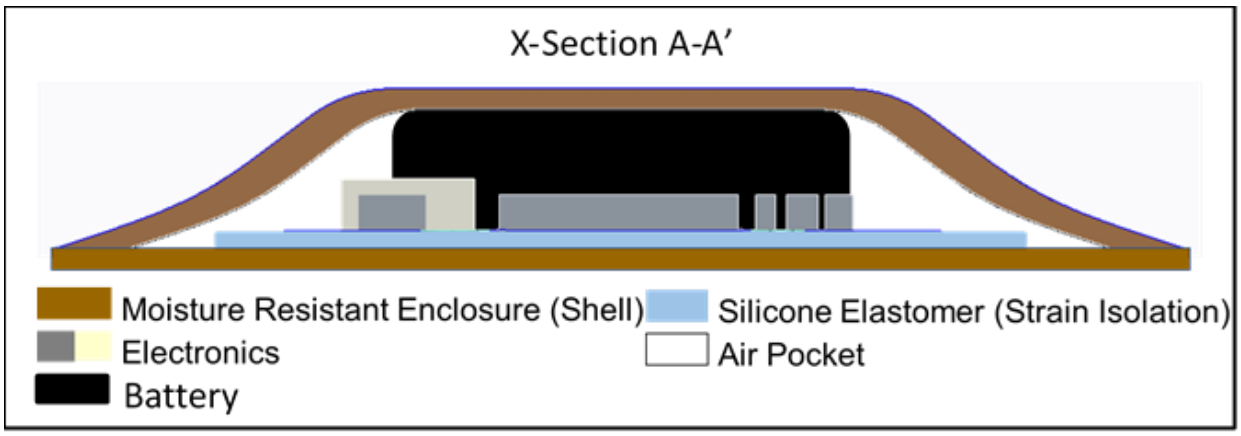

Fig. 9 | Cross-sectional schematic illustration of the architecture of the system. A thin membrane (300 μm) of a low modulus formulation of silicone (Ecoflex) forms an air pocket, or hollow enclosure. The hollow enclosure construction minimizes mechanical constraints of the serpentine interconnects during the device deformations

A thin (~0.3 mm) elastomeric membrane of silicone (modulus, 60 kPa; toughness, 500 MPa) forms a hollow enclosure that protects the system from the environment. This design provides a waterproof encapsulation structure that also allows free movement of the buckled serpentine interconnects (Fig. 9). The device shows no degradation in performance after complete immersion in phosphate buffered saline solution at 70°C for ten days.

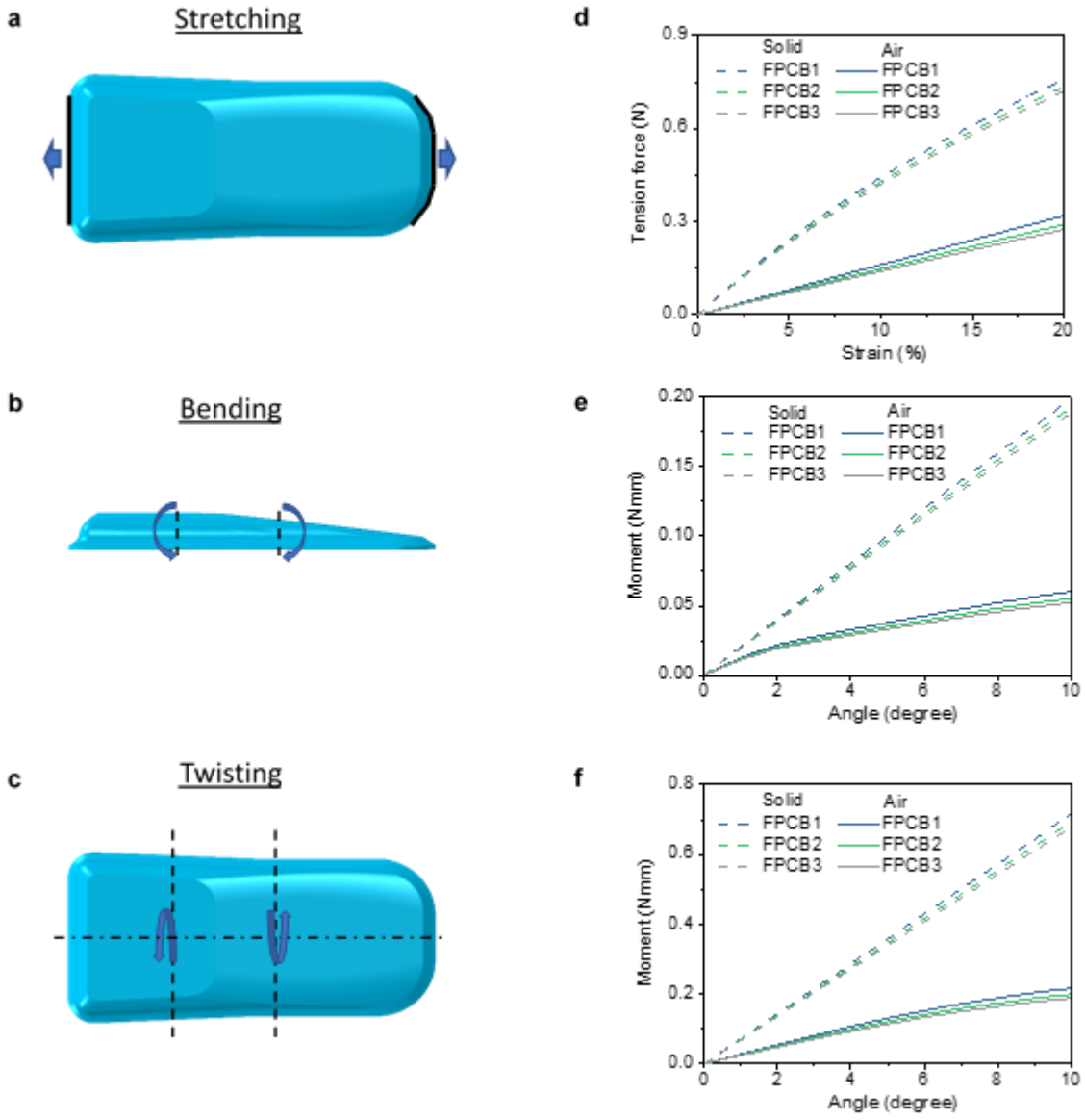

Fig. 10 | FEA results of the devices with different FPCBs thicknesses under different modes of mechanical loading. Illustration of device under different modes of load: **(a)** stretching, **(b)** bending, and **(c)** twisting on the devices with different FPCBs thicknesses (FPCB1: 12 μm PI/ 25 μm Cu/ 12 μm PI; FPCB2: 8.69 μm PI/ 20 μm Cu/ 8.69 μm PI; FPCB2: 5.79 μm PI/ 12.5 μm Cu/ 5.79 μm PI). **(d)** Tensile force as a function of the applied strain for the solid and hollow package with a 61 kPa and 18 kPa equivalent tensile modulus for the devices with FPCB1 respectively. **(e)** Moment as a function of the bending angle for the solid and hollow package configurations with a 11 Nmm^2 and 6.8 Nmm^2 equivalent bending stiffness for the devices with FPCB1 respectively. **(f)** Moment as a function of the twisting angle for the solid and hollow package configurations with a 38 Nmm^2 and 15 Nmm^2 equivalent twisting stiffness for the devices with FPCB1 respectively. The results for stretching, bending, and twisting deformation show that the thickness of the layers has a small influence (less than 10% difference) in the equivalent tensile modulus, bending, and twisting stiffness for these three FPCBs.

By comparison to a conventional, solid core encapsulation strategy, the hollow air-pocket layout reduces the equivalent tensile modulus and bending/twisting stiffnesses by ~ 3.4, ~ 1.6, and ~ 2.5 times, respectively (Figs. 10d, e and f). In fact, the equivalent tensile modulus is only ~18 kPa, nearly seven times lower than that of human skin (120 kPa) [49]. The bending and twisting stiffnesses (~17.2 Nmm^2 and ~59.4 Nmm^2, respectively) are ~2.5 and ~3.9 times lower than those of the skin with comparable thickness.

These results highlight the range of robust, low- modulus, elastic responses (Fig. 10) necessary to accommodate realistic physiological motions with little constraint on the underlying skin (Fig. 5e). Fig. 10 also shows that the fPCB thickness has little effect on the overall device modulus and stiffness.

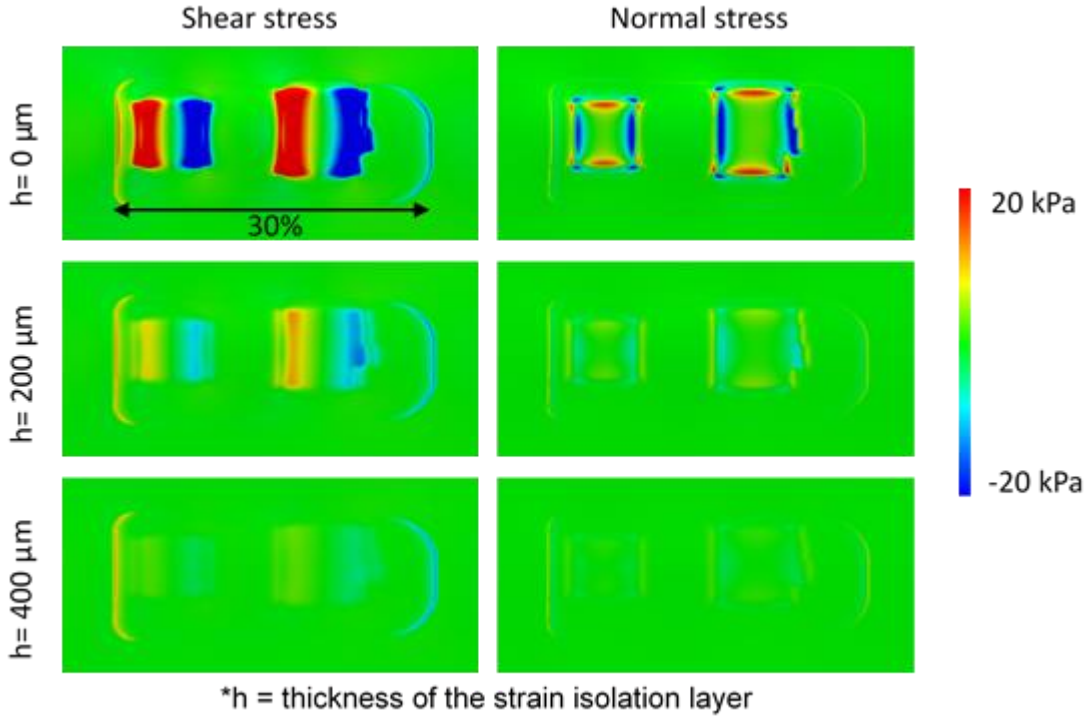

Fig. 11 | The stress distributions on the skin with a strain isolation layer. The color indicates stress on the skin induced by stretching the device by 30% when different strain isolation layer thicknesses (h = 0, 200, and 400 µm) are used.

A layer of a soft silicone gel (Silbione 4717 Gel A/B, Elkem) at the base of the system, but within the encapsulating structure, provides a degree of mechanical isolation from the underlying skin, where stresses would otherwise accumulate at the locations of the islands during motions and/or deformations of the body and skin. Simulations indicate that the shear and normal interfacial stresses remain below the threshold for sensation (~20 kPa) for deformations of the skin to tensile strains of up to 30% when the thickness of the gel is 400 μm (Fig. 11).

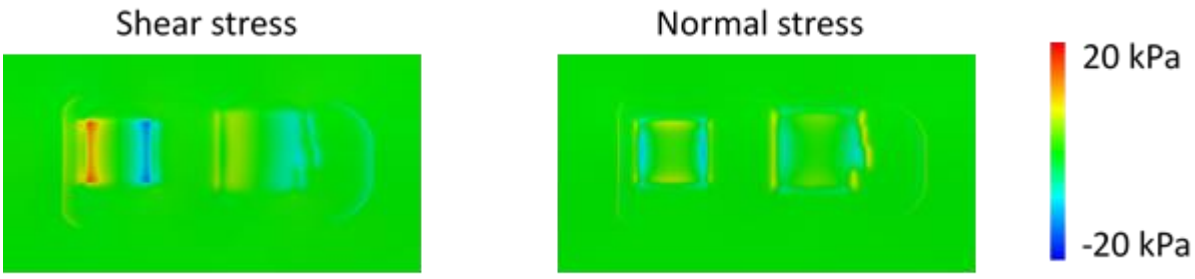

Fig. 12 | The stresses on the skin from the 10% stretched device without a strain isolation layer. The device without the strain isolation layer induces stress on the skin even at low tensile strain.

Without the strain isolation layer, the stresses reach 20 kPa at strains of only 10% (Fig. 12). The strain isolation layer does not, however, extend to the region of the device that supports the accelerometer, thereby ensuring its intimate mechanical coupling to the skin.

IV. Effect of design in signal fidelity.

In addition to the mechanical characterization of the complete device, the effect of the packaging material and device structure on the signal fidelity is as important aspect for design to consider. In fact, many of the design consideration and the device architectures also provides benefit to the signal quality. For instance, the strain isolation layer reduces the effective stiffness of the device at the skin interface, allowing the sensor to have a conformal contact with the skin. The conformal contact reduces the air-gap and delamination points in the interface and enhance the signal transmission (Appendix 1).

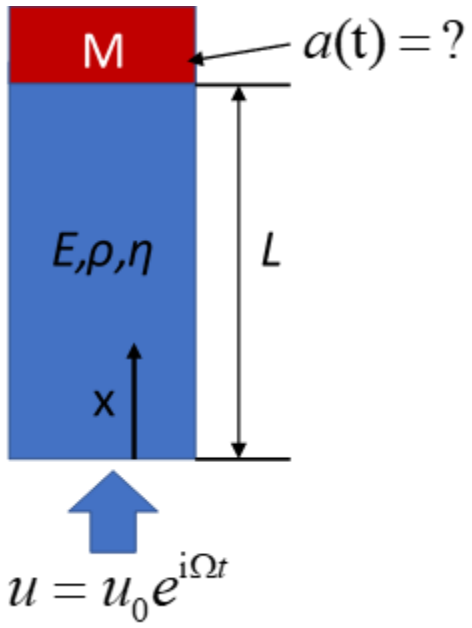

Fig. 13 | Schematic illustration of the vibration model of a one-dimensional rod with damping. The parameters of the model are described next. E, ρ and η are the Young's modulus, mass density and damping coefficient, respectively. L and M are the length of the substrate and mass of the device per unit area. The amplitude and angular frequency of the applied excitation is given by u_0 and Ω respectively. x and t are the spatial coordinates and time

Fig. 13 summarizes an analytic model for the device on the skin. For one-dimensional vibration of a viscoelastic rod, the displacement takes the form $u=f(x)e^{i\omega t}$, where t is time, ω is the angular frequency, and $f(x)$ depends on the x coordinate. The relation between strain ε and displacement u, constitutive model (Kelvin-Voigt model), and dynamic equation of motion are:

$$\varepsilon = \frac{\partial u}{\partial x} \tag{4}$$

$$\sigma = E\varepsilon + \eta \frac{\partial \varepsilon}{\partial t} \tag{5}$$

$$= (E + i\omega\eta)\frac{\partial u}{\partial x}$$

$$\frac{\partial \sigma}{\partial x} = \rho\frac{\partial^2 u}{\partial t^2} \tag{6}$$

respectively, where σ is the stress, and E, ρ and η are the Young's modulus, mass density, and viscoelastic damping coefficient, respectively.

Substitution of Eq. (5) into Eq. (6) gives:

$$\frac{\partial^2 u}{\partial x^2} = \frac{1}{c^2}\frac{\partial^2 u}{\partial t^2} \tag{7}$$

where:

$$c = \sqrt{\frac{E + i\omega\eta}{\rho}} \tag{8}$$

For the problem shown in Fig. 13, the displacement and stress boundary conditions at $x = 0$ and $x = L$ are given by:

$$\begin{cases} u(0,t) = u_0 e^{i\Omega t} \\ \sigma(L,t) = -M\dfrac{\partial^2 u(x,t)}{\partial t^2}\Big|_{x=L} \end{cases} \tag{9}$$

where u_0 and Ω are the magnitude and the angular frequency of the excitation load (from the vibration platform) applied to the rod at $x = 0$. M is the mass per unit area, which represents the mass of the device over the area of its bottom layer.

The Fourier transform:

$$\begin{aligned} \hat{u}(x,\omega) &= \int_{-\infty}^{+\infty} u(x,t)e^{-i\omega t}dt \\ u(x,t) &= \frac{1}{2\pi}\int_{-\infty}^{+\infty} \hat{u}(x,\omega)e^{i\omega t}d\omega \end{aligned} \tag{10}$$

applied to Eq. (7) gives

$$\frac{d^2\hat{u}}{dx^2} + k^2\hat{u} = 0 \tag{11}$$

where $k = \frac{\omega}{c}$. The boundary conditions in Eq. (9) become

$$\begin{cases} \hat{u}(0,\omega) = 2\pi u_0 \delta(\omega - \Omega) \\ \hat{\sigma}(L,\omega) = -M(-i\omega)^2\hat{u}(L,\omega) = M\omega^2\hat{u}(L,\omega) \end{cases} \tag{12}$$

where $\delta(x)$ is the Dirac Delta function.

The solution of Eq. (11) is

$$\begin{aligned} \hat{u}(x,\omega) &= C_1 e^{ikx} + C_2 e^{-ikx} \\ \hat{\sigma}(x,\omega) &= ik(E + i\omega\eta)(C_1 e^{ikx} - C_2 e^{-ikx}) \end{aligned} \tag{13}$$

where the coefficients C_1 and C_2 are determined by the boundary conditions (12) to (13) as

$$\begin{cases} C_1 = \dfrac{[ik(E + i\omega\eta) + M\omega^2]e^{-ikL}\pi u_0 \delta(\omega - \Omega)}{ik(E + i\omega\eta)\cos(Lk) - iM\omega^2 \sin(Lk)} \\ C_2 = \dfrac{[ik(E + i\omega\eta) - M\omega^2]e^{ikL}\pi u_0 \delta(\omega - \Omega)}{ik(E + i\omega\eta)\cos(Lk) - iM\omega^2 \sin(Lk)} \end{cases} \tag{14}$$

Substituting Eq. (14) into Eq. (13) yields

$$\hat{u}(x,\omega) = \left\{ \begin{aligned} &\frac{[ik(E + i\omega\eta) + M\omega^2]e^{-ikL}e^{ikx}}{ik(E + i\omega\eta)\cos(Lk) - iM\omega^2 \sin(Lk)} \\ &+ \frac{[ik(E + i\omega\eta) - M\omega^2]e^{ikL}e^{-ikx}}{ik(E + i\omega\eta)\cos(Lk) - iM\omega^2 \sin(Lk)} \end{aligned} \right\} \pi u_0 \delta(\omega - \Omega) \tag{15}$$

The Fourier Transform of the acceleration $a(x,t) = \partial^2 u(x,t)/\partial t^2$ is

$$\hat{a}(x,\omega) = (-i\omega)^2\hat{u}(x,\omega) \tag{16}$$

Its inverse transform gives the acceleration

$$a(x,t)=\frac{1}{2\pi}\int_{-\infty}^{+\infty}\left\{-\pi u_0\omega^2\delta(\omega-\Omega)\left[\begin{matrix}\dfrac{[ik(E+i\omega\eta)+M\omega^2]e^{-ikL}e^{ikx}}{ik(E+i\omega\eta)\,cos(Lk)-iM\omega^2\,sin(Lk)}\\ +\dfrac{[ik(E+i\omega\eta)+M\omega^2]e^{ikL}e^{-ikx}}{ik(E+i\omega\eta)\,cos(Lk)-iM\omega^2\,sin(Lk)}\end{matrix}\right]\right\}e^{i\omega t}d\omega \tag{17}$$

which can be further expressed as

$$a(x,t)=-u_0\Omega^2e^{i\Omega t}\left\{\frac{\sqrt{(E+i\omega\eta)\rho}\,cos\left[\frac{(x-L)}{c}\Omega\right]+M\Omega\,sin\left[\frac{(x-L)}{c}\Omega\right]}{\sqrt{(E+i\omega\eta)\rho}\,cos\left(\frac{L}{c}\Omega\right)-M\Omega\,sin\left(\frac{L}{c}\Omega\right)}\right\} \tag{18}$$

The acceleration at the x=L is

$$a(L,t)=\frac{-u_0\Omega^2e^{i\Omega t}\left(\frac{L}{c}\Omega\right)}{\left(\frac{L}{c}\Omega\right)cos\left(\frac{L}{c}\Omega\right)-\left(\frac{LM\Omega^2}{E+i\omega\eta}\right)sin\left(\frac{L}{c}\Omega\right)} \tag{19}$$

For the displacement at the other end $x=0$ to take the form $u(0,t)=\mathrm{Re}\left\{u_0e^{i\Omega t}\right\}=u_0\cos(\Omega t)$, the above acceleration at the end x=L is simplified to

$$a(L,t)=Re\left\{\frac{-u_0\Omega^2e^{i\Omega t}\left(\frac{L}{c}\Omega\right)}{\left(\frac{L}{c}\Omega\right)cos\left(\frac{L}{c}\Omega\right)-\left(\frac{LM\Omega^2}{E+i\omega\eta}\right)sin\left(\frac{L}{c}\Omega\right)}\right\} \tag{20}$$

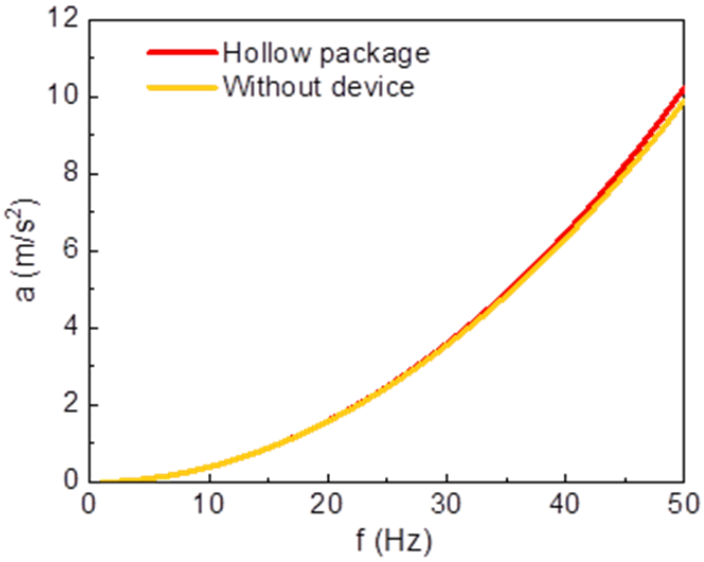

Fig. 14 | The acceleration of the elastomer as a function of the applied frequency for the hollow package and without a device. The parameters used in the simulation are E = 60 kPa, ρ = 1070 kg/m^3, L = 2 mm, M_{hollow}=0.01 g/mm^2 which represents the weight of the device over the area of its bottom layer, u_0 = 0.1 mm, and the damping ratio (ξ= ηω) was 0.03.

For frequencies between 1 and 50 Hz (Fig. 14), the difference in the acceleration of skin with and without the device is less than 3%, due to the small mass (4.56 g) of the device.

Figs. 13-15 illustrates the effect of the packaging materials and device structure on the signal fidelity.

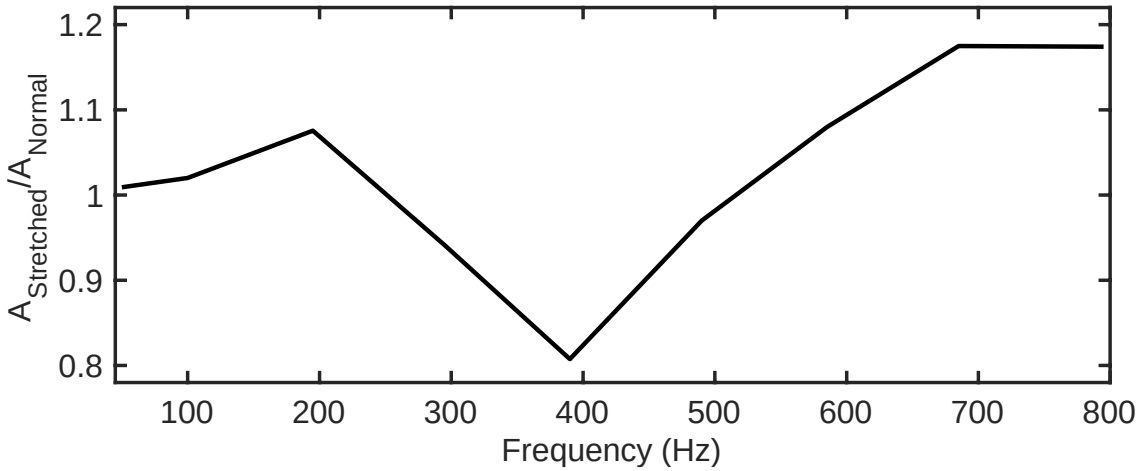

Fig. 15 | Experimental comparison between the frequency responses of a normal device and a 12% stretched device. The ratio between the frequency response of a 12% stretched device $A_{Stretched}$ and that of a normal device A_{Normal} stays close to 1 across the frequency range (0-800 Hz) except for a maximum of ~20% drop around 400 Hz. The stretched device becomes more sensitive at high frequencies (>500 Hz). The stretched device also delaminates at a higher frequency (>295 Hz) and causes transient instability.

Fig. 15 compares z-axis acceleration recordings across a frequency range of 0 to 800 Hz, measured by a complete wireless system and by a wired, isolated accelerometer. The ratio between the two measurements is close to unity across the measurement range, demonstrating

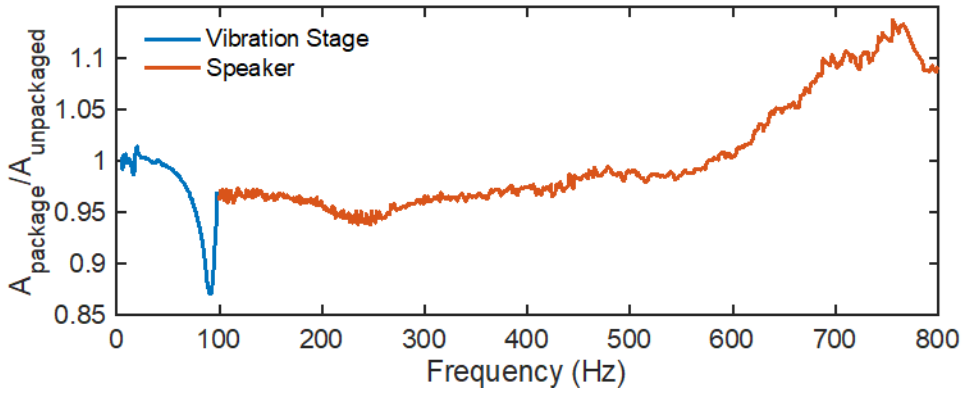

Fig. 16 | Experimental comparison between the frequency responses of a hollow packaged device and a mechanically independent accelerometer. The ratio between the frequency response of a hollow packaged device $A_{packaged}$ and that of an unpackaged accelerometer $A_{unpackaged}$ stays close to 1 in the frequency range of interest (0-800 Hz), except for a maximum of ~13% drop in the relative response around 91 Hz due likely to a resonance; the encapsulated device is more sensitive than the unpackaged one at high frequencies (>600 Hz). The driving sources for the frequency sweep tests are a vibration stage (3B, Scientific) (1-100 Hz) and a speaker (100-800 Hz).

that the effects of the packaging materials are negligible. As shown in Figs. 13-14, results from a simple simulation model confirms these findings.

Similar measurements show that the responses of the device are not significantly affected by stretching to tensile strains of 12% (Fig. 16).

V. Assembly of the Devices.

A 3-axis milling machine (Roland MDX 540) created aluminum molds in geometries defined by three-dimensional computer-aided design (CAD) drawings created using ProE Creo 3.0. Casting a silicone thermoset polymer into the gap formed by matching pairs of molds defined the capping membrane (Ecoflex, 00-30, Smooth-on) with well controlled thickness (300 μm). Curing occurred in an oven at 70 º C for 15 minutes. Bonding this membrane to a planar silicone substrate film around the perimeter defined an air cavity that enclosed the electronics.

Silicone gel (Silbione RT Gel 4717 A/B, Bluestar Silicone, E = 5 kPa) served as a strain isolation layer at the base of the device. A manual screen-printing process delivered this material onto the substrate film in a pattern to match geometries of the islands. Heating on a hot plate at 100 º C for 5 minutes cured the gel. Delivering the electronics in aligned fashion onto this gel, capping the entire structure with the membrane that is molded into a preformed shape and bonding the preformed membrane on top of the planar silicone substrate around its perimeter completed the fabrication.

VI. Data and analysis approaches for measurements from the suprasternal notch.

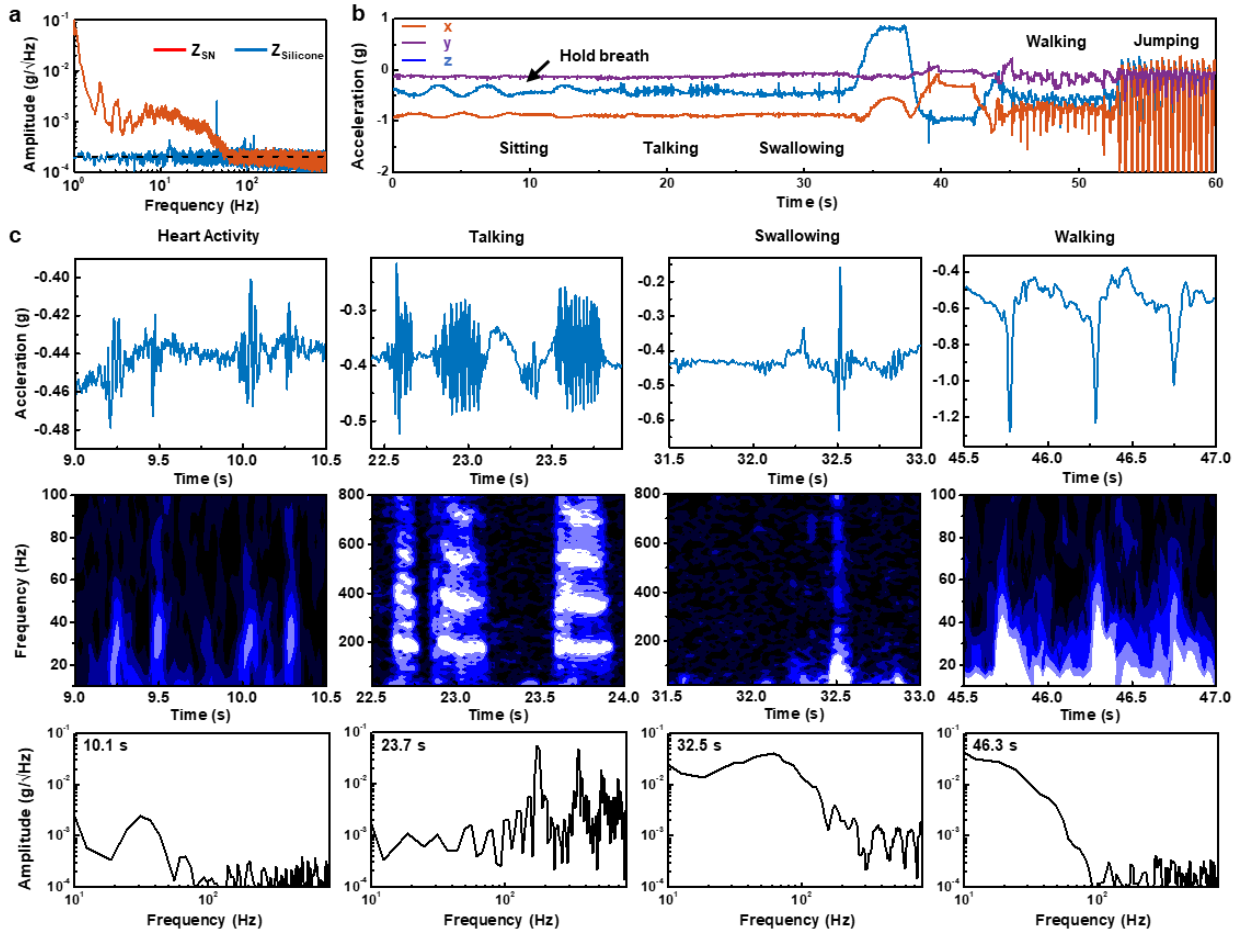

Fig. 17 | Representative mechano-acoustic (MA) data in the form of accelerations measured along three orthogonal axes from a device mounted on the suprasternal notch (SN) of a healthy normal subject. a, Power spectral analysis of data (z-axis acceleration) collected from a device vertically resting on an elastomer and interfaced to the SN of a subject sitting quietly. The power spectrum of the measurement from the SN shows high power below 100 Hz associated with various involuntary physiological events. **b**, 3-axes time series data simultaneously recorded over a 60 second interval as a subject engages in various activities that include sitting at rest, talking, drinking water, changing body orientation, walking and jumping. **c**, Sample time series data, spectrograms, and spectral information corresponding to cardiac activity, talking, swallowing, and walking. The frequency analysis uses a Hanning window with a width of 0.1 s moving in time steps of 0.02 s.

Natural physiological processes generate diverse MA signals at the surface of the skin, from subtle vibrations on the order of $\sim 1 \times 10^{-4}\ g/\sqrt{\mathrm{Hz}}$ (Fig. 17a) to large-scale motions with amplitudes of $\sim 2\ g$, across a band of frequencies (0 to 800 Hz) that can be captured with the accelerometers used here. The SN represents a unique anatomical location for recording such

signals, as a direct soft tissue MA interface to vital organs related to cardiovascular, respiratory, and digestive systems and their interconnections between the head and torso. Fig. 17a shows the typical sensitivity of the device (z-axis, axes defined in Fig. 5b) characterized when placed on a vertical slab of elastomer (4 mm thick, 60 kPa) and when interfaced to the SN (Fig. 5a) of a subject while sitting quietly. The sensor on the slab shows nearly uniform noise power density across the entire frequency range.

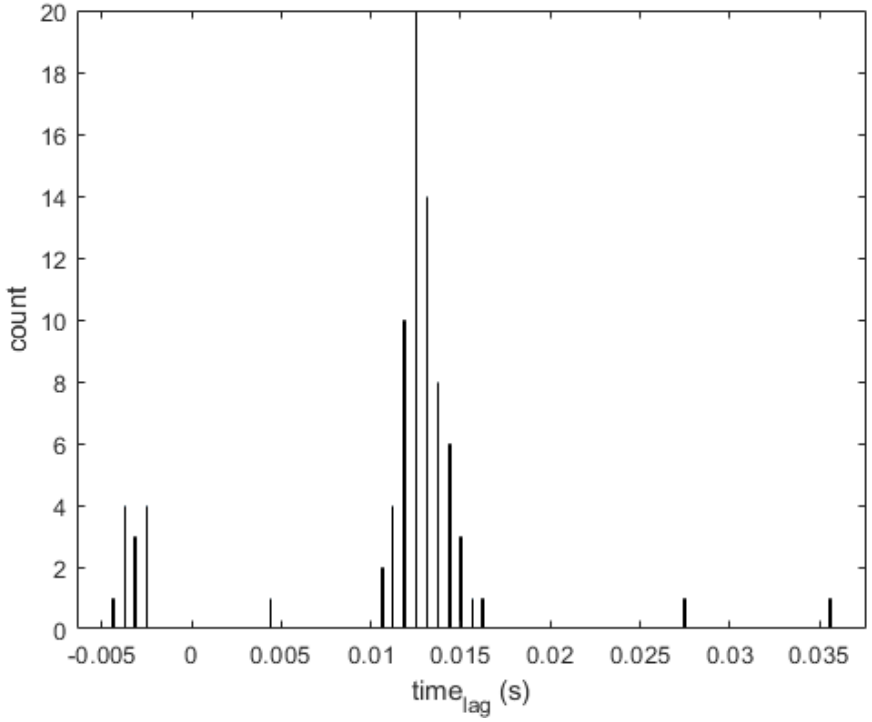

Fig. 18 | Histogram of the time lag results from cross correlations between the pulses from the suprasternal notch (SN) and from the chest. The SN has the time lag of ~13 ms. This indicates that the vibratory signatures related to the pulsatile flow of blood are from the carotid artery as opposed to chest/body vibrations due directly to the heartbeat.

At the SN, proximity to the carotid artery results in vibratory signatures related to the pulsatile flow of blood. The periodic nature of these signals allows determination of heart rate and variability. The cross-correlation of pulses measured from the chest near the pulmonic area and the SN defines a time lag between these two signals (Fig. 18). The lag of ~13 ms is consistent

with recordings of vibratory signatures from the carotid artery itself, as opposed to chest/body vibrations. The amplitudes yield information on the intensity of cardiac activity and, indirectly, stroke volume. Passage of air through the trachea and movements of the chest wall produce MA data related to swallowing, talking, breathing, coughing, sighing, snoring and other responses. Furthermore, the device simultaneously responds to chest wall and full-body movements, including orientation referenced to the gravity vector.

All such signals rise well above the noise floor of the measurement system. To demonstrate the collective capabilities, Fig. 17b presents representative three-axis acceleration data recorded from the SN of a healthy normal subject engaged in a sequential series of activities. The signals associated with each of these and other activities exhibit distinct features in time and frequency, thereby conveying a rich set of information related to body processes. The following analysis focuses, for simplicity, on accelerations measured along the direction normal to the surface of the skin (z-axis).

The first 10 seconds of the data feature signals that arise from respiration. Here, expansion and contraction of the chest wall induce periodic rotations of the device around the y-axis at the neck, along with some translational motions. The main effect is to change the magnitude of the projection of gravity along the z- and x-axes. Mounted on the SN, the device includes grounded points (e.g. trachea) that do not move with the chest wall. Thus, the angular range of rotations (~1.3°) from respiration is larger than that associated with chest wall movement alone (~0.5°). As the subject begins to hold one's breath at the ~10 s mark, these periodic changes cease. Talking and swallowing generate high-frequency signals associated with acoustic vibrations and rapid motions, as shown in the data from 16-34 s. When the subject leans in different directions through the time period from 34-45 s, quasistatic 3-dimensional accelerations provide instantaneous

measurements relative to the gravity vector indicative of body orientation. Walking (45-53 s) and jumping (53-60 s) induce large amplitude accelerations with significant projections along all axes.

Fig. 17c shows quantitative details of the high-frequency features (>10 Hz) of individual physiological events. Cardiac activities – both systole and diastole[11]– give rise to paired pulses with peak amplitudes of ~0.05 *g*, and power concentrated in a frequency band of 20-50 Hz. The speech signals feature high-quality harmonic structures with fundamental frequencies in the range of 85 to 255 Hz for typical adults[50,51]. Swallow events initiate with slow motion (~0.1 s) of the vocal folds and with larynx mechanics during the pharyngeal phase and end with a high-frequency ring-down associated with flow of water or food during the esophageal stage[8]. Large impact forces that span a broad frequency ranges up to ~100 Hz characterize walking motions.

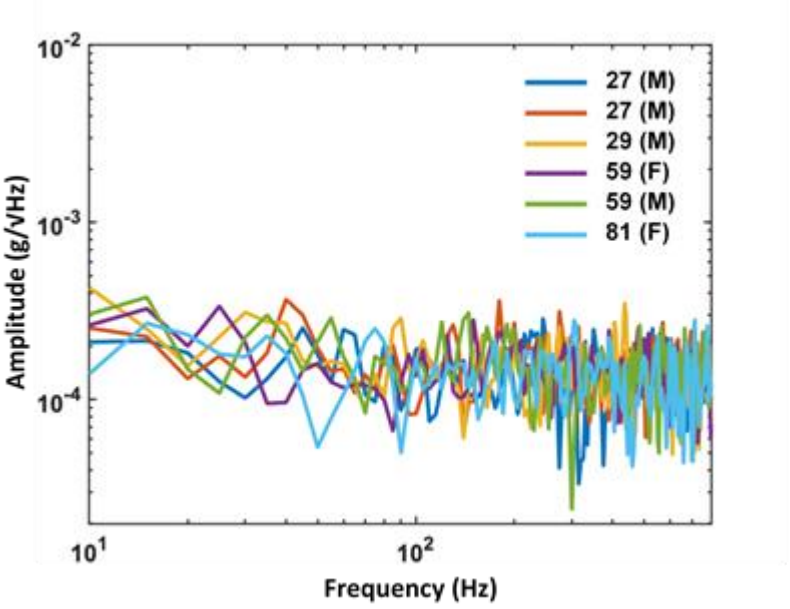

Fig. 19 | Short-time windowed (0.2 s) spectrum of z-axis acceleration measured from the SN of five subjects across different ages and genders. Data from male (M) and female (F) subjects from 27 to 81 years old, each while sitting quietly in a resting state. The analysis windows are manually chosen from time periods where no bio-signals are clearly present. The spectrums indicate a noise behavior of the device close to that on the Ecoflex (Fig. 17a), which exhibit no clear difference between different age groups.

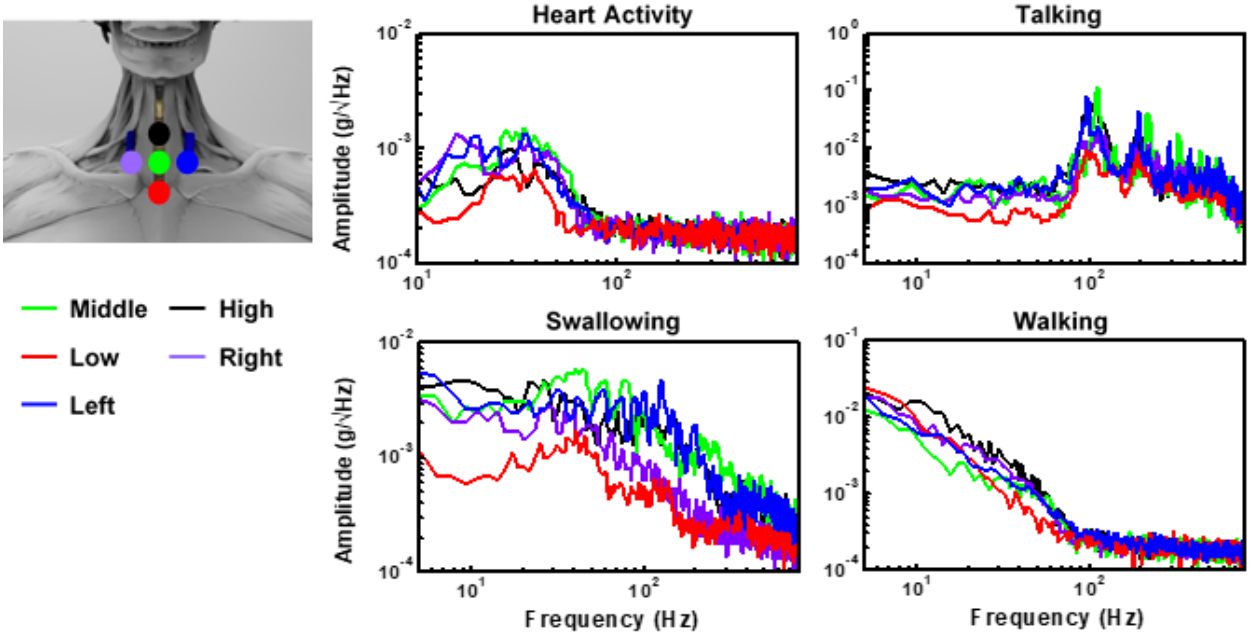

Fig. 20 | Demonstration of the effect of mounting location. The measurements are from five different locations (+/- 1 cm vertical and horizontal displacements from the center of the SN) of a male subject with lower body mass. The results indicate that the device is not sensitive to the mounting locations, especially for the prominent frequency range for each distinctive event. There are slight differences in the magnitude

of the signal relative to the position which agrees with the anatomical locations of the associated signal sources.

The characteristic frequencies and temporal structures of these features do not depend critically on the subject (gender, body type, ethnicity and age) (Fig. 19) or the mounting location in the vicinity of the SN (Fig. 20), although their relative amplitudes can vary slightly. For instance, the magnitudes of talking/swallowing signals increase as the mounting location approaches the larynx and upper esophageal sphincter. The magnitudes of walking signals are invariant with position as might be expected. Biological features across different subjects, including the fundamental frequencies of speech[52], the thickness of the skin, and other aspects lead to differences in the signal, in ways that are expected and do not affect approaches in signal analysis and interpretation.

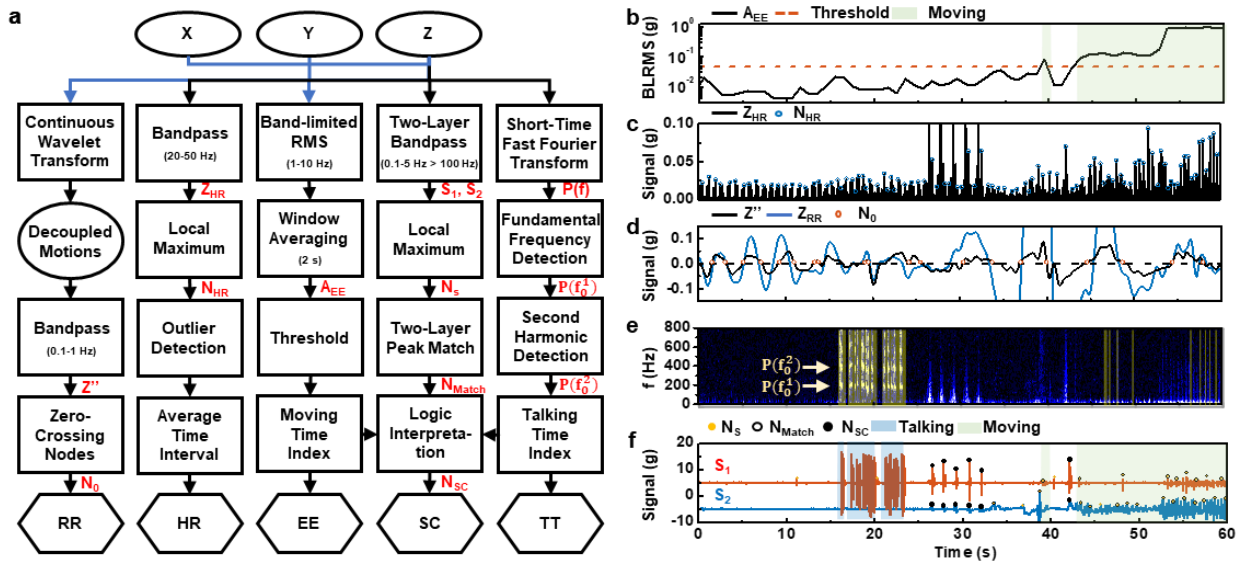

Fig. 21 | Flow diagram of signal processing and corresponding results from representative mechano-acoustic (MA) data acquired from healthy normal subjects. a, Block diagram of post-processing analytics for energy expenditure (EE), heart rate (HR), respiration rate (RR), swallow count (SC) and talking time (TT); blue arrow indicates a use of three-axis accelerometer data and black arrow feeds only z-axis data. EE: The window-averaged 1-10 Hz band-limited root-mean-square (BLRMS) sum of data from all three axes ($\mathbf{A_{EE}}$) indicates the intensity of activities. HR: Detection of heartbeat peaks relies on identification of local maxima ($\mathbf{N_{HR}}$) in 20-50 Hz band-passed waveforms ($\mathbf{Z_{HR}}$). RR: Zero-crossing nodes ($\mathbf{N_0}$) of the decoupled, 0.1-1 Hz band-passed chest-wall motion ($\mathbf{Z''}$) from three-axis measurements serve as the basis for RR estimation. TT: The talking signals feature pronounced harmonics ($\mathbf{P(f_0^1)}$ and $\mathbf{P(f_0^2)}$) of

fundamental frequencies ($\mathbf{f_0^1}$) in the spectrogram analysis ($\mathbf{P(f)}$). SC: The broadband swallow-like events ($\mathbf{N_{Match}}$) correspond to occurrences of peaks ($\mathbf{N_S}$) in both low-passed and high-passed signals ($\mathbf{S_1}$, 0.1-5 Hz; $\mathbf{S_2}$, >100 Hz). The algorithm outputs swallow events $\mathbf{N_{SC}}$ that do not overlap with talking or activity periods. **b**-**f**, Application of the signal processing flow to the representative MA data (Fig. 17) for EE (**b**), HR (**c**), RR (**d**), TT (**e**), and SC (**f**) analysis.

In practice, MA measurements consist of data streams that superpose physiological information from a multitude of sources. A processing flow that exploits the characteristic time-frequency features demonstrated in Fig. 17 enables separation of key events, each of relevance in medical and/or fitness monitoring, i.e. energy expenditure (EE), heart rate (HR), respiration rate (RR), swallow counts (SC), and talking time (TT) (Fig. 21a).

Application of these strategies on the data in Fig. 17 demonstrates the scheme (Figs. 21b-f). Fig. 21b summarizes the EE over 2 s, 50% overlapping moving averaging window as a sum of all-axis low-frequency (1-10 Hz) band-limited root-mean square (BLRMS) data[53]. The result allows classification of activity levels from low (sitting $\sim 10^{-2} g$) to medium (walking$\sim 10^{-1}\ g$) to high (jumping $\sim 10^{0}\ g$) on a logarithmic scale.

Analysis of HR begins with the application of a bandpass filter ($f_{low} = 20$ Hz, $f_{high} = 50$ Hz) to the z-axis acceleration data to suppress noise outside the frequency range of interest. Cardiac pulses correspond to local maxima greater than 0.005 *g* in the time series of these band-passed signals, ignoring intervals shorter than 0.33 s (~180 beats per minute, or BPM) and longer than 1.2 s (~50 BPM). Applying a 5 s, 50% overlapping moving window average to peak-to-peak intervals yields a running estimate of HR (Fig. 21c). The peak-detection algorithm, however, cannot operate reliably with motion artifacts that involve large impacts and associated temporal and spectral features that coincide with those due to comparatively subtle cardiac mechanics.

Measurements of RR are particularly sensitive to ambulatory signals due to overlaps of these two types of signals in the frequency domain (0.1 – 1 Hz). Traditional methods rely on three-axis accelerometers mounted on the chest or the abdomen and allow determination of RR only

during periods that exclude effects of locomotion[16,17,54]. Simple/weighted sum methods (e.g. Principal Component Analysis) can make use of the multi-axis information[18]. In the approach reported here, a noise subtraction algorithm exploits time-synchronized three-axis acceleration measurements to extract respiration signals at all activity levels. The detection mechanism relies critically on the SN mounting location and orientation (Figs 5. a, b), where the z-axis and x-axis measurements are both sensitive to chest-wall motion, while the y-axis acceleration is mainly associated with core-body motions.

The wavelet cross spectrum of two time series, x_n and y_n, where $n = 1,2, \dots, N$ is:

$$C_{xy}(b,n) = C_x^*(b,n)C_y(b,n) \tag{21}$$

where $C_x(b,n)$ and $C_y(b,n)$ denotes the CWT of x and y at scales b and positions n. The superscript denotes the complex conjugate. The coherence projection for the common mode signal embedded in y_n becomes,

$$C_{y'}(b,n) = \frac{C_{xy}^*(b,n)}{C_{xx}(b,n)} \cdot C_x(b,n) \tag{22}$$

We kept wavelet transform coefficients with wavelet coherence $R_{xy}^2(b,n) > 0.8$, where

$$R_{xy}^2(b,n) = \frac{\left|C_x^*(b,n)C_y(b,n)\right|^2}{|C_x(b,n)|^2\left|C_y(b,n)\right|^2} \tag{23}$$

For the specific application in suppressing motion artifacts occurring in the frequency range of respiration cycles, the computation uses Morlet wavelets. We chose a sampling period $\Delta t = 20\ s$ to cover all time scale of interest. The smallest scale for the Morlet wavelets is $s_0 = 2\Delta t$. The CWT discretizes scales with 16 voices per octave. The number of octaves is set to be the nearest integer less than or equal to $\log_2 N - 1$, which in this case is 10. We perform the

continuous wavelet transforms as well as a smoothing operation over 16 scales using the built-in MATLAB™ function “cwt” and “smoothCFS”.

In practice, the wavelet transform projection yields common mode z' values between z- and x-axis measurements. The differential mode z'' between z' and y-axis measurements decouple motions from respiration, according to

$$C_{z'} = \frac{C_{xz}}{C_{zz}} \cdot C_{z,} \tag{24.1}$$

$$C_{z''} = \left(1 - \frac{C_{yz'}}{C_{z'z'}}\right) \cdot C_{z'}. \tag{24.2}$$

Fig. 22a demonstrates an application of the algorithm to simulated signals. Two time-series data, x and z are generated. Both data carry a large amplitude chirp signal in common to mimic the time non-stationary motion artifact, as well as a random gaussian noise of same distribution. A differential sinusoidal signal is added to z to simulate the respiration signal. The algorithm detects the common mode chirp signal between x and z and recovers the differential sinusoidal signal with gaussian noise in z.

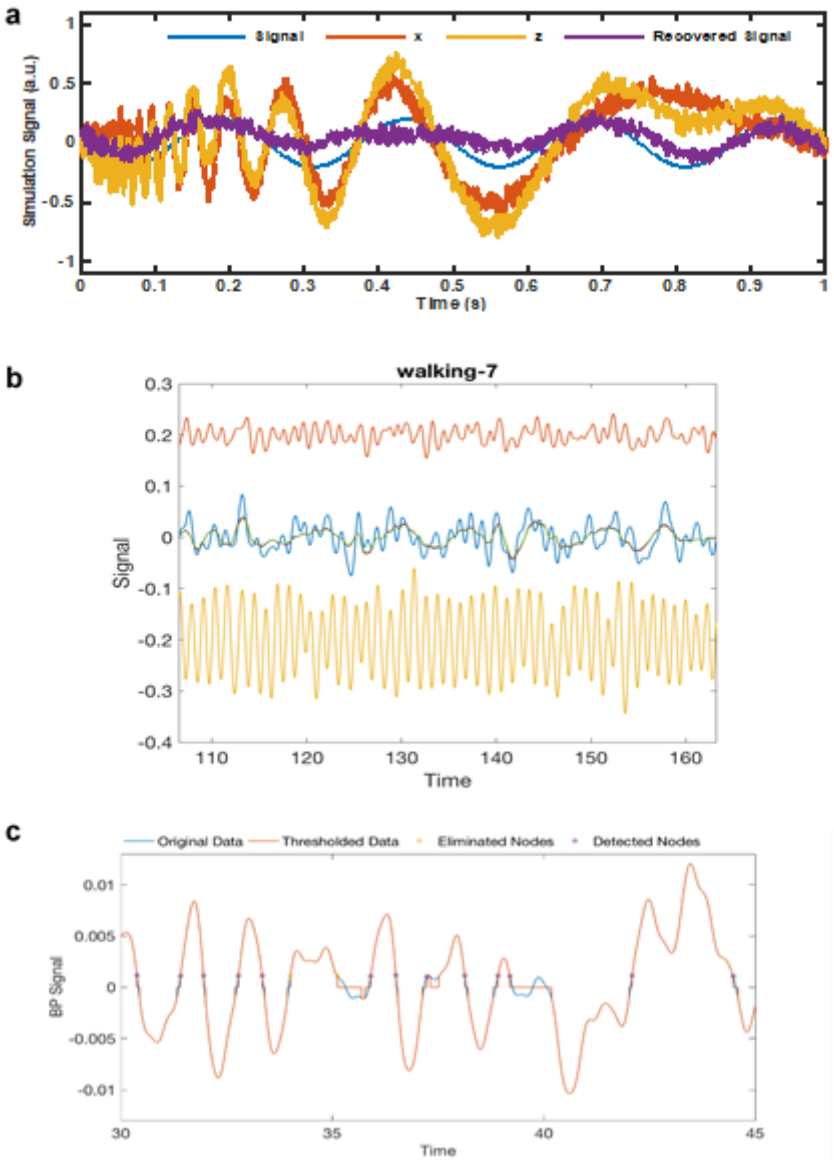

Fig. 22 | Applying CWT subtraction methods to simulation and experimental signal. (a) A numerical simulation test for performance of wavelet cross spectrum analysis. The algorithm detects the common mode (a large amplitude chirp) between X and Z and recovers the differential sinusoidal signal embedded in Z. **(b)** A sample wavelet cross spectrum analysis for chest-wall motion decoupling using three-axis acceleration measurements. The 0.1-1 Hz band-passed x- and y-axis data is offset by 0.2 g for visualization purposes. **(c)** Zero-crossing nodes detected from the extracted signal. A dynamic threshold equal to a tenth of the standard deviation of 1 min data eliminates the effects of small-amplitude ripples that appear on top of the general respiration pattern.

Fig. 22b presents the subtraction results from sample experimental measurement, using the three-axis acceleration data acquired from a healthy-normal subject during walking. The

algorithm suppresses the fast motion artifacts and recovers the slower respiration patterns. Fig. 22c shows a sample detection for zero-crossing nodes using sample extracted respiration signal. A dynamic threshold, set as a tenth of the standard deviation of data collected for 1 min, eliminates the effects of small-amplitude ripples that appear on top of the general respiration pattern.

Fig. 21d compares the band-passed ($f_{low} = 0.1$ Hz, $f_{high} = 1$ Hz) z-axis measurement with z''. As opposed to traditional time-frequency analysis approaches for RR[55,56], a search for zero-crossing nodes of z''determines the average time-span of inspiration-expiration cycles $\bar{T}$ in one minute, as the basis for estimating RR as $60/\bar{T}$ breaths-per-minute (BPM) (Fig. 21d). The direct counting method accounts for the time non-stationary nature of respiration during physical activities. An adaptive threshold of 10% of the standard deviation of the data helps reduce miscounting associated with small-amplitude and fast ripple features on top of the overall 1-min respiration pattern (Fig. 21d).

Signals that arise from speech involve the prominent presence of a second harmonic of the fundamental frequency f_0^1 in the expected frequency range and magnitude (Fig. 21e). The talking time detected in this manner appears as shaded regions in Fig. 21e. Given that $P(f_0^1)$ is a local maximum of power spectral density $P(f)$ in the range of the human voice ($f_0^1 < 160$ Hz for male subjects, $150\text{ Hz} < f_0^1 < 400$ Hz for female subjects) (Fig. 21e), the algorithm searches for a local maximum $P(f_0^2)$ in the frequency range $\frac{3}{2}f_0^1 < f_0^2 < \frac{7}{2}f_0^1$ and identifies speech if the search matches the anticipated harmonics behavior within a tolerance distance $\left|f_0^2 - 2f_0^1\right| \leq 10$ Hz. Instances with $f_0^2 < 120$ Hz and $P(f_0^2) < 5 \times 10^{-3}\ g/\sqrt{Hz}$ are not considered.

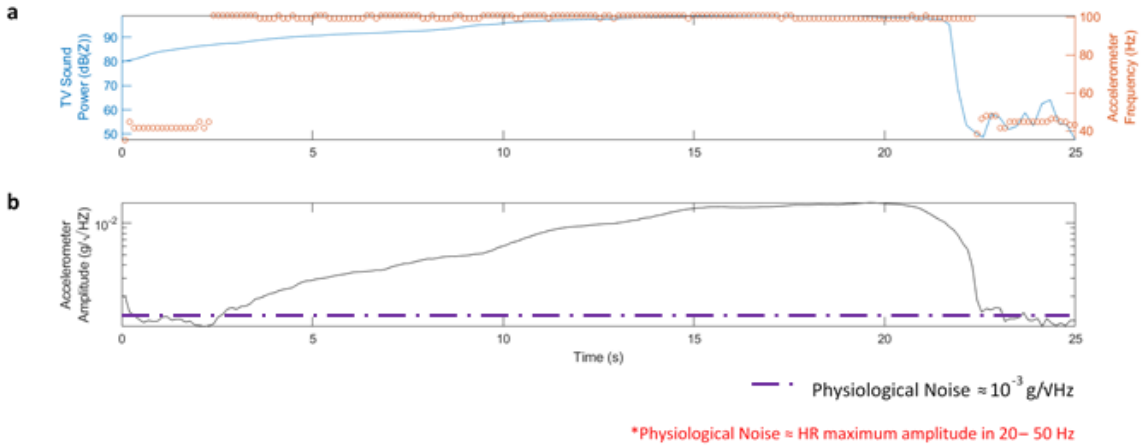

Fig. 23 | Device sensitivity test to 100 Hz ambient TV sound. (a) The device is responsive to ambient sound that is louder than 87 dBZ, which was measured by the microphone. **(b)** Even though the device picks up the ambient sound starting at 87 dBZ, its effect in the accelerometer amplitude is not significant until it reaches 98 dBZ. Even when the ambient sound reaches the power of 98 dBZ, the accelerometer amplitude ($2x10^{-2}$ g/√Hz) is smaller than that of the general speech signal (10^{-1} g/√Hz).

Using this device to determine TT has distinct advantages over methods relying on microphones due to its insensitivity to airborne acoustics. Tests in controlled, acoustically isolated rooms show that external sounds at 100 Hz and 90 dB(Z), appear as signals with amplitudes of only $2x10^{-2}$ g/√Hz (Fig. 23) while speech at a similar frequency and at 65 dB(Z) on microphone (near the audible threshold) appears on the device with maximum amplitude of 10^{-1} g/√Hz (Fig. 24).

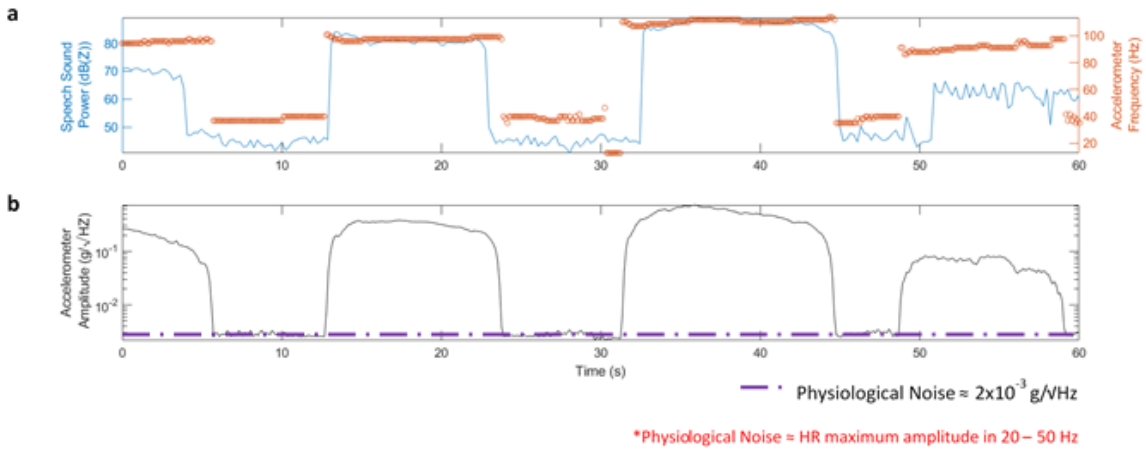

Fig. 24 | Device sensitivity test to vocal sound. (a) The device is sensitive to vocal sound that is softer than 65 dBZ, which was measured by the microphone. **(b)** Even when the vocal sound is ~65 dBZ, the device picks up the vocal fold vibration with the adequate amplitude (10^{-1} g/√Hz) for the signal processing algorithm.

The effects of ambient sounds can, therefore, be neglected entirely in almost all practical scenarios.

Swallowing events feature both low-frequency mechanical motions (0.1-5 Hz) and high-frequency acoustic components (100-800 Hz). Based on this observation, the algorithm for SC detects swallow events as high-frequency and low-frequency peaks that occur, coincidentally, within a 2 s time window (Fig. 21f). For the purpose of this algorithm, swallow events are only considered if they are separated by more than $0.2\ s$ from talking events and by more than $0.5\ s$ from active periods ($EE > 0.05\ g$).

Human subject evaluations in practical scenarios.

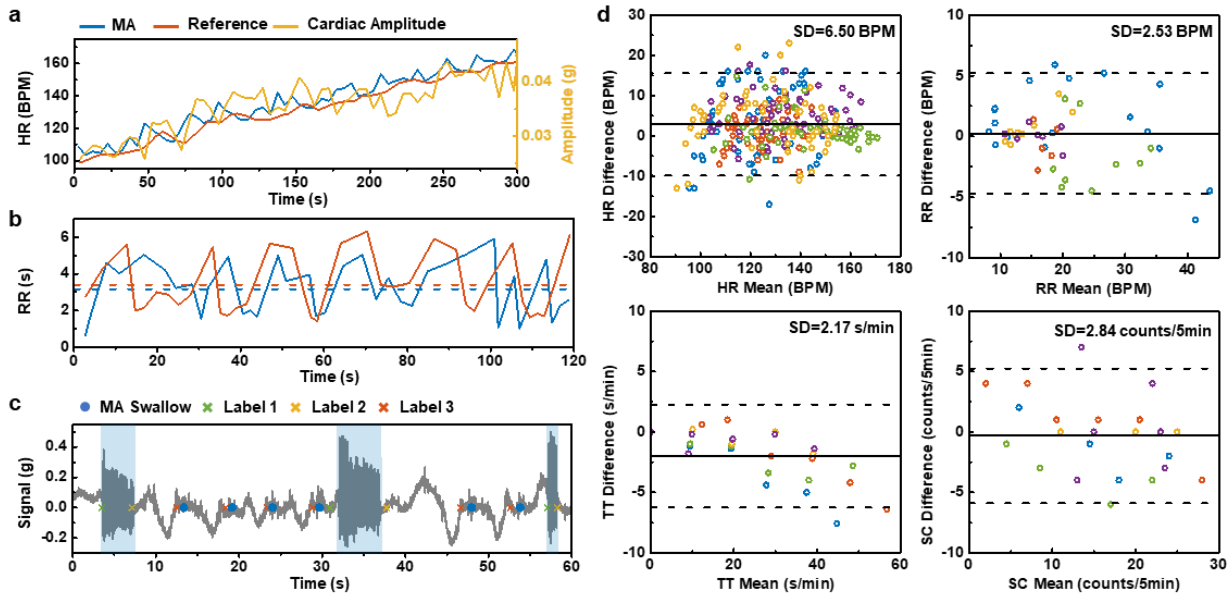

Fig. 25 | Results from mechano-acoustic (MA) data recorded at the suprasternal notch (SN) in field studies with comparisons to reference measurements. a, HR measurements during a 5-minute interval during exercise to increase the HR using MA signals and a Polar® hand-grip monitor. The cardiac amplitude, measured as the peak acceleration amplitude, exhibits a correlation with the HR measurement. **b**, RR measurements during a 2-minute interval using MA data and manual counting. The subject counts peak-to-peak intervals but the algorithm counts zero-to-zero intervals, thereby leading to a difference that appears as a time lag. **c**, A sample 1-min dining-scheme experiment comparing the reference labeling of events (cross) with the MA device detection (dot). For reference labels, label 1 and 2 mark the start and end of talking, while label 3 marks the occurrence of swallowing. **d**, The Bland Altman analysis for HR, RR, TT and SC. The solid and dashed lines represent mean difference and standard deviation x 1.96, respectively. Different colours represent the five different healthy normal subjects.

Field studies in physical exercise and in dining demonstrate these data acquisition and processing schemes. The SN served as the mounting location in all cases. The first involves cycling and resting on a stationary bike, with HR between 50 to 180 BPM. For the HR monitoring session, the subject rode a cycling machine with a HR sensor (Polar®) interfaced to electrodes on the handle, yielding reference HR values every 5 s. The session began when the HR reached over 90 BPM. The subject cycled to increase the HR by 10 BPM each min until reaching 170 BPM as shown in the Fig. 25a.

In a separate set of experiments, subjects manually count the number of breathing cycles per five minutes during normal sitting, walking and running activities as a reference for RR. For dining, each subject talks and swallows for five minutes according to a prescribed protocol.

For the swallowing experiment, the duration of each session was 5 min. The subject talked and swallowed water for a prescribed number of times per minute throughout the session. The talking duration was 10-s per session, and the swallowing occurred every 10 s from the end of a previous talking session to the start of a subsequent one.

Here, periodicity (with a time scale of ~10 s, significantly longer than the time scale of event detection of ~ 0.1 s) in the activities facilitates tracking of numbers of events. In each minute of the n^{th} test $(n = 0, \dots, 5)$, the subject talks for $n \times 10$ s, then swallows at $(n + k) \times 10$ s, $k = 1, \dots, 6 - n$. During data acquisition, each subject marks the start and end of the talking period as well as swallowing instances using logging buttons on an app that runs on the smartphone used for data acquisition (Fig. 5d). The data set includes five subjects for each scenario. For the cycling test, each subject cycle for 5 min. Applying a 5 s, zero overlapping moving window generates a total of 301 samples for comparison. RR experiments yield 56 samples across different activity levels, wherein each sample is an average RR over one 5-min test. A total of 26 dining tests generate average values for TT and SC over each 5-min test.

Figs. 25a-c shows the example results of MA measurements versus reference data. In the exercising scheme, the MA HR follows the reference HR from 100 to 160 BPM over a time period of 5 min under cycling activity, as in Fig. 25a. In addition to HR, the MA device captures the amplitude of the cardiac activity, which exhibits an approximate linear correlation to HR. In Fig. 25b, the MA RR follows the manually counted RR for this 2-min segment during walking. The mean RR values in both cases, marked by the dashed lines, closely match. Fig. 25c is a 1-min

demonstration of the dining scheme. The MA talking and swallowing events agree with the label reference.

Figs. 25d shows Bland-Altman plots for HR, RR, TT, and SC. The solid and dashed lines mark the mean and 1.96 times the standard deviation of the difference between MA measurements and reference values, respectively. HR has a mean difference of 2.8 BPM and a standard deviation A_{RMS} of 6.5 BPM. This limit of agreement is comparable to that observed with some of the best commercial devices for HR monitoring during physical activity (A_{RMS}= 4-29 BPM). RR has a mean difference of 0.3 BPM and a standard deviation of 2.5 BPM. As with HR, this difference is comparable to that of conventional monitors of RR (A_{RMS} = 2-3 BPM).

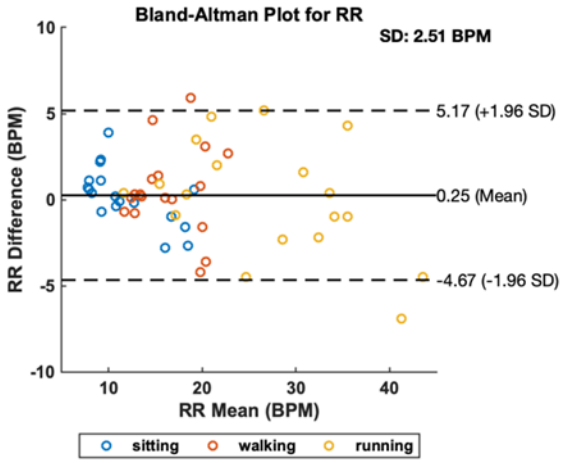

Fig. 26 | Bland-Altman analysis for RR under different activities. For sitting, the mean difference between MA and reference measurements is 0.21 BPM and the standard deviation A_{RMS} = 1.63 BPM (N=18); for walking, the mean difference is 0.52 BPM, and A_{RMS} = 2.43 BPM (N=19); for running, the mean difference is 0.01 BPM and A_{RMS} = 3.34 BPM (N=19). N indicates the sample size for each scenario.

A categorized statistical analysis indicates that the standard deviation error increases slightly with intensity of the activity (Fig. 26). TT has a mean difference of -2.0 s/min and a standard deviation of 2.2 s/min. SC has a mean difference of -0.7 counts/5 min and a standard deviation of 2.8 counts/5 min.

3. Applications

I. Sleep Study

The materials from this section is from: 'Lee, K., Ni, X., Lee, J.Y. *et al.* Mechano-acoustic sensing of physiological processes and body motions via a soft wireless device placed at the suprasternal notch. *Nat Biomed Eng* **4,** 148–158 [2020], [Nature Research]'

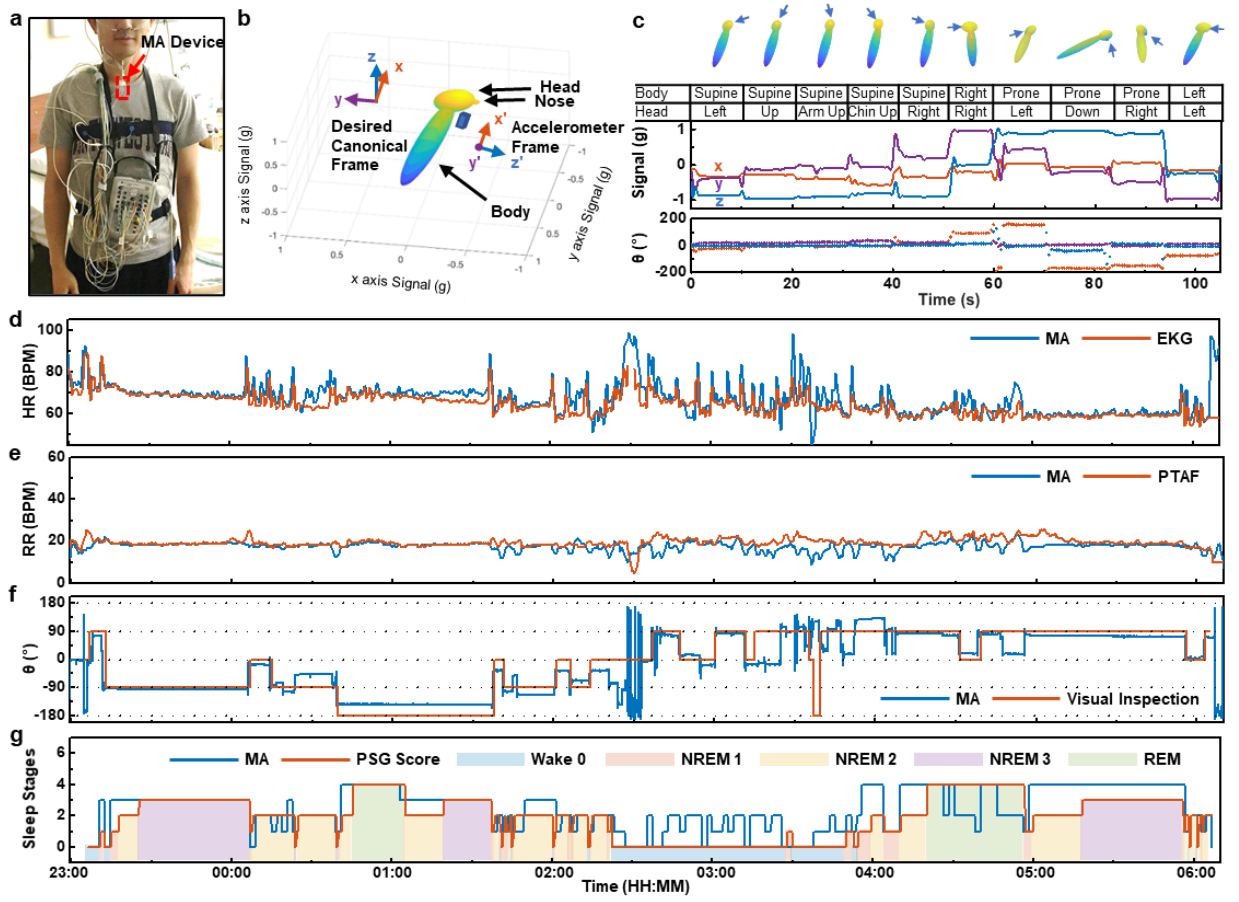

Fig. 27 | Application of mechano-acoustic (MA) sensing from the suprasternal notch (SN) in clinical sleep studies. a, Image of the MA device on the SN (red box) along with a gold-standard polysomnography (PSG) sensor ensemble, including devices for recording Electrocardiograms (ECG), Electroencephalograms (EEG), and Electrooculograms (EOG) and for Pressure Transducer Airflow (PTAF) measurements, along with an Abdomen Strain Gauge, Thorax Strain Gauge and Thermistor. **b**, Avatar representation of a subject with the associated device frame and canonical frame. **c**, Body orientation calibration test. The arrows indicate the position of the nose. **d**, Comparisons of heart rate determined with the MA sensor and with the ECG recordings during sleep. **e**, Comparisons of the respiration rate determined with the MA sensor and with the nasal Pressure Transducer Airflow (PTAF) recordings during sleep. **f**, Comparisons of the body orientation determined with the MA sensor and by visual inspection by a sleep technician. **g**, Inference of sleep stages based on multi-band z-axis signal power of MA measurements in comparison to clinically determined sleep stages

Use of MA devices to quantify patterns of sleep represents a potential application in advanced clinical diagnostics. Fig. 27a shows a subject equipped with an MA device on the SN and with a complete suite of conventional polysomnography (PSG) sensors for gold-standard reference measurements. For the sleep study, in addition to the MA device, the subject wore a suite of PSG sensors, including a three channel system for electroencephalography (EEG) on the forehead, two channel leads for electrocardiography (EKG) on the chest, a pair of leads for electromyography (EMG) on the chin, a pair of channels for electrooculography (EOG) on the side of upper left eye and lower right eye, a pressure transducer air flow (PTAF) with thermistor in the nostrils, two strain gauge bands around the chest and abdomen.

A sleep lab technician performs visual observations alongside throughout the study to record changes in body orientation. In addition to HR and RR detection, MA device also monitors quasi-static body orientation continuously.

We analyze body orientation in SO(3) by finding the rotation matrix transforming the nominal gravity vector in the canonical frame $\boldsymbol{g} = [0,0,g_0]$ to the gravity vector measured in the device frame $\boldsymbol{g}' = [a_x, a_y, a_z]$, where the magnitude of gravity is estimated as $g_0 = \sqrt{a_x^2 + a_y^2 + a_z^2}$. We use Rodrigues' rotation formula for computation efficiency[657],

$$\boldsymbol{v}_{rot} = \boldsymbol{v}\cos\theta + (\boldsymbol{k}\times\boldsymbol{v})\sin\theta + \boldsymbol{k}(\boldsymbol{k}\cdot\boldsymbol{v})(1-\cos\theta) \tag{25}$$

where $\boldsymbol{k}$ is the unit vector representing the rotation axis around which vector $\boldsymbol{v}$ rotate an angle θ following right-hand rule. Eq. 25 can be represented in matrix notation, $\boldsymbol{v}_{rot} = \boldsymbol{R}\boldsymbol{v}$, where $\boldsymbol{R}$ is the rotation matrix,

$$\boldsymbol{R} = \boldsymbol{I} + (\sin\theta)\boldsymbol{K} + (1 - \cos\theta)\boldsymbol{K}^2 \tag{26}$$

In the above equation, $\boldsymbol{I}$ is the 3 × 3 identity matrix, $\boldsymbol{K}$ is the skew-symmetric cross-product matrix of $\boldsymbol{k} = [k_1, k_2, k_3]$,

$$\boldsymbol{K} = \begin{bmatrix} 0 & -k_3 & k_2 \\ k_3 & 0 & -k_1 \\ -k_2 & k_1 & 0 \end{bmatrix} \tag{27}$$

Given the two gravity vectors $\boldsymbol{g}$ and $\boldsymbol{g'}$, we compute rotation axis and angle using cross product and dot product of normalized vectors $\widehat{\boldsymbol{g}}$ and $\widehat{\boldsymbol{g'}}$,

$$\boldsymbol{k} = \frac{\widehat{\boldsymbol{g}} \times \widehat{\boldsymbol{g'}}}{\left|\widehat{\boldsymbol{g}} \times \widehat{\boldsymbol{g'}}\right|}, sin\theta = |\widehat{\boldsymbol{g}} \times \widehat{\boldsymbol{g'}}|, \cos\theta = \widehat{\boldsymbol{g}} \cdot \widehat{\boldsymbol{g'}}. \tag{28}$$

If we let $\boldsymbol{K'}$ be the skew symmetric matrix of $\widehat{\boldsymbol{g}} \times \widehat{\boldsymbol{g'}}$, *i.e.* $\boldsymbol{K'} = \left|\widehat{\boldsymbol{g}} \times \widehat{\boldsymbol{g'}}\right| \boldsymbol{K}$. Substituting all expressions to Eq. 26, we obtain rotation matrix,

$$\boldsymbol{R} = \boldsymbol{I} + \boldsymbol{K'} + \frac{\left(1 - \widehat{\boldsymbol{g}} \cdot \widehat{\boldsymbol{g'}}\right)\boldsymbol{K'}^2}{\left|\widehat{\boldsymbol{g}} \times \widehat{\boldsymbol{g'}}\right|^2} \tag{29}$$

We convert the rotation matrix to the corresponding Euler angles in the device frame using MATLAB™ function “rotm2eul”. The rotation angle around the longitudinal axis of body indicates the body orientation of major interest in the sleep study.

Fig. 27b shows an avatar representation of the subject in a left recumbent position, along with the corresponding device and global frames of reference. Rotation matrix to the Euler angles conversion around the body-fixed (intrinsic) axis in z-y-x sequence (MATLAB™ function “rotm2eul”) makes intuitive sense of the rotation operation. The rotation angle θ around the longitudinal x-axis characterizes the major body orientation of interest during sleep, where we

define zero degree as supine and the positive sense as turning right (left-hand rule). Fig. 27c presents a calibration test on rotation angles, in which a subject roll into a series of body orientations. In addition to the supine, prone, left recumbent, and right recumbent positions, the MA signal at the SN reveals additional information associated with the relative rotation of the head against the torso (Figs. 5a and 27c). Figs. 27d-f compare MA devices vs HR derived from electrocardiography (EKG) (1-min window, 50% overlap), RR derived from pressure transducer air flow (PTAF) (2-min window, 75% overlap) and sleep technician inspection measurements of body orientation (0.1-s window, 0% overlap) respectively throughout a ~7-h sleep study on a healthy male (Age 26, Asian/Korean) subject.

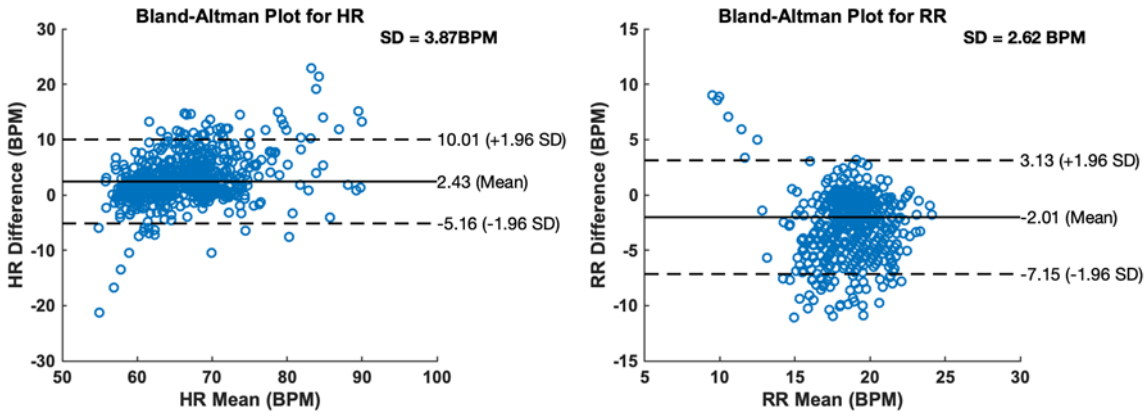

Fig. 28 | Bland-Altman analysis for HR and RR during the 7 h sleep study. HR has a mean difference of 2.4 BPM and a standard deviation A_{RMS} of 3.9 BPM (N = 853). RR has a mean difference of -2.0 BPM and a standard deviation of 2.6 BPM (N = 853). N indicates the sample size for each scenario.

Bland-Altman analysis for HR and RR gives a standard deviation error of 3.9 BPM and 2.6 BPM, respectively (Fig. 28).

As a routine part of clinical care, segments of sleep are classified into four different stages, excluding the wake stage. The duration and frequency of each stage determines the sleep quality.

The four stages are Rapid Eye Movement (REM), and non-REM Stages N1, N2, and N3. REM sleep comprises irregular and high RR and HR, along with the large amplitude electrooculogram (EOG) signals recorded using the PSG suite[58]. Non-REM sleep stages are defined by characteristic features on electroencephalogram (EEG), and although the MA device does not record EEG or EOG data, the results in Fig. 27g suggest some capabilities in quantifying sleep stages by applying machine learning algorithms on MA data obtained during stages determined manually by a clinical expert.

Sleep scoring involves modeling time series sequences with discrete states. Realistically, MA signal features would not tell sleep stages deterministically. We introduce Hidden Markov Model with Gaussian mixture emissions (GMMHMM) to capture the stochastic emission from states to observations. A Hidden Markov Model (HMM) $\boldsymbol{\Phi} = (\boldsymbol{A}, \boldsymbol{B}, \pi)$ encodes a joint probability distribution of generative states sequences $\boldsymbol{\Omega} = \{1, 2, 3, \dots, N\}$ characterized by a set of output observation symbols $\boldsymbol{O} = \{o_1, o_2, \dots, o_M\}$ with an underlying probabilistic dependence. We let s_t denote the state at time t. In the mathematical representation, $\boldsymbol{A} = \{p_{ij}\}$ is a transition probability matrix, where p_{ij} is the transition probability from state i to j. $\boldsymbol{B} = \{q_{ik}\}$ is the output probability distribution, where q_{ik} is the probability of emitting observation symbol o_k in state i. $\pi = P(s_0 = i)$ is the initial state distribution. Sleep stage identification is a learning problem, *i.e.* given a sequence of observations $\boldsymbol{X} = (X_1, X_2, \dots X_T)$, to find the best characteristic model parameter $\boldsymbol{\Phi}'$ so that the joint probability $\prod P(X|\Phi)$ is optimized through expectation-maximization (EM) algorithm. For the specific application, we use sklearn.hmm.GMMHMM module to train the HMM parameters and infer the hidden states. We randomly initialize the HMM parameter values. The prior distribution over initial states is uniform. The EM algorithm runs for 10 iterations or until convergence.

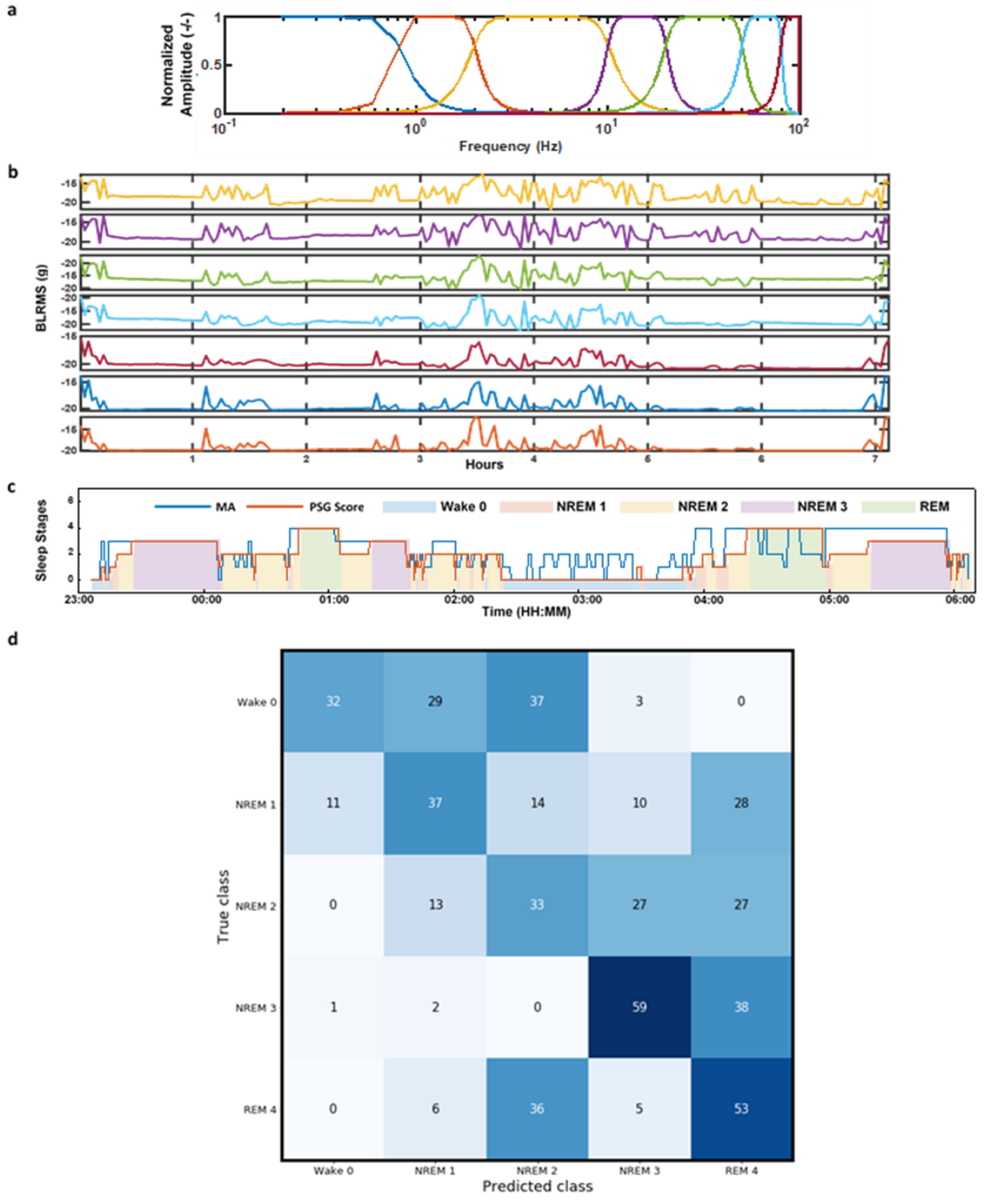

Fig. 29 | Feature extraction and classification of sleep stages. (a) The filter-bank for energy feature generation **(b)** The time series of multi-band energy extracted from z-axis acceleration measurements. **(c)**

The inference of sleep stages based on the multi-band signal power in comparison with clinically determined sleep stages. **(d)** The confusion matrix for the success rate of the classification.

In the sleep study, the input features to the GMMHMM model take the form of multi-frequency band signal power, characterized by the band-limited root mean square (BLRMS) in 120-s time epoch, as our input features to the GMMHMM model. The band choices feature the 0.1-0.8 Hz respiration signals, as well as the 20-50 Hz cardiac signals. We choose in total seven bands for a balance between the characterization of system complexity and the feature representation for generality. Fig. 29a shows the full feature extraction filter-bank. Fig. S29b shows the time-series of each band power for the sample 7-hour sleep data presented in the main text, Fig. 27.

For the HMM model, we set the number of states to be $N = 5$. Multi-band z-axis signal power on a logarithmic scale serves as the observable clustering features to classify the five sleep stages labeled as 0 to 4 from Wake to Rapid Eye Movement (REM). The multi-band choices are 0.1-0.8 Hz for respiration, sub-bands in the range 0.8-20 Hz for body motions, and 20-80 Hz for cardiac activity. Gaussian mixture emissions determine the probability of multi-band power observations given the state. The inferred hidden states capture the overall trend of clinician determined sleep scoring.

The HMM model developed upon small dataset is a simple clustering method providing no information about the labeling. We permute the inferred states for all combinations of labeling and assign each class to a stage according to a minimum marathon distance optimization. Fig. 29c presents the final classification result in comparison with the clinically determined sleep stages. Fig. 29c summarizes the success rate in a confusion matrix.

The algorithm exploits multi-band z-axis signal power on logarithmic scales as the observable clustering features, with a multi-band choice featuring the 0.1-0.8 Hz for respiration

signals, sub-bands in the range 0.8-20 Hz for motions, as well as 20-80 Hz for cardiac signals. As shown in Fig. 27g, the optimized inferred hidden states capture the overall trend of gold-standard sleep scoring. The success rate for a simple binary wake/asleep classification is 82%. Fig. 29 includes a complete confusion matrix for multi-classes. Advanced analytics, a subject of on-going work, may enable further classification.

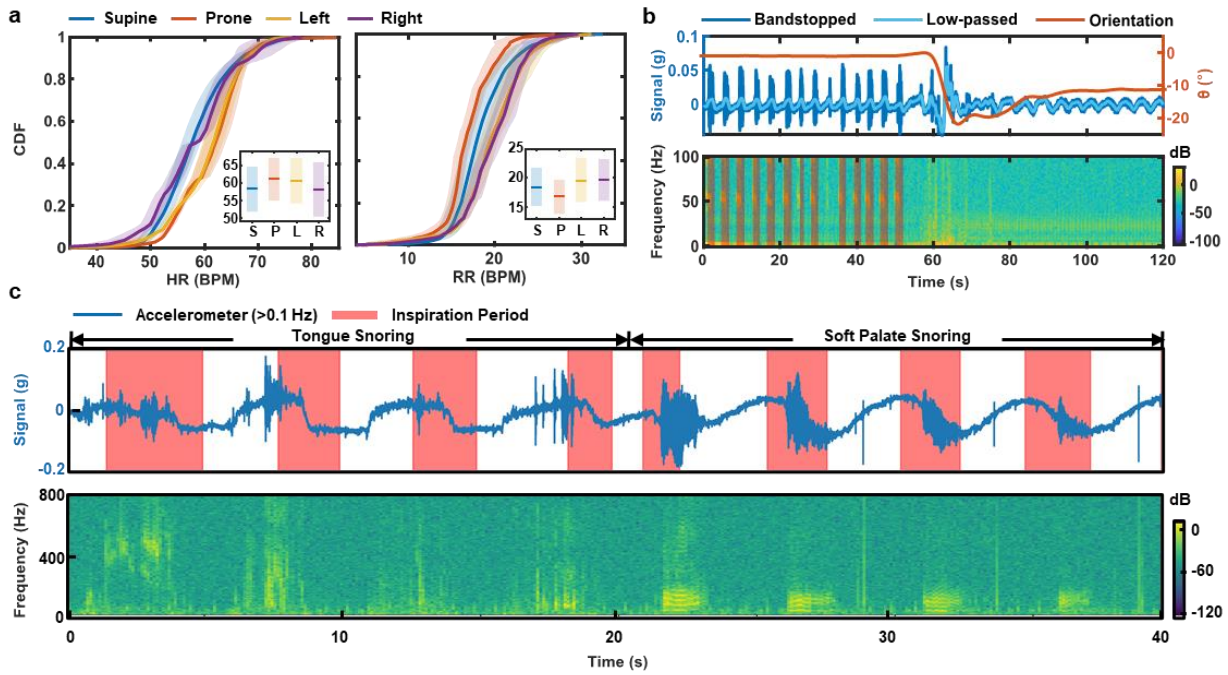

Fig. 30 | Insights into sleep patterns determined by mechano-acoustic (MA) sensing from the suprasternal notch (SN). a, Cumulative distribution function (CDF) of HR and RR in supine, prone, left, and right body orientations. The inset indicates mean (line) and standard deviations (bars) of the measurements between subjects. **b**, Sample data that illustrate the transition from snoring to quiet periods, plotted along with body orientation. **c,** Comparisons of different types of snoring mechanisms and their characteristics in acceleration and frequency.

The wireless operation and the ability to track sleep with a single device facilitates use in home settings and in a way that does not alter natural patterns of sleep, as significant advantages over PSG systems. Insights obtained in this way can guide behaviors to optimize sleep quality. For example, Fig. 30a shows the cumulative distributive function (CDF) of HR and RR statistics, extracted from data collected from eight healthy normal subjects over five nights of sleep in the

home, classified into four body orientations (supine: $-45° < \phi < 45°$, left: $-135° < \phi < -45°$, right: $45° < \phi < 135°$, prone: $\phi > 135°$ or $\phi < -135°$). The solid lines are mean CDF values for all subjects. The shaded regions mark the standard deviation variance between subjects (Fig. 30a). The inset compares the mean and standard deviation of HR and RR respectively generated from the averaged CDF for different body orientations. The results indicate that the HR is highest, on average, in Left-recumbent/Prone-approximate positions. The RR is higher in recumbent positions but lower in prone positions, with supine as a reference. According to previous studies[59–61], such changes may relate to reductions in venous flow, with resulting blood pressure reductions and/or increases in reflexive sympathetic nervous activity.

As expected, the device is sensitive to snoring signals as well. Fig. 30b shows time series and time-frequency analysis of a representative ~50 s period of snoring followed by a transition to a ~50 s period of quiet sleep from a healthy female subject. The time series superimposes the band-stopped ($f_{low} = 1$ Hz, $f_{high} = 60$ Hz) z-axis acceleration measurement with the band-passed ($f_{low} = 0.1$ Hz, $f_{high} = 1$ Hz) respiration signal, to show that snoring occurs during exhalation. The snoring-to-quiet transition in the sample of Fig. 30b correlates with a slight left-ward head versus torso rotation of ~$10°$. The time-frequency analysis shows a clear presence of harmonics with fundamental frequency of ~50 Hz, which falls in the range of the natural frequencies of the soft palate and tongue structures[62,63]. The TT algorithm can be adapted to search for snoring time (ST) by shifting the fundamental frequency search range to the lower frequencies ($20 \text{ Hz} < f_0^1 < 80 \text{ Hz}$). The auto-detected ST appears as shaded regions of the spectrogram plot. A tendency for snoring occurs during inspiration due to the Bernoulli effect[64]. As the throat starts to narrow, the velocity of flow may increase which drops the pressure in the airway behind the tongue and soft palate, thereby drawing the tissues together. The timing relative to the inspiration period may indicate the anatomical origin of snoring: tongue, or soft palate. Fig. 30c compares the snoring signal

generated by these two different mechanisms. From 0 to 16 s, the subject artificially obstructs the airway by pushing the tongue to the back of the throat, then the subject artificially generates the snoring sound by vibrating the soft palate. The results clearly demonstrate that tongue snoring has inconsistent timing relative to the respiration cycle as compared to soft palate snoring. Moreover, the spectrogram illustrates that snoring generated by the tongue appears at a higher frequency range than that of the soft palate, as might be expected based on the mechanics of these processes.

II. Stroke Rehabilitation

Stroke affects more than 795,000 people per year in the United States. It is a leading cause of long-term disability, which includes a reduction in mobility and communication skills. More than half of survivors over age 65 struggles with these post-stroke diseases. Movement deficits are a hallmark of stroke, resulting from weakness or paralysis on one side of the body. Typical outcomes of stroke are difficulty walking and reduced walking speed, difficulty using the affected upper arm, the rigidity of the limbs, impaired balance, and impaired speech, language, and cognition. However, post-stroke patients can improve from these deficits. Early clinical treatments, including physical rehabilitation and medication, aim to build on these improvements and return stroke patients to a certain level of function before hospital discharge. The stroke severity and ability to function in the community determine the duration of hospitalization. However, determining whether a patient has recovered sufficiently for discharge depends on subjective and qualitative measures.

Currently, the evaluation of stroke patient recovery relies on infrequent clinical assessments, performance-based rehabilitation measures, and patient self-reports. Performance-based rehabilitation measures limit sensitivity, reliability, and validity in identifying changes or clinical efficacy of treatment or recovery progression. The patient-reported recovery

is rather biased. Thus, there is a strong need for objective, reliable, and continuous monitoring of stroke patients to assist clinicians and therapists in making informed decisions about stroke treatment and recovery.

In this study, the mechanoacoustic sensor continuously monitors stroke inpatients and allows clinicians and therapists to offer more customized interventions during inpatient procedures. Specifically, a wireless sensing system enables quantitative measures of body function and activity and tracks biometric data and communication. Clinicians and therapists would have access to a patient history of sensor-based biometric and activity data, allowing them to measure recovery and assign treatment after stroke more fully.

Aphasia

The sensor is more sensitive to the mechanical and acoustic signals of the body than the ambient mechanical and acoustic noise (Figs. 23 and 24). Notably, high energy and distinct signals like vocalization predominate in most of the signals and noise that co-occur. Relying on these unique characteristics of the sensor and the vocalization signal, we deploy the sensors to an aphasia rehabilitation focus group. The patients exercise vocalization and restore their linguistic ability through the practices of assisted communication with each other.

Conventionally, the clinician attends the focus group to assist the patients and record their conversation. After the session, the clinician listens to the conversation again, and qualitatively score the degree of the impairment for each patient. This assessment process is prone to human

error and time-consuming, especially when the recordings involve multiple people communicating with each other and convoluting the recorded message.

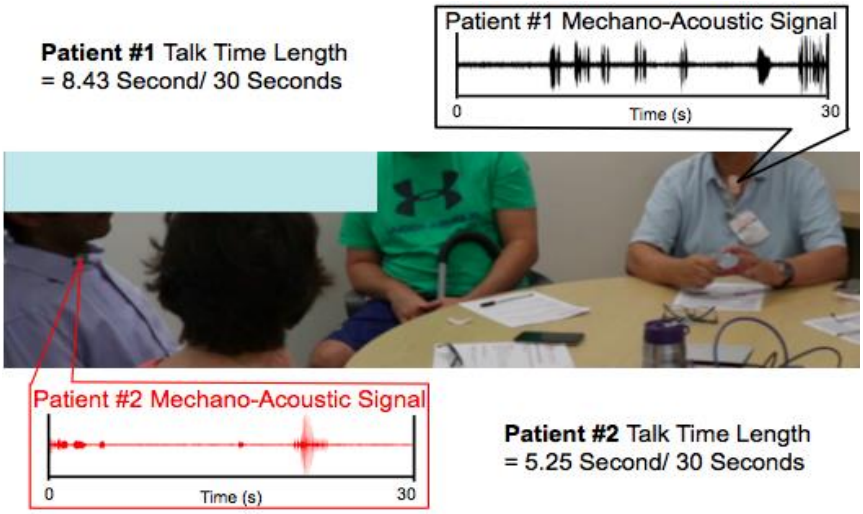

Fig. 31 | Quantifying talk time with a cohort of 3 stroke survivors with aphasia and a speech-language pathologist. Demonstrating the sensor's ambient noise insensitivity by plotting signals from the conversation between two patients. Each signal only shows the vocalization of the individual wearing the sensor, but not the sound from others.

In this aphasia study, two participants wore the sensor on the suprasternal notch and carried on the conversation. Each sensor only picked up the vocalization of the patient wearing the sensor by measuring the vocal fold vibration and blocking out the ambient sounds in the room (Fig. 31). At the end of the session, the talk time algorithm quantified the duration and frequency of the conversation from the MA signal recordings by selecting the vocalization features, as demonstrated in the earlier section.

As a result, the sensor accurately recorded the mechano-acoustic laryngeal data and calculated total talk time for the two subjects during the book club and conversation group. The full recording time was 311 minutes, and the subject 1 sensor measured 51 minutes of talk time, and the subject 2 sensor measured 33 minutes of talk time. These measurements were longer than the manual measurements using the microphone recordings and stopwatch. The discrepancy may be due to the human error in manual counting and the algorithm that considers the pause between the short interval between words and the talk time. Figs 32 and 33 show 5-

minute segments of their talk time for Subjects 1 and 2, respectively. Subject 1 shows an irregular speaking pattern, with periods of lengthy utterances, while Subject 2 shows more interjections or brief comments throughout the time. We also surveyed the user experience. The participants did not feel any irritation at the sensor placement site. They noted that they could not feel the sensor while talking, swallowing, or moving their heads or necks.

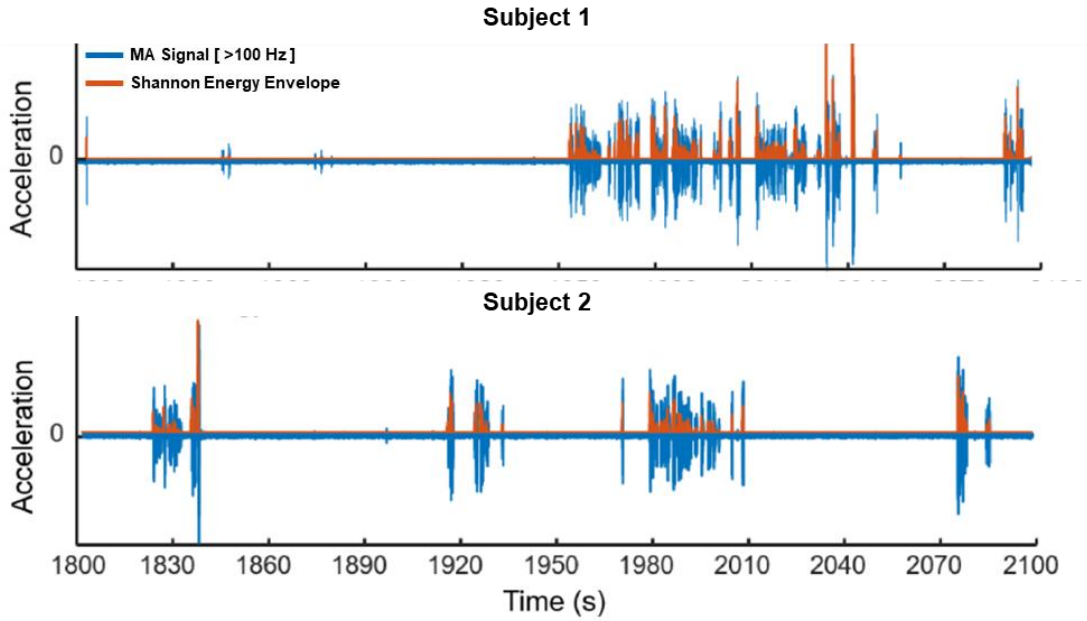

Fig. 32 | 5-minute segments of MA signals. The 100 Hz, highpass Butterworth filter, keeps the MA signal associated with the vocalization. The red curve is the envelope of the MA vocalization signal that groups the utterance of words and bases the calculation of the talk time.

This pilot study demonstrates the feasibility of a flexible, wearable, wireless MA sensor to accurately measure the talk-time of an individual speaker with aphasia in a setting with an ambient conversation. The sensor is comfortable and unobtrusive, and it accurately captures the total talk-time for persons with aphasia throughout the day. Future research will examine the sensor's use in the home and community to assess functionality, usability, and durability. Data from this sensor can inform future treatments, as clinicians will have objective data from multiple communication environments.

Dysphagia

Recalibrating respiratory-swallow phase patterning through Respiratory-Swallow-Training (RST) results in significant airway protection and swallowing biomechanical benefits. However, identifying patterns of the chest and abdominal wall movements outside of research settings is cumbersome and expensive, as the current RST system, called respiratory inductance plethysmography, requires specialized non-portable sensors and peripheral apparatus (Fig. 32), which consists of a nasal cannula pressure transducer, chest and abdominal strain gauge band, table-top signal amplifier, and a laptop with wires connecting the sensors and amplifiers (Fig.33).

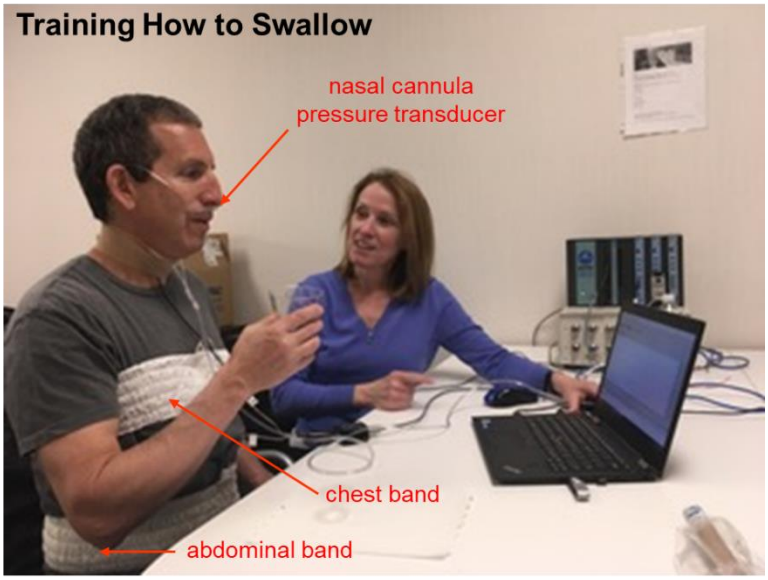

Fig. 33 | Current gold-standard system for Respiratory-Swallow-Training. It consists of a nasal cannula pressure transducer, chest and abdominal strain gauge band, table-top signal amplifier, and a laptop. Wires and tubes create a connection among the sensors and peripheral instruments**.**

In this study, we compare respiratory signals recorded during swallow trials using the MA sensor to the respiratory inductance plethysmography recordings, current gold-standard for the RST. A total of 214 swallows were analyzed. There was a high percentage of agreement (89%) and a strong, positive correlation ($r = 0.92$, $p < .05$) between the number of swallows detected by the MA sensor and the gold standard respiratory inductance plethysmography sensors and the

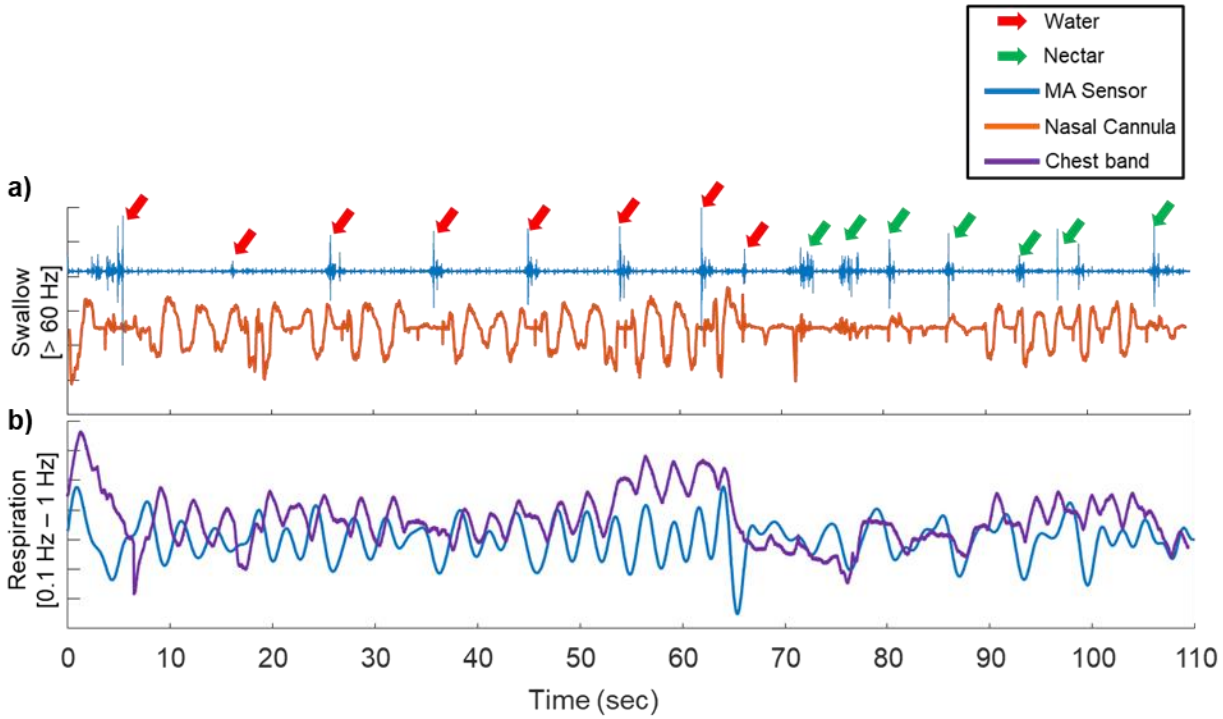

Fig. 34 | Demonstration of swallow and respiration detection from the MA sensor and comparisons to the ground truth sensor: nasal cannula pressure transducer and chest band. a) The nasal cannula data in orange shows a clear sign of swallowing incident with the apparent impulse in the signal from the flat baseline. These impulse signatures match well with the sharp impulse signatures from the high-passed MA data. The high passed MA signal also has potential in differentiating the constituency of the swallowed food based on the waveform of the impulse signal. **b)** Mechanocaoustic sensor follows the cadence of the chest band respiration signal as well, indicating its potential in measuring the respiration cycle.

nasal cannula pressure transducer (Fig.33). The MA sensor and the respiratory inductance plethysmography systems for respiratory-swallow phase patterning agreed well (percentage of agreement: 100%, $\kappa_{weighted}$ = 1.00). A Wilcoxon signed-rank test showed no statistically significant differences between estimated lung volumes at swallow initiation (p = .101). Our findings suggest that the MA sensor detects swallows and respiratory-swallow phase patterning with high accuracy. These results also indicate that lung volume at swallow initiation can be estimated using the sensor.

III. Scratch Study

In dermatology, there need to be more objective measures of disease severity. While itching is an important symptom in many skin diseases, it is the hallmark of atopic dermatitis. Thus,

scratching behavior provides a potentially quantifiable measure of itching intensity and frequency. However, patients' self-reported itch severity via standardized surveys and visual scales has shown a weak correlation to visually observed scratching behavior. Many experts suggest that these subjective measures of itch are particularly prone to anchoring bias and subject to experimental error. There is a need for more accurate, reproducible, and scalable tools to quantify the intensity and duration of pruritus.

The accepted gold-standard for measuring scratching is direct visual inspection captured by a video camera. However, visual inspection is time-intensive, requires manual coding, and not suitable for broader clinical deployment. Actigraphy with embedded accelerometers in a wristwatch format has been studied as a possible wearable scratch sensor. While there is a significant correlation with visual inspection regarding scratching behavior, there are several limitations of actigraphy. The actigraphy cannot differentiate true scratching from other common voluntary and involuntary arm movements (e.g., waving, brushing teeth). Of the wide range of scratching motion, subtle movements of scratching localized to only the fingers are difficult to capture by a wristwatch-based accelerometer. With its relatively coarse time and sensing resolution, fine measurement of the scratching duration and intensity is challenging. The rigid, bulky form factors of wristwatch based actigraphy remain a significant limitation in the use of the pediatric population.

There have been many other efforts in quantifying scratching. For example, one group has developed a wearable wrist-based microphone that demonstrates higher agreement with direct observation of scratching behavior by using an acoustic signal. It can differentiate scratching movements from other voluntary arm movements. However, this system remains bulky, rigid, and uncomfortable to wear. Furthermore, the acoustic sensor is ambient-noise prone. Especially when it continues to collect data in a noisy ambient daytime setting, the signal quality

of the system will hinder. Another study uses more advanced algorithms that involve signal processing to derive scratch behavior from a consumer smartwatch (Samsung Galaxy Gear Live). However, this system still struggles to differentiate scratching from involuntary arm movements, and, like the actigraphy, it remains locked in a rigid, bulky wrist-based form factor.

Such a form factor affects the acceleration measurement due to its high mass density. They are incapable of capturing necessary physiological measures given the loose coupling to the skin. While advanced signal processing can provide some improvement, scratching behavior is highly variable amongst individuals suggesting the need for a raw signal with a higher signal-to-noise ratio (SNR) for further signal processing.

The MA sensor can capture both low-frequency signals and high-frequency signals due to its high time and sensing resolution. Intimate skin coupling enables the capture of mechanoacoustic signals with high SNR. Also, the sensing modality, by nature, makes the sensor insensitive to the ambient noise. For instance, our sensor can measure the mechanical movement and the raw acoustic signal produced by scratching, even in the noisy surrounding. These unique features differentiate the MA sensor from all other prior reported scratch sensors. Thus, we hypothesize that the collective utility of capturing both an acoustic and mechanical movement will enable more sensitive and specific measurement of scratching.

Furthermore, this multi-modal sensing will better quantify both scratching time and scratching intensity. MA sensor can also operate continuously throughout sleep. Therefore, it would hold additional value for patients suffering from atopic dermatitis.

We mount the MA sensor between the 2nd and the 3rd metacarpophalangeal joints specifically to capture movement that reflects finger scratching (extension and flexion of the 1st and 2nd digit), wrist scratching (extension, flexion, ulnar lateral movement, and radial lateral movement), and elbow scratching (extension, flexion, medial, and lateral movement) (Fig. 35). In Fig. 36, we show the ability to capture the mechanical and acoustic signals obtained from

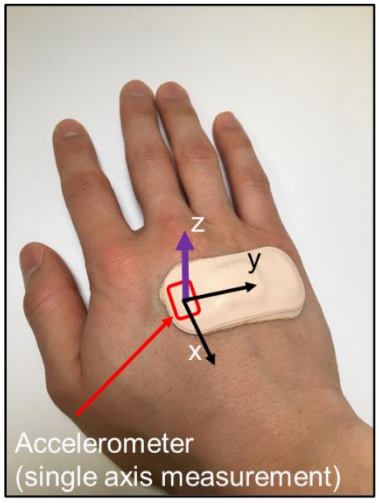

Fig. 35 | The mounting location of the MA sensor. The z-axis acceleration is in the normal direction to the dorsal side of the hand. The x-axiz is in the proxial direction. The accelerometer part of the sensor is specifically placed between the 2nd and the 3rd metacarpophalangeal joints.

scratching.

The amplitudes of x, y, and z accelerations can be correlated to scratching intensity. The high-frequency acoustic signatures of the movement can differentiate a true scratching motion from other voluntary movements as the acoustic range of the scratching signal is highly distinctive from the low-frequency hand waving signal. The preliminary results here on a healthy normal subject demonstrate our ability to distinguish scratching signals from various scratching behaviors of varying intensities and arm movements (e.g., fingers only, wrist movement, elbow movement) (Fig. 36).

Based on these preliminary results, and understanding the opportunity space in quantifying scratch, MA sensor shows excellent potential in adding its value from the application.

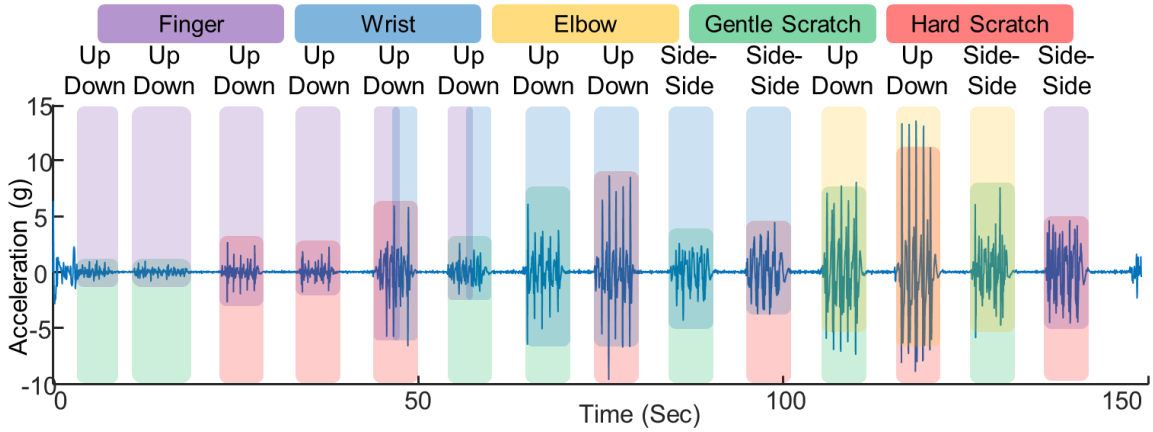

Fig. 36 | MA signal of various types of scratching motion. Depending on the intensity and the body parts used for scratching, the captured signal displays a noticeable difference in amplitude and frequency. MA scratch signal with relatively smaller amplitudes relates to gentle scratch. MA scratch signal with relatively larger amplitudes relates to hard scratch. Using just finger, the amplitude is smallest relative to all the other scratching motion with other body parts. Using entier forearm to scratch (elbow), MA signal

With a broader sensing range of the accelerometer, the sensor would have more significant potential in its use for detecting a wide range of scratching motion. Further analysis of the frequency signatures and development of the machine learning algorithm would amplify its robustness and practicality in differentiating various types of scratching action.

IV. Monitoring COVID-19 related symptoms with mechanoacoustic sensor

Given the challenges faced during the recent COVID-19 pandemic, the development of the MA sensor that permits remote monitoring of physiological signals in a patient's naturalistic environment is more critical than ever. Upon further testing, the MA sensor offers an alternative for monitoring physiological signals in a clinical setting or a patient's home.

On March 11, the World Health Organization (WHO) declared SARS-CoV-2 (COVID-19) a pandemic. COVID-19 is a severe acute respiratory syndrome that is highly contagious. Its most common symptoms are fever and cough[65]. In fact, recent COVID-19 HCP screening guidance includes respiratory symptoms (cough, shortness of breath, or sore throat) and fever[66]. Although

the severity may vary, the symptoms gradually appear, and therefore, personalized assessment is possible. Using a mechanoacoustic sensor, we first acquire the personalized baseline of the symptoms or the body's initial state and observe their changes over time.

Of the symptoms in the guideline, there are well established and standardized methods of monitoring the body temperature to identify fever, but not for the cough and other respiratory behavior. Thus, there have been many efforts in quantifying coughs using the microphones, accelerometers, pneumographic belts, and spirometer. For example, the microphone of the earphone, or even the cellphone's microphone collects the audio of coughing sound[67,68]. In general, the audio signal is subject to other ambient acoustic noise, and the position of the microphone is inconsistent from the source of the sound. As result, this system will require costly computation and have unreliable diagnosis of the symptoms. Another study used a spirometer to measure the condition of a respiratory system, such as lung capacity and respiration speed. However, the measurement can only do voluntarily by having the user actively blowing air into the sensing unit. Such an operation protocol is not suitable for continuous measurement. Continuous measurement is especially important in this study since the recovery rate differs vastly throughout a different population. Such irregular measurements may miss essential time points of the disease progression. Another study demonstrates a patch form of the accelerometer sensor to detect the cough, but its rigid form factor will induce poor mechanical coupling with the skin and introduce motion artifacts. Its stiff mechanics of the device and its direct contact with the skin will create a mechanical mismatch at the device-skin interface, resulting in a large mechanical load on the skin and inducing skin irritation.

With the wireless flexible MA sensor mounted on the suprasternal notch, we can continuously measure the coughing signal with consistent distance from the source of the signal without inducing skin irritation. In addition, with its large measurement capacity, we can measure the heart

rate, respiration rate, and other physiological information, as demonstrated above, along with the coughing signal. Therefore, the sensor provides a comprehensive understanding of the effect of the virus. In addition to the MA signal, it also utilizes the temperature sensor embedded in the accelerometer unit and simultaneously measures the subject's body temperature. With these sensing capabilities, the system collects an abundance of information that includes all the signals related to the symptoms listed in the guideline.

Unlike other clinical studies, COVID patients must operate the MA sensor without direct assistance from the clinicians. Therefore, the updated system presented here emphasizes the simplification and automation of the operation steps and data pipeline (Fig. 37). We eliminated the user-end effort and reduced the user error by making the system fully automated. The device operates without toggling any buttons. The user, as a default, charges the sensor on the wireless charging platform. When the user places the device on their suprasternal notch, it continuously records the data to its onboard memory for 36 hours. When the data collection is complete, and the device charges again, the user-interface automatically downloads the data from the device via Bluetooth. Therefore, the system only requires the user to mount the device on and off from the charging platform and the suprasternal notch.

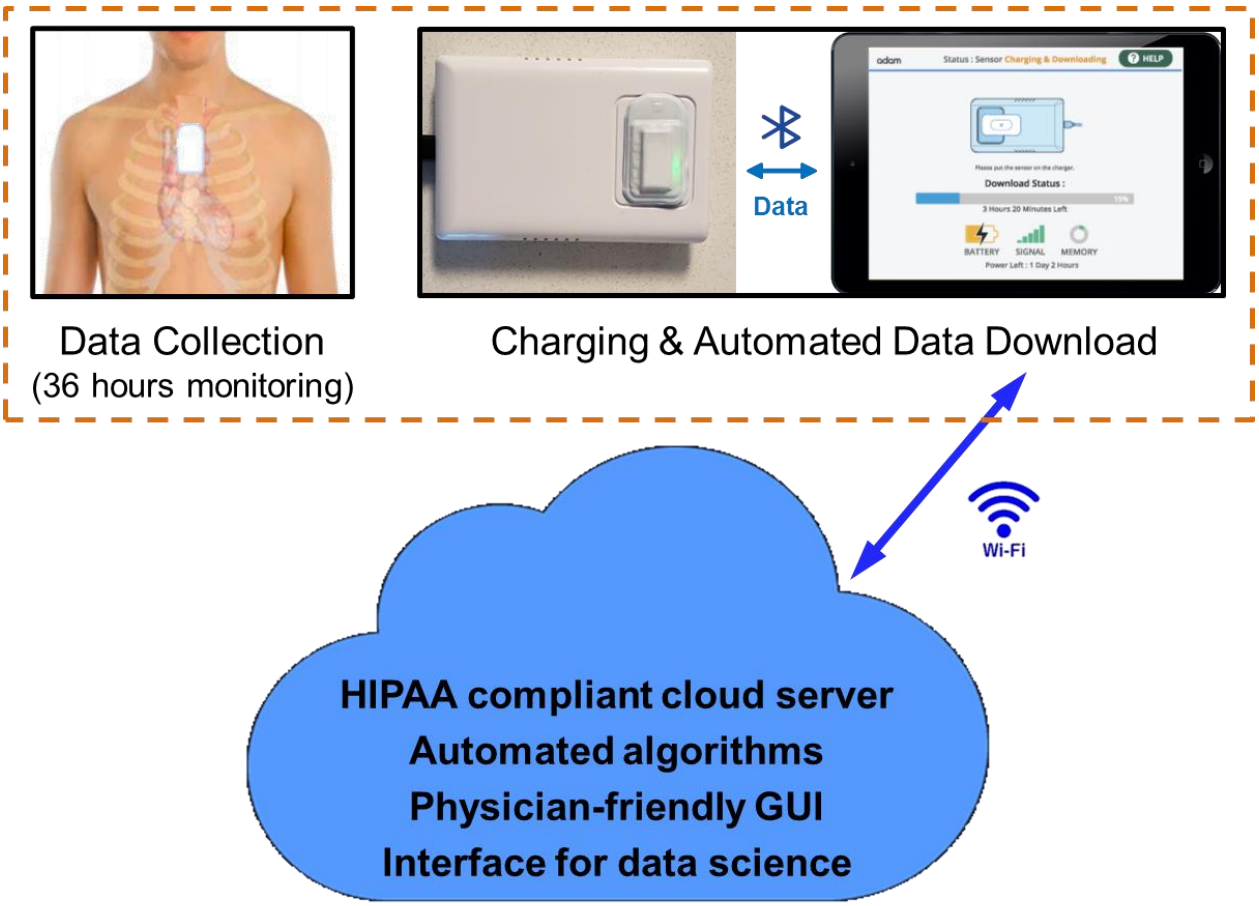

Fig. 37 | Simplified system operation flow and data pipeline. The end-user only needs to mount the device on the skin or set it on the charging platform. The sensor will record the MA signal to its internal memory. The saved data will stream to the user interface when the device is charging. The user interface then will upload the data directly to the HIPAA compliant cloud where the data automatically get processed.

Once the user-interface finishes the downloading process, it uploads the data to the HIPAA compliant server (AWS S3 bucket) via Wi-Fi. Once the data uploading process completes, AWS Lambda function channels the data to the data-processing pipeline that is in an AWS EC2 incident. Fig. 38 demonstrates the process of the cough-count algorithm. The algorithm first transforms the Z-axis time-series signal into a spectrogram (0.1 seconds 90 % overlapping moving window). It identifies the vocalization signal by finding the notable characteristics of harmonics of the spectrogram, specifically the fundamental frequency and second harmonics. The vocalization signal and cough signal share many similarities in the time domain, including

large-amplitude and wideband. Therefore, the algorithm separates the vocalization signal from the coughing signal by zeroing its associated time-series signal. Finally, the high pass filter isolates only the cough signal, and the peak-detection algorithm picks out the individual coughing signal.

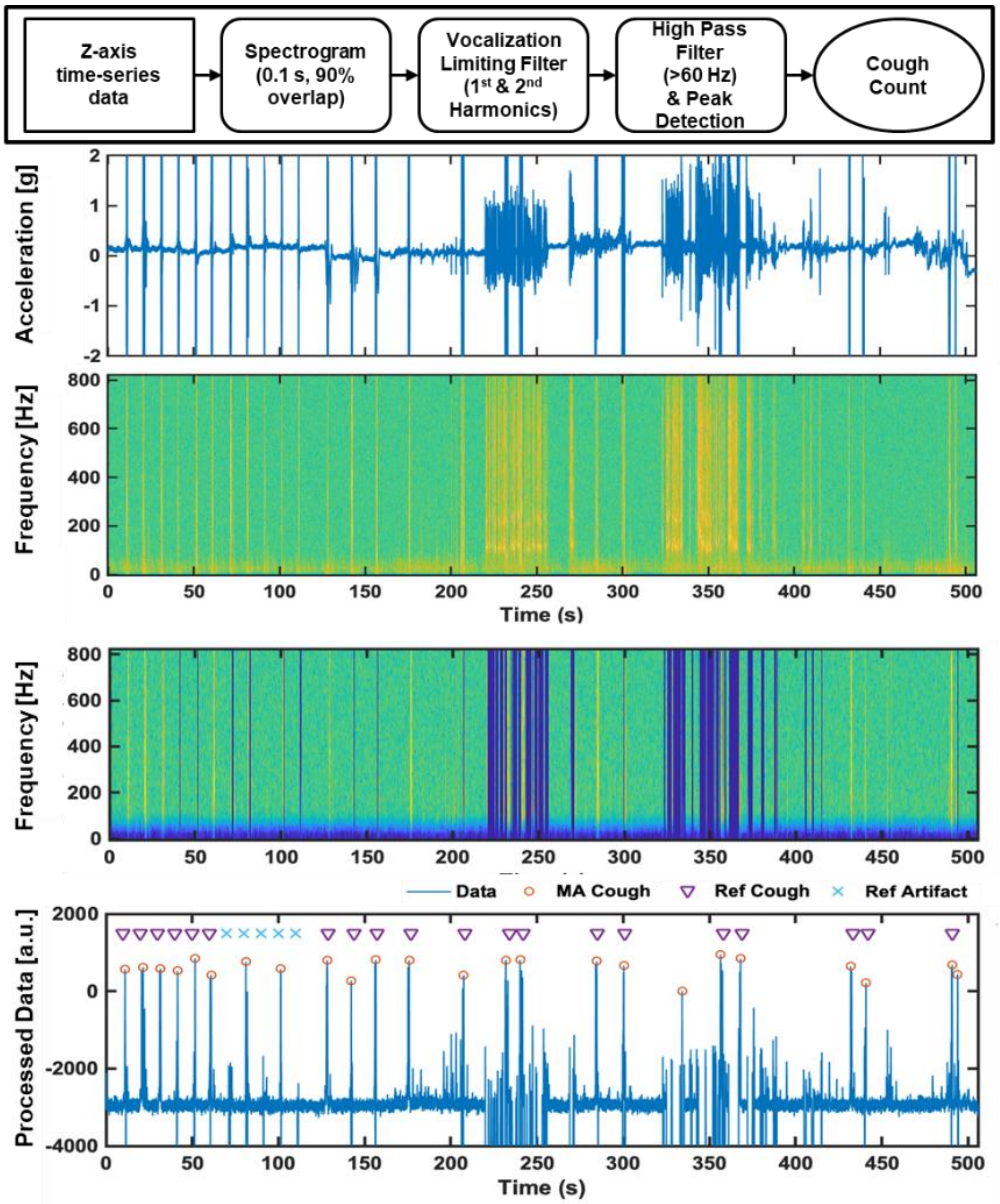

Fig. 38 | The cough-count algorithm steps in order (from top to bottom). It uses the Z-axis acceleration signal to determine the characterize the cough signal. It first transforms the signal into a spectrogram and then blocks out the time window that shows pronounced characteristics of harmonics related to the vocalization. Finally, a high pass filter and peak detection algorithm determine the cough signal.

The pipeline outputs cough counts, body temperature, and other signals demonstrated above in the form of both graphical charts and spreadsheets. Our internally developed HIPAA compliant web-app creates a dashboard with these graphical charts and remotely provides the trend of the

patients' physical state to the clinicians, enabling the clinicians to monitor the patient in real-time without direct contact. Also, from the processed data, we can build further algorithms to comprehend the data and classify to the different level of the COVID-19.

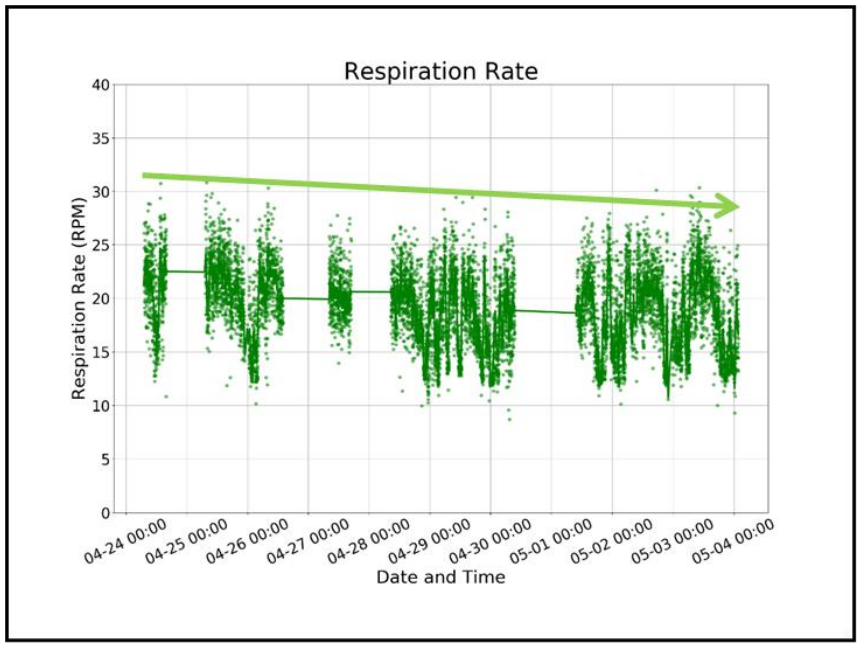

Fig. 39 | Respiration rate measurement of a COVID patient from a MA sensor on the suprasternal notch. The measurement started from when the subject was an active COVID and continues after the subject is discharged. The trend illustrates the decrease in breathing rate as the patient recovers from COVID.

Figs. 39 -42 show processed data from a COVID patient. The patient wore the senor starting from the beginning of COVID infection and continued to wear it post-discharge to monitor the disease progression and recoveries for two weeks. Fig. 39 provides the trend of the respiration rate. The data suggest that the patient breathing pattern becomes slower throughout recovery. Another interesting observation we can make from Fig. 40 is the decrease in the intermittent tachycardia, where the heart rate is higher than 100 bpm[69]. The catecholaminergic, including emotions, physical activity, and stresses, often trigger tachycardia events. Over the two weeks of the recovery period, the number of tachycardia has decreased. Another observation is the

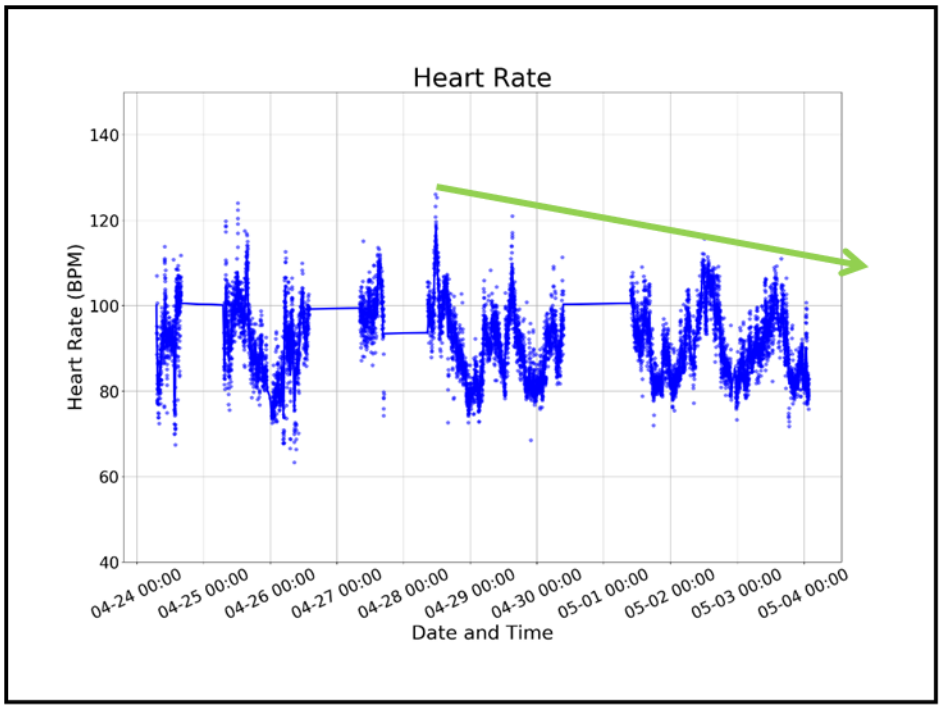

Fig. 40 | Heart rate measurement of a COVID patient from a MA sensor on the suprasternal notch. The measurement started from when the subject was an active COVID and continues after the subject is discharged. The trend illustrates the decrease in the number of tachycardia as the patient recovers from COVID.

activity counts, as shown in Fig. 41. The patient becomes more active as the recovery progresses. These observations are useful features to classify the different stages of the disease and the severity of the COVID-19 symptoms.

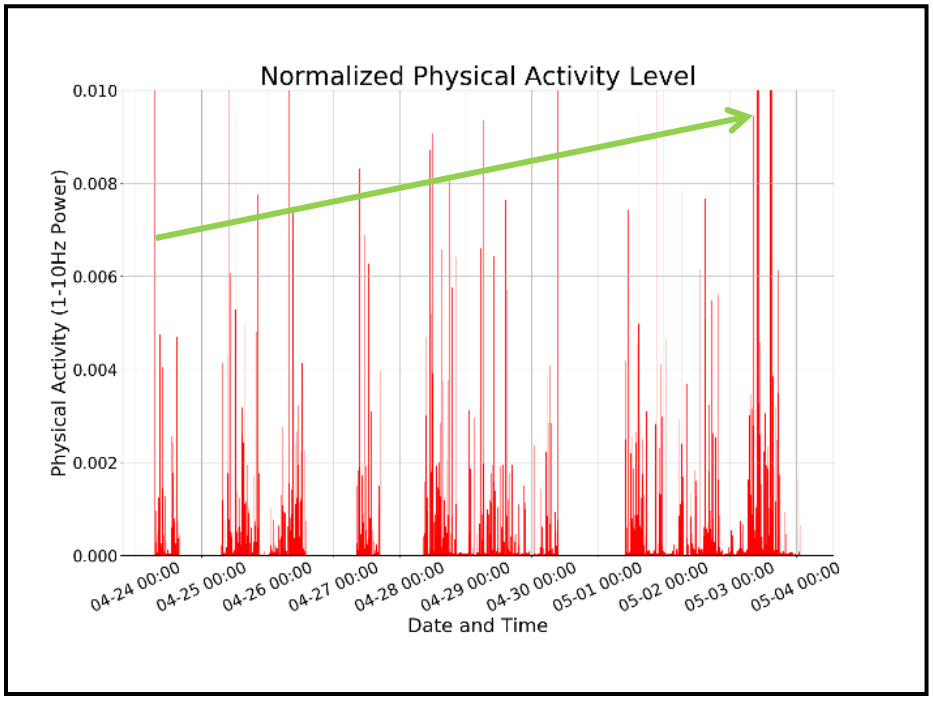

Fig. 41 | Activity measurement of a COVID patient from a MA sensor on the suprasternal notch. The measurement started from when the subject was an active COVID and continues after the subject is discharged. The trend illustrates the increase in the number of body movements as the patient recovers from COVID.

Fig. 42 provides a statistical overview of the cough frequency over three days. It includes the cough counts per 10 seconds time window, cumulative cough counts, the trends of heart rate, temperature, and activity intensity, all derived from the mechanoacoustic signal. It is also

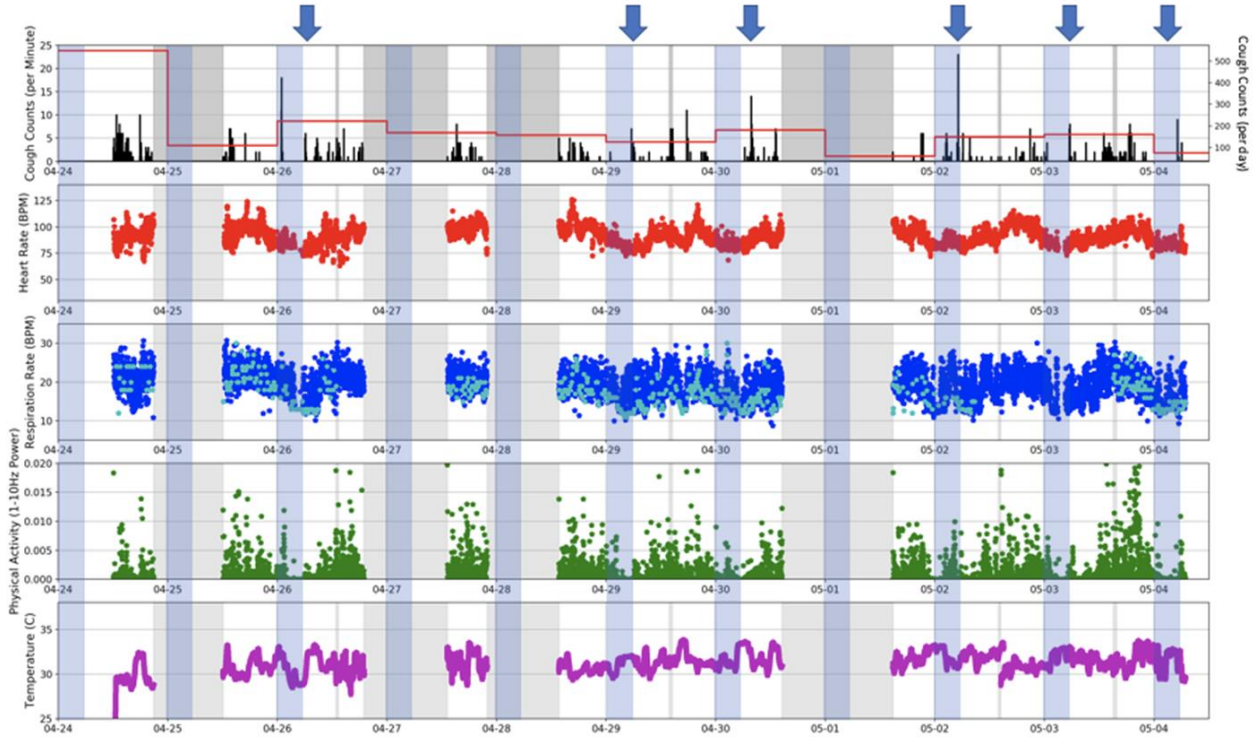

Fig. 42 | A statistical overview of COVID-19 related symptoms and the trend throughout 3-days. Cough counts represent the total number of coughs in the 10-second time window. Mechanoacoustic signal also provides information about heart rate and physical activity. Heart rates display the circadian rhythm of the patient. The sensor measures temperature using the thermocouple embedded in the accelerometer unit.

interesting to see the heart rate trend following the circadian rhythm. The heart rate decreases overnight and increases throughout the day.

This application highlights the strength of the MA sensor in every facet. The sensor remotely monitors continuous physiological states of COVID patients in a natural setting without any direct physical interaction with the patient.

V. Multinodal Mechano-Acoustic Sensor

These MA sensors can also communicate with each other and operate in a time-synchronous manner. The time alignment across the sensors allows additional observability of our physiological system. The MA signals measured simultaneously from the SN and other parts of the body enable the mapping of cardiac activities, calculation of pulse arrival time, cancelation of the noise and artifacts, and amplification of the signal of our interest.

It is essential to consider the distance between the two measurement sites of the body relative to the sampling rate or the time resolution of our measurement capability. Currently, the sampling rate is at 3200Hz, and the speed for sound in body tissue is 1540 m/s. Therefore, the two sensors must be apart at least 0.96m. In the case of characterizing the travel of a mechanical signal throughout the body, a source of the signal and its relative path governs the minimum characterizable distance.

In this study, we focus on characterizing the pulse traveling through the blood vessel by measuring the pulse arrival time-difference (PAT) between two remote locations. PAT is a crucial parameter for calculating the blood pressure without using a pressurized cuff[70]. The first MA sensor measures the pulse near the aorta, second MA sensor near the subclavian artery, and third MA sensor on the SN. Other than the SN, the two locations are the conventional measurement sites for the stethoscope. This multinodal system records time-synchronized MA data across the body and measures the PAT among the three areas.

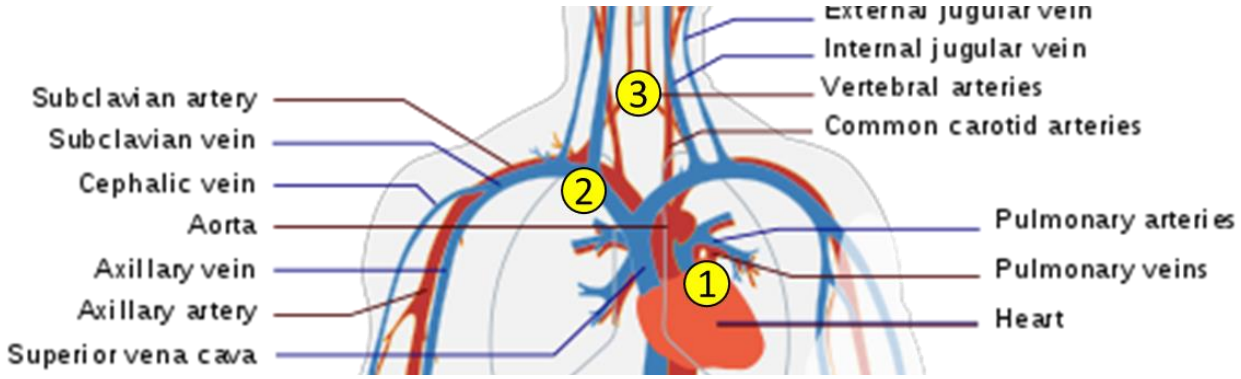

Fig. 43 | Three different measurement sites for deriving PAT. Three remotely time-synchronized MA sensors measure the pulsatile mechanical signal at three different locations: ① MA sensor near the aorta, ② MA sensor near the subclavian artery ③ MA sensor near the SN.

The algorithm calculates the time difference from two locations by cross-correlating two MA signals with 1.5 second time windows with 50% overlap. Each window provides the time lag value where the cross-correlation is at maximum. Aggregating the time lags from each window, we find the PAT between two statistically sound locations.

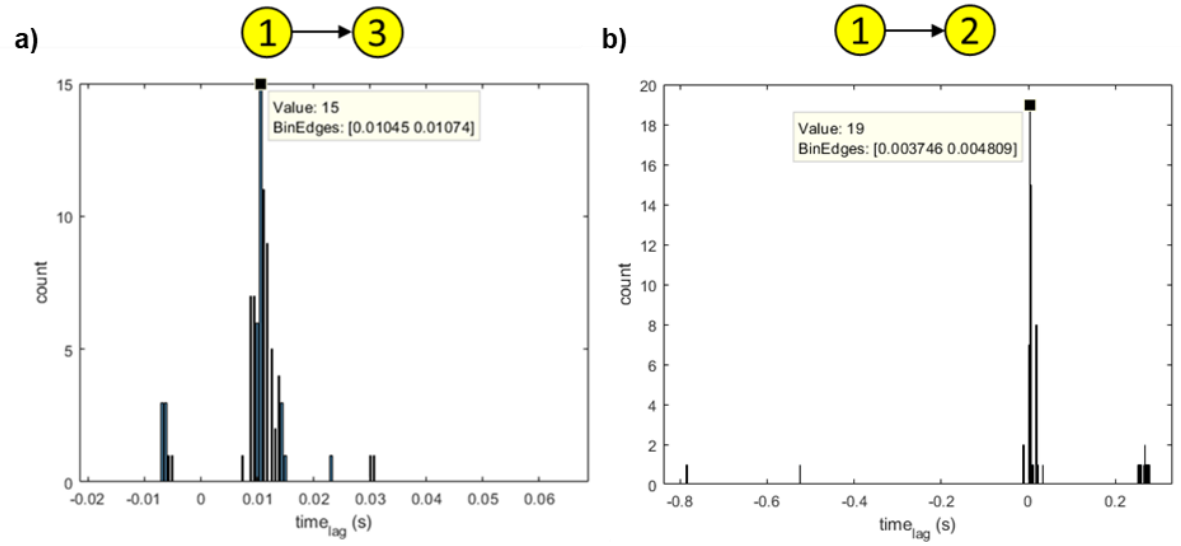

Fig. 44 | Histograms of the pulse arrival time differences between two measurement sites. The individual $time_{lag}$ values are representative time differences associated with the maximum cross-correlation value of 1.5 second time windows with 50% overlap. **a)** This histogram shows an aggregate PAT between SN and aorta. 0.01 second time difference is the most frequently observed value. **b)** This histogram shows an aggregate PAT between the subclavian artery and aorta. 0.0037 second time difference is the most frequently observed value.

In Fig.44, we may infer that PAT is 0.01 seconds between SN and the aorta and 0.0037 seconds between the subclavian artery and aorta. These PAT values correspond to their relative physical distance.

From this experiment, we learned that it is promising to derive the PAT using multiple sensors. However, a more thorough examination and comparison with the gold-standard data is necessary. Also, the time lag caused by the Bluetooth communication across the multiple sensors may result in inaccurate measurement; therefore, a more significant number of samples is required for higher confidence in the PAT derivation. An alternative solution is to have multiple MA sensor in a single system and eliminate the wireless communication latency, which the following section is going to demonstrate.

VI. Dual Accelerometer

Mechano-acoustic (MA) signal includes small vibrations to large motions at the surface of the skin generated by the internal organs (10^{-3} ms^{-2}) and body movements (>10 ms^{-2})[71]. Conventional MEMS accelerometers are capable of measuring MA signal, mostly in the low-frequency range due to its inertial mass density and loose mechanical coupling at the body-device interface[72,73]. Consequently, many studies employ other complementary sensors with different sensing modalities in addition to the accelerometer to monitor both low-frequency body movements and additional higher frequency physiological information[74–76].

These modules either contain all the sensors in a single rigid plastic circuit board (PCB) or a separate rigid PCBs that communicate via wires running down the body. The modules with the multiple sensors in a rigid body measure on the location ideal for the complementary sensors. For example, the PPG-accelerometer sensing unit uses a wrist or forehead as the mounting location to measure the pulse and the body motion[74,76]. Wrist and head, however, can move

independently from the core body, and the acceleration measurement does not strictly represent the movements that are clinically significant[77]. The modules with multiple sensors in a separate rigid PCBs have wires that create the mechanical and electrical link between two sensors in different locations. These wires may constrain the natural body motion and introduce a source of non-physiological artifacts to both sensors, especially when the subject is moving.

Of these modules, only standard physiological information that the sensors share is the low-frequency signal induced by the body motion. The studies use the signal from an accelerometer to reference the movement and reject the motion artifacts in the complementary sensors data. These artifact rejection algorithms, however, require careful consideration of the different metrics. In addition, the module with separate body and mounting location has the motion artifacts in the complementary sensor data weakly correlated with the movement signal from the accelerometer, making it difficult to distinguish the artifacts and the signal.

A small, lightweight, flexible wireless MA sensor on the suprasternal notch (SN) collects a rich set of physiological information simultaneously and continuously. The sensor on the SN can capture the superposed signal that contains information of cardiac activity from the carotid artery, respiration cycle from the chest wall movement, swallowing behavior from the laryngeal movement, and esophagus, vocalization from the vocal fold vibration, and core body movement from the sternum. It has broad implications, especially in tracking the progression of diseases or recoveries, due to its ability to continuously monitor a rich set of physiological information without the constraints of its location. With the sensor, we can find the correlation among the different physiology and draw a wholesome picture of the physical response to various inputs and diseases. This single accelerometer sensor, however, has a limitation when it records under an extensive motion. The large energy of body motion often overwhelms the subtle MA signals. Each step involves both low-frequency MA signal and impulse signal. Therefore, it is hard to confidently

obtain other physiological data besides the body movements, even with the high order bandpass filter. This limitation dwindles its capability of measuring multiple physiological information simultaneously and continuously in natural settings.

Therefore, the system incorporates a feature that collects data using multiple sensors in a time-synchronized manner. An additional MA sensor on the sternum mainly collects the core-body motion with other subtle physiological information that has even smaller amplitudes relative to the data from the sensor on SN. Although the theoretical time resolution of the synchronization is in sub-millisecond, as the sensors synchronize via Bluetooth communication, the radio transmission efficiency directly affects its time resolution. A robust algorithm that cancels noise or enhances the signal requires a characterizable time difference between the data.

The developments presented here augments the prior art with (1) an additional high sensitive accelerometer integrated in a single flexible PCB (fPCB) that enhances the stability of time synchronization between two acceleration measurements, (2) the neck serving as the general mounting location for the sensor that has flexible and stretchable PCB platform which minimizes the mechanical coupling between two accelerometers, (3) algorithms that fully exploits the benefit of dual accelerometer including active motion artifact rejection, and signal amplification.

Engineering mechanics fo the device

The system implements a thin and soft form factors of the fPCB and device architecture from our previous work[71] (Figs. 45a and b). The system minimizes its footprint by taking advantage of fPCB's flexible mechanics (Fig. 45c). The fPCB layout has three main islands dedicated to an inductive antenna for the wireless charging, power management and charging circuits, and microcontroller unit (nRF52840, Nordic Semiconductor) with its necessary peripheral components, including the 4Gb memory. The fPCB design has multiple bending zones designed to withhold

the static bending deformation when they fold on top of each other. The island with the microcontroller unit has two accelerometers on either side of the rigid electronic platform (Fig. 45b). Two pairs of serpentine structures electronically connect both accelerometers from the rigid platform, and mechanically decouples those accelerometers from the rigid mechanics of the component island. Accelerometers can undergo 90° torsional, 45% tensile and 180° bending deformations, without affecting the integrity of the solder joints between the components and the fPCB board (Figs. 45d and e). These serpentine structures also enhance the accelerometers' sensitivity and their SNR, especially when the monitoring signal involves high impulsive motion, such as movement with stomping action.

Furthermore, up to twelve of this system can operate in a time synchronized manner. This feature maximizes the system's measurement capabilities. The system can measure the MA signals throughout the body and collect signals from multiple people simultaneously with the sensor-network, connected to a single user interface. Like the COVID-19 study, the system also minimizes the number of operation steps to improve its usability. It only requires the user to stick it on the suprasternal notch when it is in use and mount it on the wireless charging platform when it is not in use. The sensor records data from both accelerometers to the device's internal memory, and when it is charging, the sensor streams the data to a user interface device via Bluetooth. Once the user interface has the data, it uploads them to the HIPAA compliant cloud and computes various physiological information, including the cough counts, respiration rate, heart rate, activity level, and body temperature using the algorithm from our previous studies[71]. As a result, the total number of the required devices is less, while the amount of the data we collect is more.

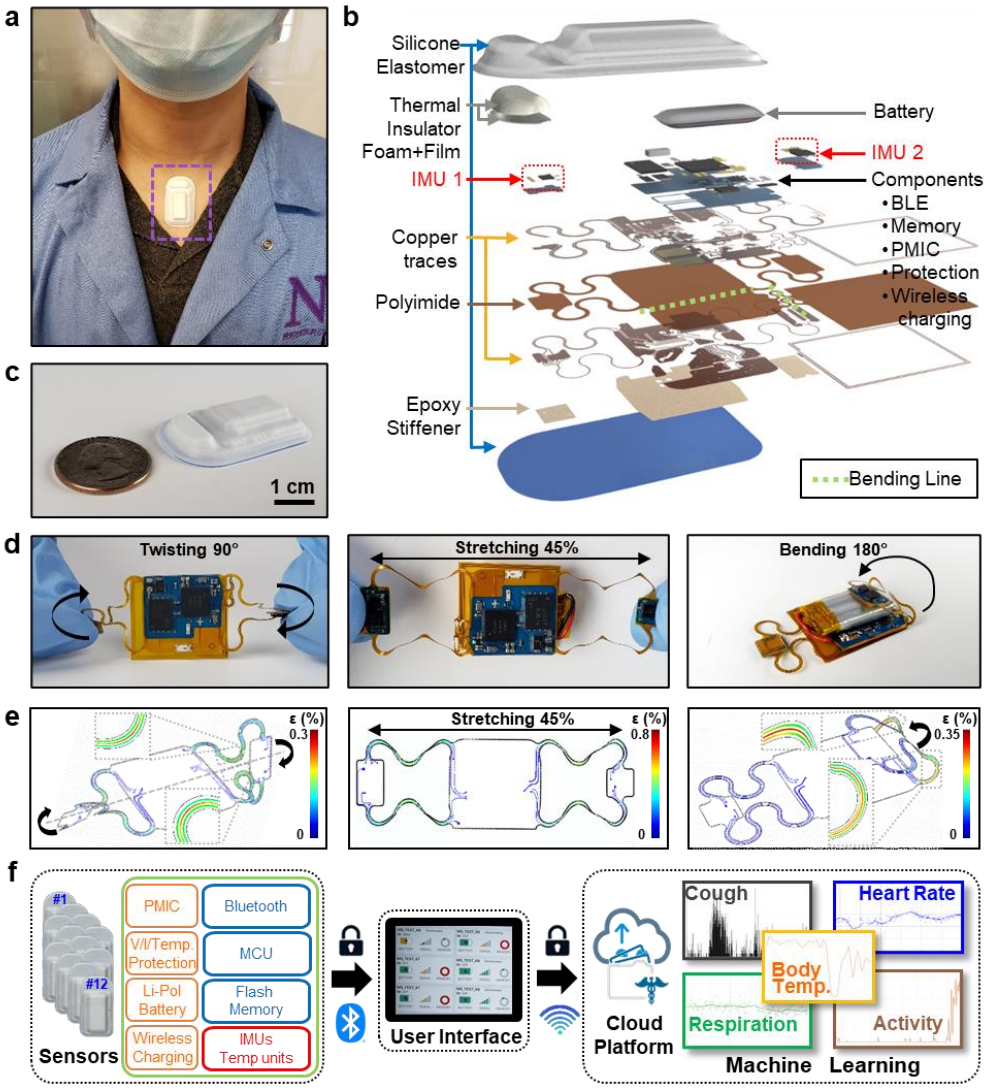

Fig. 45 | Images, schematic illustrations, functional flow charts and mechanical modeling results for a wireless, skin-interfaced mechano-acoustic (MA) measurement technology designed for mounting on the suprasternal notch (SN). **a**, Images of the MA device interfacing the SN. **b**, Exploded schematic illustration of the active components, interconnect schemes and enclosure architectures. **c**, size comparison to a Washington quarter (24.26 mm diameter). **d**, Images of a device in twisted (left), stretched (middle) and folded (right) configurations**. e**, Finite element modeling of the mechanics during uniaxial tensile and twisting deformations. **f**, Block diagram of the system operation.

Algorithms and the signal

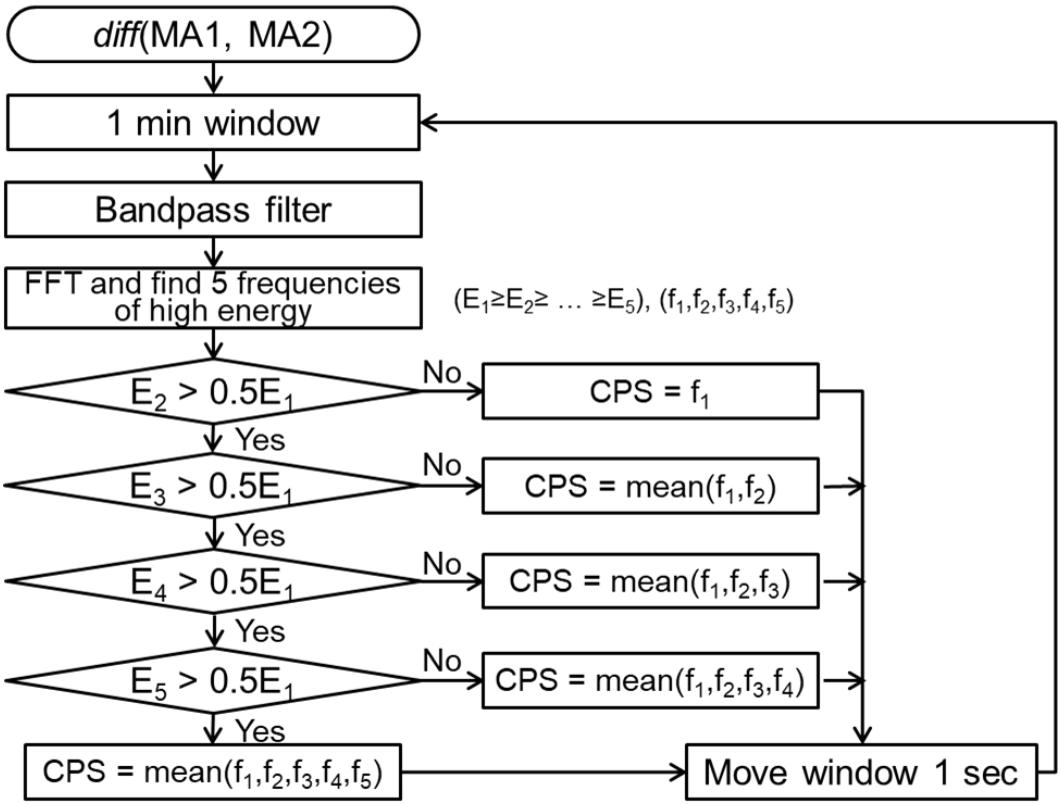

Fig. 46 | Block diagram of the post-processing algorithm for calculating the rates of quasiperiodic signals with a motion artifact rejection. An appropriate bandpass filter (0.1-1 Hz for the respiration signal, 10-60 Hz for the cardiac signal) filters 1-minute window of a differential signal of two MA data. The algorithm finds the five predominant frequencies and ranks them based on their energy. Then, the algorithm only considers the frequency that has its energy higher than half of the maximum energy. The output rate of the signal or the count-per-second (CPS) is the mean of the significant frequencies. The same procedure is applied to the 1-minute window with 59-seconds window overlap.

The algorithm takes advantage of the dual accelerometer with precise time synchronization. The difference of the data from both accelerometers already minimizes the large amplitude signal related to the motion artifacts. This naturally increases the effectivity of digital filters that draw out the signals of interest without any leakage of the motion artifacts. This single algorithm, therefore, successfully derives subtle MA signals, such as heart rate and respiration rate while the subject is in motion. The algorithm starts with a 1-minute window of the differential data. It goes through the bandpass filter (0.1-1 Hz for the respiration signal, 10-60 Hz for the

cardiac signal). Fast-Fourier-Transformation (FFT) identifies five most predominant frequencies of the filtered differential signal. Then, the algorithm selects the subset of the dominant frequencies with energy higher than 50% of the maximum energy. Finally, it calculates the periodicity of a specific signal by averaging the selected dominating frequencies.

Fig. 47a demonstrates the effectiveness of the differential signal from the dual accelerometer sensor. Simply by subtracting the two signals, the differential signal minimizes the large amplitudes induced by the ambulatory motion. This reduces the efforts for rejecting the motion artifacts to detect the physiological information of the interest. From the differential MA signal, the algorithm calculates the respiration rate estimate and heart rate estimate. Figs. 47b and c highlight the performance of the dual accelerometer system and its differential signal, especially when the subject is in ambulatory motions. When the subject is sitting still on a chair, the algorithm correctly calculates the respiration rate and the heart rate measurement using either the single accelerometer signal, or the differential signal. However, when the subject starts to move, the algorithm shows the significant differences in the accuracy of calculating heart rate and respiration rate. Using the single accelerometer data, the algorithm guesses the physiological information very poorly ($R^2 = 0.5$). On the contrary, using the differential data correctly measures the physiological information even when the subject is walking, running, or jumping ($R^2 = 0.9$).

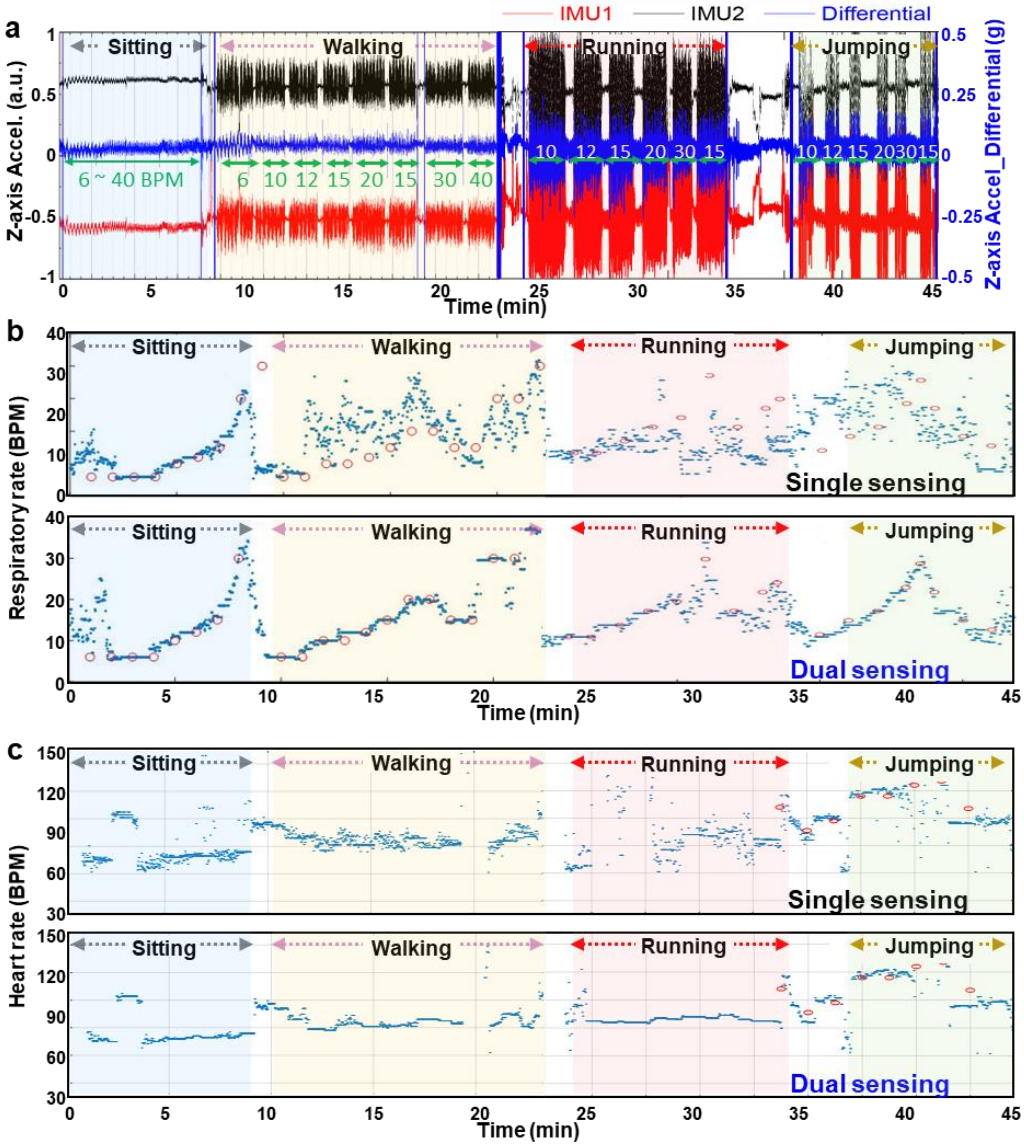

Fig. 47 | 45 minutes of sample data from a dual accelerometer sensor in various ambulatory motions and measurements of respiratory rate and heart rate compared with those of single accelerometer sensor and gound truth value. a. The subject sits quietly for 8 minutes, walked for 15 minutes with resting intervals, ran for 10 minutes with resting intervals, and jumped for 7 minutes with resting intervals. **b.** Single raw accelerometer data provides the respiratory rate reliably while the subject sits still. When the subject is in the ambulatory motions, just a single accelerometer data have a hard time calculating the respiratory rate close to the ground truth. The differential signal of the two accelerometer data provides an accurate respiration rate that matches well with the ground truth signal. **c.** Single raw accelerometer data provides the heart rate reliably while the subject sits still. When the subject is in the ambulatory motions, just a single accelerometer data have a hard time calculating the heart rate close to the ground truth. The differential signal of the two accelerometer data provides an accurate heart rate that matches well with the ground truth signal.

Its further application for stroke rehabilitation and sports are in progress in clinics. In

stroke rehabilitation, the sensor measures the severity of the motor dysfunctionality of the stroke survivors, especially the difference of the motor function relative to the hemiplegia. Also, in parallel, the sensor is capable of capturing respiration rate and heart rate and other behaviors such as swallowing and vocalization, which are also essential biomarkers to track the recovery of the post-stroke patients. In sports, it has always been challenging to measure the respiration rate and constant heart rate when the athletes are in a wide range of fast and dynamic motion. With the dual sensor, even when there are large motion and acceleration, the system can reliably capture the important physiological information to track the athletes' condition concerning their performance for the first time. With the extra sensor, the system provides the solution to the limitation that the single accelerometer MA sensor had. As a result, it enables the system to continuously monitor vital signals and other subtle MA signatures that were hard to capture when the subject is moving.

4. Application of the Hardware Architecture in Other Sensors

The flexible device architecture considers its use cases for other sensors with different modalities. With the air encapsulation platform, the architecture isolates sensing units from the environmental factors such as mechanical undulation, and heat, which is beneficial for the temperature sensor and MA sensor. The architecture also has a flexible thin membrane that is mechanically separated from the core electronics. Therefore, the flexible bottom layer can integrate sensing interfaces such as electrodes for ECG and EEG. In this chapter, I demonstrate the use case of the soft device architecture in ECG and Pulse Oximetry measurements.

I. NICU Vital Monitor

In the United States, over 480,000 critically-ill infants and children enter intensive care units each year. Those with less than one year of age suffer from the highest mortality rates and therefore require the most intensive care[78,79]. These fragile patients include premature infants who may weigh as little as 500 g (1.1 lbs), 1/7 that of an average term baby[80]. Continuous monitoring of vital signs is essential, yet existing technologies require the use of multiple sensors interfaced to the skin with adhesive tapes and connected by wires to electronic processing systems that are often tethered to the wall. This system of hardware creates a multitude of difficulties in both routine and specialized procedures in clinical care, ranging from therapeutic skin-to-skin contact with parents (i.e. kangaroo mother care, KMC) to feeding, diaper changing and bathing[80]. Furthermore, continuous monitoring of certain vital signs, such as blood pressure, demands additional wired hardware, such as peripheral arterial, central venous, or pulmonary arterial catheters[81], which can induce other types of complications, including thrombus formation and occlusion, infection (e.g. sepsis), rupture, pseudoaneurysm, and death. A wireless system capable of non-invasive, continuous vital sign monitoring would greatly enhance the effectiveness and safety of neonatal and pediatric critical care[82].

The results reported in the following adopt mechanically robust, manufacturable systems that rely on Bluetooth technology to circumvent these limitations, with options in operation and power supply that address a broad spectrum of clinical and user preferences, ranging from modular primary batteries to integrated secondary batteries to wireless harvesting schemes. These platforms additionally support important modalities in monitoring that lie beyond both the standard of care and the capabilities of our previously reported systems. These include the ability to: (1) capture acoustic signatures of cardiac activity, reflecting valvular function, (2) quantify pulse wave dynamics through multiple measurements, as a reliable surrogate for systolic blood pressure.

Device and System Design.

Fig. 48a presents an exploded view illustration of one of the two mechanically soft, wireless devices that form the complete system. This example uses a modular battery unit for power supply in a design that allows for gentle mounting on the curved skin of the chest (chest unit) via a thin hydrogel coupling layer to record electrocardiograms (ECGs), mechano-acoustic signals of vocalization and cardiac/respiratory activity, body orientation and movements, and skin temperature, all enabled by a Bluetooth Low Energy (BLE) system-on-a-chip (SoC) and associated collection of sensors. The overall layout includes a thin, flexible printed circuit board (flex PCB) and mounted components, configured in an open design with serpentine interconnect traces. The construction involves folding of distinct, but connected, platforms as a key step in assembly and packaging (Fig. 48a and Fig. 49). Quantitative insights from three-dimensional finite element analysis (FEA) of the system-level mechanics help to define an optimal distribution of the active components to reduce the lateral dimensions of the device by ~250%. A pre-compression process in the assembly forms buckled layouts in the serpentines for enhanced mechanical properties, with improved flexibility and stretchability. A soft elastomeric enclosure with an inner

silicone gel liner (~300 μm thick, ~4 kPa) further improves the mechanics to ensure compatibility with the fragile skin and highly curved anatomical features of neonates at the lowest gestational ages. A pair of thin, conductive elements formed using a doped silicone material (carbon black in polydimethylsiloxane, abbreviated as ‘CB PDMS’; bulk resistivity of 4.2 Ω.cm) serve as soft electrical connections to corresponding gold electrodes on the flexible printed circuit board and to conductive hydrogel skin interfaces for ECG measurements. The result is a soft and completely sealed, waterproof system with applicability across a wide range of settings, focused on but not limited to the NICU and PICU (Fig. 49).

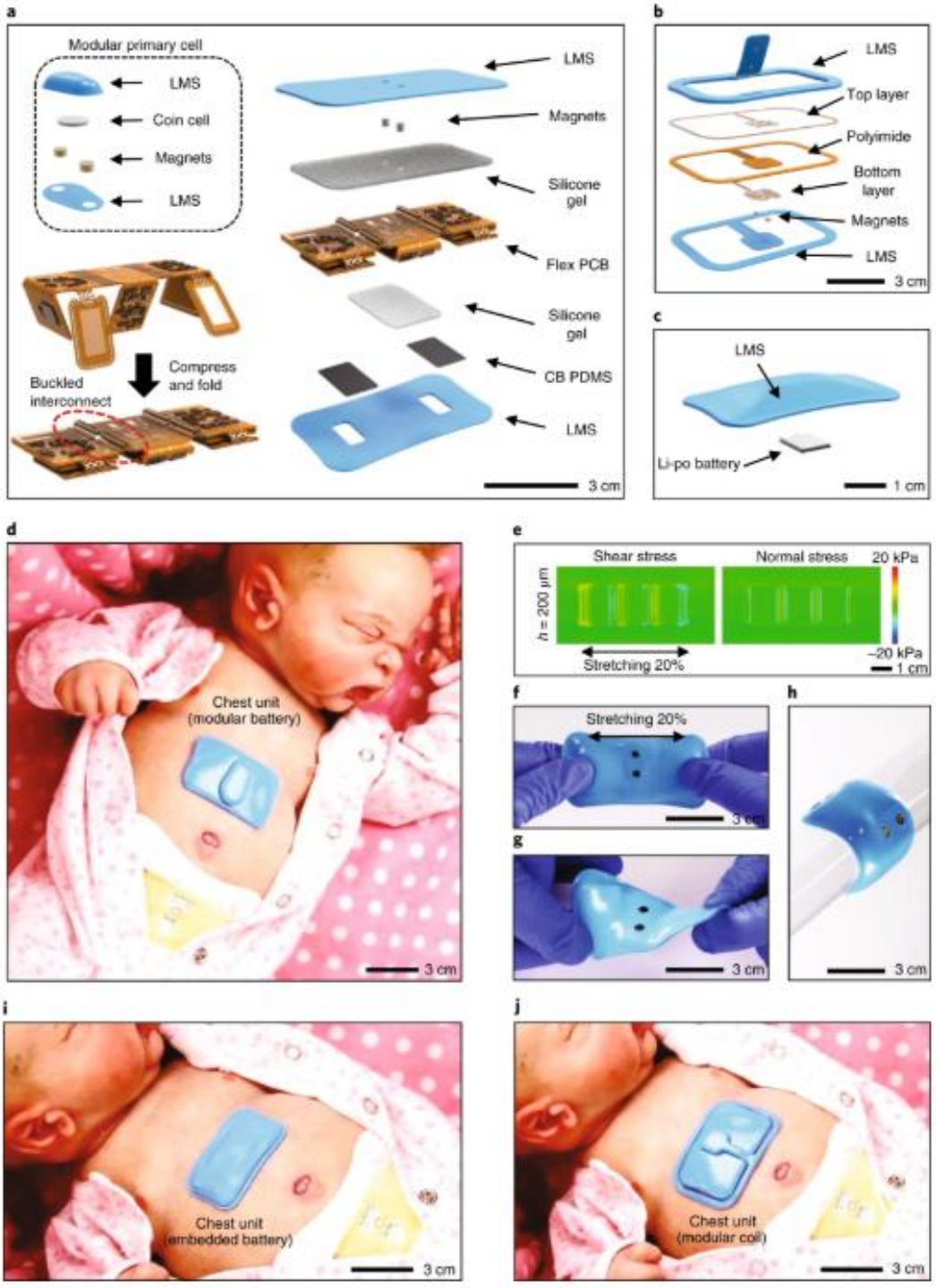

Fig. 48 | Designs, mechanical characterization results and pictures of a soft, wireless chest unit for physiological monitoring of neonatal and pediatric patients. a, Schematic diagram and exploded view illustration of a device with a modular primary battery. The main body consists of buckled serpentine interconnects between islands of electrical components contained within a soft, elastomeric enclosure. The battery interfaces to the system via reversible magnetic coupling. Thin silicone pads establish electrical connections between measurement electrodes and a hydrogel interface to the skin, to yield a completely sealed, waterproof device. LMS stands for low modulus silicon.

Fig. 48 | b, Illustration of a detachable wireless power harvesting system. **c,** Illustration of a powering option that involves an integrated, wirelessly rechargeable battery. This option uses a different top layer encapsulation, without the magnets. **d,** Photograph of the chest unit with modular battery on a realistic model of a neonate.**e,** Computed stresses (right: normal; left: shear) at the interface between the skin and a device during uniaxial stretching to a strain of 20%, with a thickness of 200 μm. **f-h,** Photograph of a representative device during stretching (**f**), twisting (**g**), and bending (**h**). **i,j,** Photographs of a device with integrated battery (**i**) and with a wireless energy harvester (**j**), both mounted on a model.

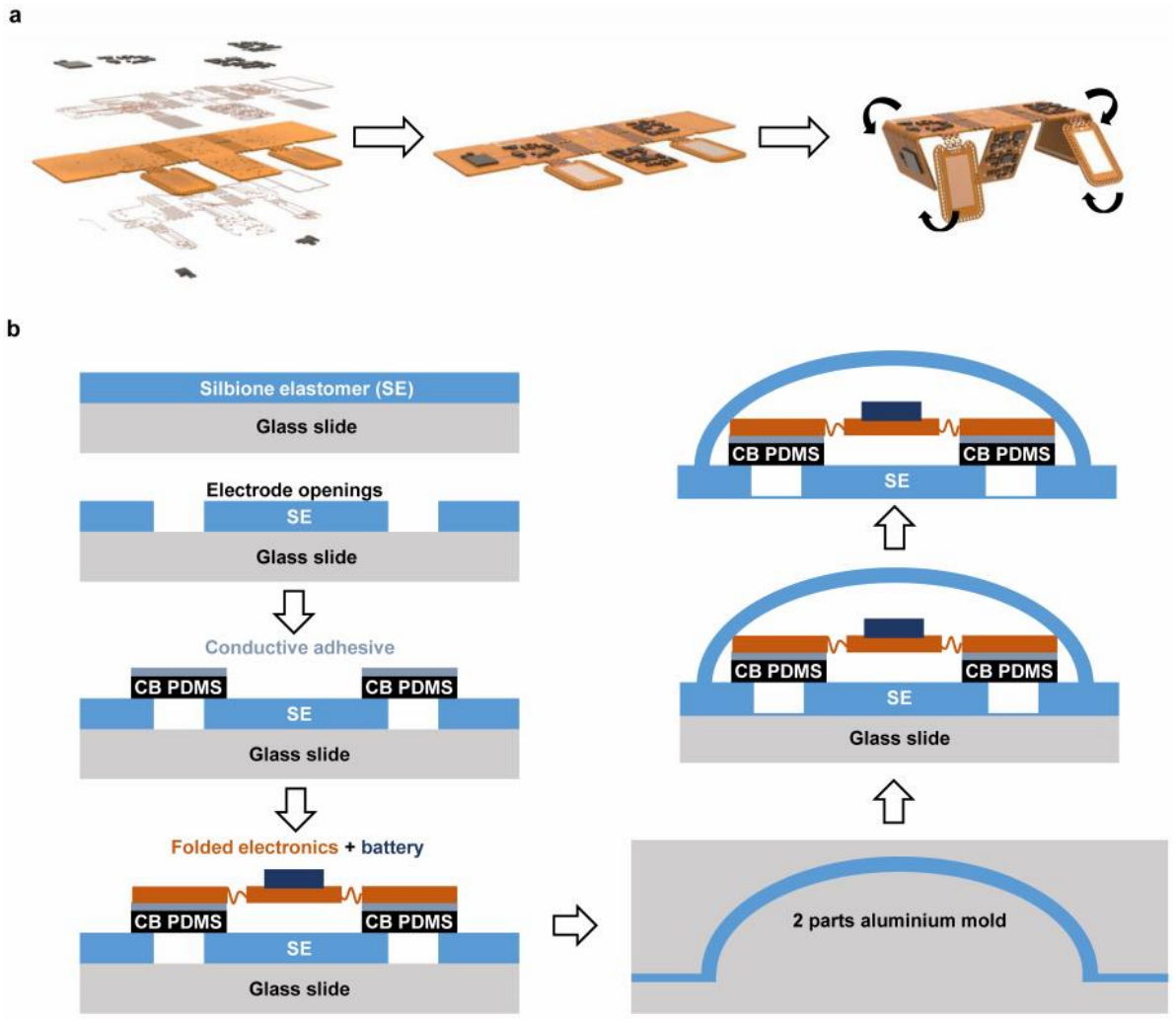

Fig. 49 | a, Leftmost and middle diagrams show the assembly process of the circuit components on a 2-layer flexible printed circuit board. Rightmost diagram shows how the sub-systems of the chest board are folded. **b,** The encapsulation process involves spin casting Silbione elastomer on top of a glass slide, followed by opening for the electrodes. CB PDMS is used to fill the electrode openings, then combined with the folded board that contains a battery. The top Silbione enclosure is prepared through a 2-part molding process and closes the encapsulation of the chest unit. Removing the glass slide finalizes this process. CB PDMS, carbon black in polydimethylsiloxane.

The modular battery unit couples to the device mechanically and electrically through pairs of matching sets of embedded magnets (Fig. 48a, inset), thereby: (1) allowing replacement of the

battery without removing the device from the patient to minimize disruptions in clinical care, decrease the burden on the care giver, and reduce risks of skin injury[83]; (2) enabling removal of the battery to allow autoclave sterilization of device; and (3) mechanically decoupling the battery from the device to improve the bendability and, therefore, the compliance at the skin interface. The magnetic scheme also allows for other options for power supply, not only in choices of battery sizes, shapes and storage capacities (and therefore operational lifetimes; Fig. 50), but also in alternative modalities, including battery-free schemes that rely on wireless power transfer (Fig. 48b). As an example of this latter possibility, a magnetically coupled harvesting unit can be configured to receive power from a transmission antenna placed under the bed and designed to operate at a radio frequency of 13.56 MHz with a negligible absorption in biological tissue[84]. Fig. 48c illustrates a third option, in which a wirelessly rechargeable battery (Li-polymer, 45 mAh) lies within the sealed enclosure of the device to eliminate any external connections.

Fig. 50 | Similarly, negligible change in temperature was observed, when a limb unit was mounted on the foot of the same subject for 24 hours in full operation (n = 3). Different form factors of encapsulated modular batteries. The green colored circle with the diameter of choking limit outlines the safety limits to prevent choking hazard for kids under 3 years old.

The photograph in Fig. 48d features a chest unit deployed on a model of a neonate, with a small, encapsulated button cell as a modular battery. The serpentine interconnects encapsulated with polyimide (PI), the folded configuration, and the soft enclosure with gel liner lead to a uniaxial elastic stretchability that exceeds ~33% at the device level, corresponding to a ~500% stretchability in the interconnects prior to encapsulation in the outer silicone shell (Fig. 51b). The gel (~300 μm thick, ~4 kPa modulus) provides strain isolation between the folded

islands to reduce the stresses at the skin interface to levels below the thresholds for sensory perception (20 kPa) for uniaxial stretching of up to 20%, a value at the high end of the range expected in practical use (Fig. 48e and Fig. 51c). The resulting elastic bending radius and equivalent bending stiffness are ~20 mm and ~9.6 Nmm^2, respectively (Fig. 51b). These mechanical characteristics ensure soft, irritation-free skin interfaces, even in cases of extreme curvatures encountered with small babies and/or low Gas, as well as those that have conditions such as pneumothorax. The images in Fig. 48f-h illustrate a device stretched, twisted, and bent to levels that exceed requirements. Mounted units with the embedded battery and battery-free designs appear in Fig. 1i and j, respectively.

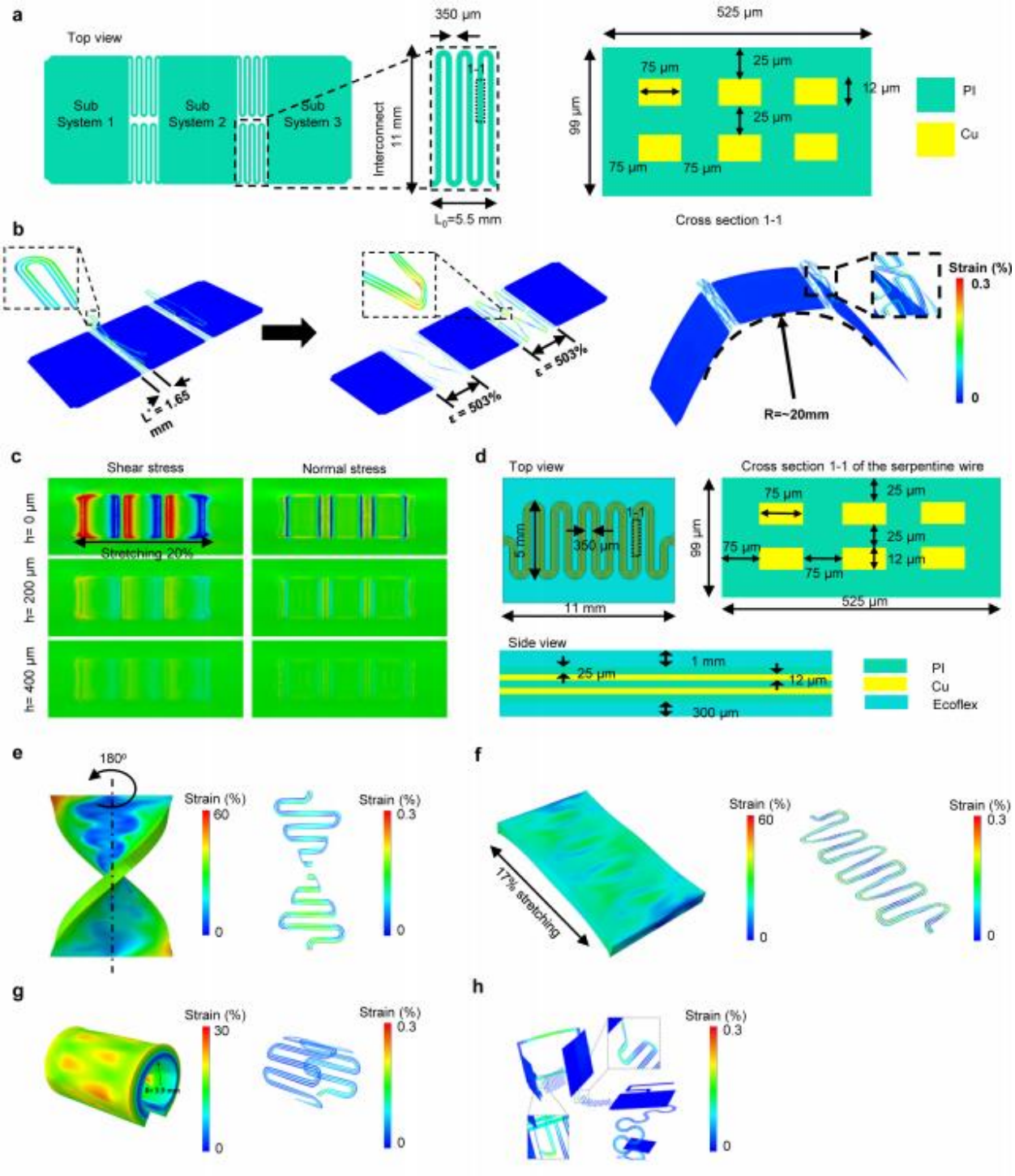
a
Top view
Sub System 1
Sub System 2
Sub System 3
Interconnect 11 mm
350 μm
1-1
L_0=5.5 mm
525 μm
99 μm
75 μm
25 μm
12 μm
25 μm
75 μm
75 μm
PI
Cu
Cross section 1-1
b
L = 1.65 mm
ε = 503%
ε = 503%
Strain (%)
0.3
0
R=~20mm
c
Shear stress
Normal stress
h= 0 μm
h= 200 μm
h= 400 μm
Stretching 20%
d
Top view
5 mm
350 μm
1-1
11 mm
Cross section 1-1 of the serpentine wire
99 μm
75 μm
25 μm
25 μm
12 μm
75 μm
525 μm
Side view
1 mm
25 μm
12 μm
300 μm
PI
Cu
Ecoflex
e
180°
Strain (%)
60
0
Strain (%)
0.3
0
f
17% stretching
Strain (%)
60
0
Strain (%)
0.3
0
g
Strain (%)
30
0
Strain (%)
0.3
0
h
Strain (%)
0.3
0

Fig. 51 | a, Schematic illustration of stack and dimension information for serpentine interconnects and sub-systems of a chest unit. PI, polyimide. Cu, copper. **b,** Computational result showing the stretchability and bendability of a chest unit's board. L_0, nominal length of a serpentine interconnect of the board. L*, pre-compressed length of the serpentine. $\varepsilon = (L-L^*)/ L^*$ defines the elastic stretchability. **c,** Computational result showing the effect of thickness of the strain isolation layer regarding shear and normal stress when a chest board is assumed to be stretched by 20%. **d,** Schematic illustration of the stack and dimension information for serpentine interconnects of a limb unit. **e,** Strain distribution in the encapsulation layer (left) and copper layer (right) of an interconnect during (**e**) twisting, (**f**) stretching, (**g**) and bending at the radius of 3.9 mm. **h,** Overall bending mechanics of a limb unit board illustrated by strain distribution.

Fig. 52a summarizes the structure of the other component of the complete system, a device designed to record reflection-mode photoplethysmograms (PPGs) and skin temperature from peripheral locations. This limb unit features a layout that facilitates wrapping around the foot, palm or toe. Fig. 52b highlights the overall design, with umbilical interconnects that can bend to radii as small as ~3.9 mm twist through angles as large as 180° and elastically stretch to uniaxial strains as high as 17% (Figs. 51e and f). The fundamental design features are similar to those of the chest unit, but in configurations that anatomically match different limb interfaces: ankle-to-sole of the foot for neonates in NICU (Fig. 52c) and wrist-to-hand (Fig. 52d) and foot-to-toe (Fig. 52e) for patients in the PICU. The image in Fig. 52f shows both chest and limb units deployed on a model of a neonate in a NICU isolette, along with a representative illustration of vital signs information displayed on a tablet computer.

Fig. 52g presents a block diagram that summarizes the overall operational scheme. The chest unit includes a wide-bandwidth 3-axial accelerometer (BMI160, Bosch Sensortec), a clinical-grade temperature sensor (MAX30205, Maxim Integrated), and an ECG system that consists of two gold-plated electrodes. The limb unit includes an integrated pulse oximetry module (MAX30101, Maxim Integrated) for measuring dual wavelength PPGs and a temperature sensor (MAX30205, Maxim Integrated). The power management circuit for battery operation uses a voltage regulator to provide supply voltages required for the various components (3.3V or 1.8V).

The modular battery-free platform (Fig. 48b) includes an inductive coil tuned to 13.56 MHz, a full-wave rectifier, and a two-stage cascaded voltage regulating unit.


a
LMS
IC Components
Li-po battery
Flex PCB
Oximeter
LMS
3 cm
b
2 cm
c
2 cm
d
2 cm
e
2 cm
f
156
100
116
35.3 33.6
Chest unit
Limb unit
2 cm
g
Chest unit
+ Electrode
– Electrode
Filter and amp
14-bit ADC
3-Axial accelerometer
SPI
Clinical-grade thermometer
I2C
BLE SoC
Time sync
Limb unit
BLE SoC
I2C
Photodiode
LED (R, IR)
I2C
Clinical-grade thermometer
Power-supply scheme
Embedded battery
Modular battery
Wireless power transfer

Fig. 52 | Designs and pictures of limb units for physiological monitoring of neonatal and pediatric patients and block diagram of the full system operation. a, Schematic diagram and exploded view illustration of the limb unit, designed to measure PPG, SpO_2 and temperature. **b,** Photograph of a device while bent and twisted. **c-e,** Deployment of a device on (c) a model of a neonate at the ankle-to-base of the foot, (d) a model of a pediatric patient (2-year-old chronical age) at the wrist-to-hand, and (e) at the foot-to-toe. **f,** Photograph of the chest and limb unit a model of a neonate in a NICU isolette, with a tablet computer displaying representative data through a graphical user interface. **g,** Block diagram showing the operational scheme of two time-synchronized device, with an analog-front-end for ECG processing, 3-axis accelerometer, thermometer IC, and BLE SoC for the chest unit and a pulse oximeter IC, thermometer IC, and BLE SoC for the limb unit. Three different options for power supply appear at the bottom of the frame.

5. Discussion

This paper provides a comprehensive overview of the hardware design for the soft, wireless biosensor. The device utilizes the soft and resilient elastomeric encapsulation-membrane as the multi-functional component. Because of the wireless charging circuits and wireless communication, the encapsulation-membrane does not require any openings and functions as a barrier for the internal electronics with the complete seal preventing the electronics from the foreign substances and making it sterilizable. It also functions as a substrate for the electronics and creates a soft interface between the skin and the sensor. With its soft mechanics in addition to the strain isolation layer, it mitigates the mechanical mismatch between the skin and the electronic components and enhances its long-term wearability.

The electronic layout incorporates flexible and stretchable interconnects to contain the rigid mechanics of the conventional electronic components to small isolated areas. Any soft wireless biosystem can adapt this device architecture and stretchable circuit layouts with a minor change in the substrate design that suits the specific sensing modality as demonstrated here with MA and NICU sensors. The components and the manufacturing steps align with the current manufacturing practices and commercial components and enable the mass-production of the advanced technology.

The soft mechanics, and power efficient electronics with a rechargeable battery enable the system to continuously monitor for 24 hours without causing skin irritation and power shortage. The user-interface that interacts with the device has minimal operation steps and provides intuitive and effortless procedures for the end-user. In combination, the system offers an easy access to the biological information that were originally cumbersome to obtain, or even unobservable. As result, appropriate algorithm is necessary to process both unconventional and conventional physiological information that the device simultaneously captures. They include HR, TT, RR, SC,

EE, with additional possibilities in tracking body orientation, steps and gait, coughing events, respiratory sounds, and many others.

The signal processing algorithms for the specific biomarkers play an integral part of the whole system. The algorithms look for a unique feature of the time series data for each event in both time and frequency domain. Also, they look at the causal relationship and the periodicity to assist the classification of events. For now, these classifications are discrete and therefore with its hard threshold, it is hard to classify the same type of events with weaker or stronger intensity than its average. In the future, taking the probabilistic approach may alleviate this problem of generalization.

This paper primarily focuses on the soft, wireless MA sensor design and data analytics. The sensor operates on the SN that offers a set of signals related to multiple physiological processes. It demonstrates its capacity through the applications in sleep monitoring, stroke rehabilitation, scratch study, and COVID-19 study. These applications especially take full advantage of the systems' unique characteristics, such as continuous monitoring and simultaneous sensing of multiple biomarkers along a single measurement unit. The MA sensor has significant advantages compared to both conventional stationary monitoring system (e.g., polysomnography system, or vital sign monitor) and wrist mounted wearables. It demonstrates its capability of measuring majority, if not all, of the signals that the conventional systems can measure in unconstrained natural setting outside of the hospital. An additional sensing modality that the system can take advantage of is the optical sensor monitoring the blood oxygenation.

The paper also portrays its limitation in sensing subtle biomarkers while moving. This has critical effects in the sensor's advantages of multiple signal sensing and continuous monitoring in the real-life environment. However, the multi-nodal measurement and dual accelerometer illustrate their potential to improve the functionality and to expand the types of addressable

applications. In both approaches, the additional accelerometer is on the part of body where it is more prone to capture the signal associated with the core body movement and less to other MA signals. The additional sensor enhances the observability of the system and infer better about the subtle physiological activities even when there is dramatic the body movement.

This paper has exhaustively exploited the use of accelerometer in sensing numerous biomarkers. For the future study, like the multiple accelerometer approaches, adding strain gauge as a complementary component to the MA sensor would allow the system to accurately capture the subtle movements related to the chest wall expansion, which would not be effected by the motion artifact by its nature of sensing mechanism. By having the system interact with an active component such as a haptic interface, or electrical stimulator, we can also translate the current system to an active system and broaden its application from diagnostic tool to therapeutic apparatus. These active interfaces would create a closed-loop control system with the human body in the part of the control system. We also need to address and keep the confidentiality of recording in mind as we rely on the wireless communication protocols.

We made the sensor functioning as a modular unit that can collect information of our interest. With the soft wireless sensor, we are finally at the point of making the continuous monitoring to a reality. As demonstrated in this paper, continuous monitoring provides information relating to the progression of disease and recovery in detail with higher time resolution than any precedent technology. I believe that we are just starting the new phase of the neo-healthcare era hope to see that the technology improving quality of our lives.

6. References

1. Tortora, G. J. & Derrickson, B. H. *Principles of anatomy and physiology*. (Wiley, 2016).
2. Liu, Y. *et al.* Epidermal mechano-acoustic sensing electronics for cardiovascular diagnostics and human-machine interfaces. *Sci. Adv.* **2**, (2016).
3. Kaniusas, E. *Sensing by Acoustic Biosignals*. *Biomedical Signals and Sensors II : Linking Acoustic and Optic Biosignals and Biomedical Sensors* (Springer Berlin Heidelberg, 2015). doi:10.1007/978-3-662-45106-9_4
4. Hu, Y., Kim, E. G., Cao, G., Liu, S. & Xu, Y. Physiological Acoustic Sensing Based on Accelerometers: A Survey for Mobile Healthcare. *Ann. Biomed. Eng.* **42**, 2264–2277 (2014).
5. Vavrinský, E. *et al.* Application of acceleration sensors in physiological experiments. *J. Electr. Eng.* **65**, 304–308 (2014).
6. Makarenkova, A., Poreva, A. & Slozko, M. Efficiency evaluation of electroacoustic sensors for auscultation devices of human body life-activity sounds. in *2017 IEEE 1st Ukraine Conference on Electrical and Computer Engineering, UKRCON 2017 - Proceedings* 310–313 (IEEE, 2017). doi:10.1109/UKRCON.2017.8100499
7. Makaryus, A. N., Swarup, S. & Makaryus, A. Digital stethoscope: technology update. *Med. devices Evid. Res.* **11**, 29–36 (2018).
8. Dudik, J. M., Coyle, J. L. & Sejdic, E. Dysphagia Screening: Contributions of Cervical Auscultation Signals and Modern Signal-Processing Techniques. *IEEE Trans. Human-Machine Syst.* **45**, 465–477 (2015).
9. Kok, M., Hol, J. D. & Schön, T. B. Using inertial sensors for position and orientation estimation. *Found. Trends Signal Process.* **11**, 1–153 (2017).
10. Brond, J. C. & Arvidsson, D. Sampling frequency affects the processing of Actigraph raw acceleration data to activity counts. *J. Appl. Physiol.* **120**, 362–369 (2016).
11. Di Rienzo, M. *et al.* A wearable system for the seismocardiogram assessment in daily life conditions. in *Proceedings of the Annual International Conference of the IEEE Engineering in Medicine and Biology Society, EMBS* **2011**, 4263–4266 (2011).
12. Jafari Tadi, M. *et al.* Gyrocardiography: A new non-invasive monitoring method for the assessment of cardiac mechanics and the estimation of hemodynamic variables. *Sci. Rep.* **7**, 1–11 (2017).
13. Inan, O. T. *et al.* Novel Wearable Seismocardiography and Machine Learning Algorithms Can Assess Clinical Status of Heart Failure Patients. *Circ. Heart Fail.* **11**, e004313 (2018).
14. Shandhi, M. M. H. *et al.* Performance Analysis of Gyroscope and Accelerometer Sensors for Seismocardiography-Based Wearable Pre-Ejection Period Estimation. *IEEE J. Biomed. Heal. Informatics* 1–1 (2019). doi:10.1109/jbhi.2019.2895775
15. Hernandez, J., McDuff, D., Quigley, K. S., Maes, P. & Picard, R. W. Wearable Motion-based Heart-rate at Rest: A Workplace Evaluation. *IEEE Journal of Biomedical and Health Informatics* (2018). doi:10.1109/JBHI.2018.2877484

16. Hung, P. D., Bonnet, S., Guillemaud, R., Castelli, E. & Yen, P. T. N. Estimation of respiratory waveform using an accelerometer. in *2008 5th IEEE International Symposium on Biomedical Imaging: From Nano to Macro, Proceedings, ISBI* 1493–1496 (2008). doi:10.1109/ISBI.2008.4541291

17. Bates, A., Ling, M. J., Mann, J. & Arvind, D. K. Respiratory rate and flow waveform estimation from tri-axial accelerometer data. in *2010 International Conference on Body Sensor Networks, BSN 2010* 144–150 (2010). doi:10.1109/BSN.2010.50

18. Liu, G. Z., Guo, Y. W., Zhu, Q. S., Huang, B. Y. & Wang, L. Estimation of respiration rate from three-dimensional acceleration data based on body sensor network. *Telemed. J. E. Health.* **17**, 705–711 (2011).

19. Lapi, S. *et al.* Respiratory rate assessments using a dual-accelerometer device. *Respir. Physiol. Neurobiol.* **191**, 60–66 (2014).

20. Tadi, M. J. *et al.* A miniaturized MEMS motion processing system for nuclear medicine imaging applications. in *Computing in Cardiology* **43**, 133–136 (2016).

21. Preejith, S. P., Jeelani, A., Maniyar, P., Joseph, J. & Sivaprakasam, M. Accelerometer based system for continuous respiratory rate monitoring. in *2017 IEEE International Symposium on Medical Measurements and Applications (MeMeA)* 171–176 (2017). doi:10.1109/MeMeA.2017.7985870

22. Pompilio, P. P., Sgura, A., Pedotti, A. & Dellaca, R. A MEMS accelerometers based system for the measurement of lung sound delays. in *2010 5th Cairo International Biomedical Engineering Conference, CIBEC 2010* 138–141 (2010). doi:10.1109/CIBEC.2010.5716042

23. Lee, J., Steele, C. M. & Chau, T. Time and time-frequency characterization of dual-axis swallowing accelerometry signals. *Physiol. Meas.* **29**, 1105–1120 (2008).

24. Damouras, S., Sejdić, E., Steele, C. M. & Chau, T. An online swallow detection algorithm based on the quadratic variation of dual-axis accelerometry. *IEEE Trans. Signal Process.* **58**, 3352–3359 (2010).

25. Dudik, J. M., Jestrović, I., Luan, B., Coyle, J. L. & Sejdić, E. A comparative analysis of swallowing accelerometry and sounds during saliva swallows. *Biomed. Eng. Online* **14**, 3 (2015).

26. Kumari, S. K. & Mathana, J. M. Blood Sugar Level Indication Through Chewing and Swallowing from Acoustic MEMS Sensor and Deep Learning Algorithm for Diabetic Management. *J. Med. Syst.* **43**, 1 (2018).

27. Mehta, D. D., Zañartu, M., Feng, S. W., Cheyne, H. A. I. & Hillman, R. E. Mobile voice health monitoring using a wearable accelerometer sensor and a smartphone platform. *IEEE Trans. Biomed. Eng.* **59**, 3090–3096 (2012).

28. Michalevsky, Y., Boneh, D. & Nakibly, G. Gyrophone: Recognizing Speech from Gyroscope Signals. in *23rd USENIX Security Symposium (USENIX Security 14)* 1053–1067 (USENIX Association, 2014).

29. Nyan, M. N., Tay, F. E. H., Manimaran, M. & Seah, K. H. W. Garment-based detection of falls and activities of daily living using 3-axis MEMS accelerometer. *J. Phys. Conf. Ser.* **34**, 1059–1067 (2006).

30. Curone, D., Bertolotti, G. M., Cristiani, A., Secco, E. L. & Magenes, G. A real-time and self-calibrating algorithm based on triaxial accelerometer signals for the detection of human posture and activity. *IEEE Trans. Inf. Technol. Biomed.* **14**, 1098–1105 (2010).

31. Yang, C. C. & Hsu, Y. L. A review of accelerometry-based wearable motion detectors for physical activity monitoring. *Sensors* **10**, 7772–7788 (2010).

32. Posatskiy, A. O. & Chau, T. The effects of motion artifact on mechanomyography: A comparative study of microphones and accelerometers. *J. Electromyogr. Kinesiol.* **22**, 320–324 (2012).

33. Maki, H., Ogawa, H., Matsuoka, S., Yonezawa, Y. & Caldwell, W. M. A daily living activity remote monitoring system for solitary elderly people. *Proc. Annu. Int. Conf. IEEE Eng. Med. Biol. Soc. EMBS* **2011**, 5608–5611 (2011).

34. Zheng, Y. L. *et al.* Unobtrusive sensing and wearable devices for health informatics. *IEEE Trans. Biomed. Eng.* **61**, 1538–1554 (2014).

35. Phan, D. H., Bonnet, S., Guillemaud, R., Castelli, E. & Thi, N. Y. P. Estimation of respiratory waveform and heart rate using an accelerometer. in *2008 30th Annual International Conference of the IEEE Engineering in Medicine and Biology Society* 4916–4919 (2008). doi:10.1109/IEMBS.2008.4650316

36. Vertens, J. *et al.* Measuring respiration and heart rate using two acceleration sensors on a fully embedded platform. in *icSPORTS 2015 - Proceedings of the 3rd International Congress on Sport Sciences Research and Technology Support* 15–23 (2015).

37. Sánchez Morillo, D., Ojeda, J. L. R., Foix, L. F. C. & Jiménez, A. L. An accelerometer-based device for sleep apnea screening. *IEEE Trans. Inf. Technol. Biomed.* **14**, 491–499 (2010).

38. He, D. Da, Winokur, E. S. & Sodini, C. G. An ear-worn continuous ballistocardiogram (BCG) sensor for cardiovascular monitoring. *Conf. Proc. IEEE Eng. Med. Biol. Soc.* **2012**, 5030–5033 (2012).

39. Rahman, T. *et al.* BodyBeat: A mobile system for sensing non-speech body sounds. *MobiSys 2014 - Proc. 12th Annu. Int. Conf. Mob. Syst. Appl. Serv.* 2–13 (2014). doi:10.1145/2594368.2594386

40. Kim, D. H. *et al.* Epidermal electronics. *Science (80-.).* **333**, 838–843 (2011).

41. Jang, K. I. *et al.* Soft network composite materials with deterministic and bio-inspired designs. *Nat. Commun.* **6**, 6566 (2015).

42. Fan, J. A. *et al.* Fractal design concepts for stretchable electronics. *Nat. Commun.* **5**, 3266 (2014).

43. Kim, D. H. *et al.* Electronic sensor and actuator webs for large-area complex geometry cardiac mapping and therapy. *Proc. Natl. Acad. Sci. U. S. A.* **109**, 19910–19915 (2012).

44. Kim, D. H. *et al.* Materials and noncoplanar mesh designs for integrated circuits with linear elastic responses to extreme mechanical deformations. *Proc. Natl. Acad. Sci. U. S. A.* **105**, 18675–18680 (2008).

45. Ma, Y. *et al.* Soft Elastomers with Ionic Liquid-Filled Cavities as Strain Isolating Substrates for Wearable Electronics. *Small* **13**, (2017).

46. Wang, S. *et al.* Mechanics of epidermal electronics. *J. Appl. Mech. Trans. ASME* **79**, 031022 (2012).

47. Jiang, H., Sun, Y., Rogers, J. A. & Huang, Y. Post-buckling analysis for the precisely controlled buckling of thin film encapsulated by elastomeric substrates. *Int. J. Solids Struct.* **45**, 2014–2023 (2008).

48. Muroga, T., Ito, Y., Aoyagi, K., Yamamoto, Y. & Yokomizo, K. Rolled copper foil. (2009).

49. Schwindt, D. A., Wilhelm, K. P., Miller, D. L. & Maibach, H. I. Cumulative irritation in older and younger skin: A comparison. in *Acta Dermato-Venereologica* **78**, 279–283 (Williams & Wilkins Co, 1998).

50. Titze, I. R. & Martin, D. W. *Principles of Voice Production*. *The Journal of the Acoustical Society of America* **104**, (Prentice Hall, 1998).

51. Calvert, D. R. *Clinical Measurement of Speech and Voice*. *The Laryngoscope* **98**, (Singular Thomson Learning, 1988).

52. Wu, K. Gender recognition from speech. Part II: Fine analysis. *J. Acoust. Soc. Am.* **90**, 1841–1856 (1991).

53. Lin, S. J. *et al.* A Pilot Study on BSN-Based Ubiquitous Energy Expenditure Monitoring. in *2009 Sixth International Workshop on Wearable and Implantable Body Sensor Networks* 49–52 (IEEE Computer Society Press, 2009). doi:10.1109/BSN.2009.56

54. Jin, A., Yin, B., Morren, G., Duric, H. & Aarts, R. M. Performance evaluation of a tri-axial accelerometry-based respiration monitoring for ambient assisted living. in *Proceedings of the 31st Annual International Conference of the IEEE Engineering in Medicine and Biology Society: Engineering the Future of Biomedicine, EMBC 2009* 5677–5680 (2009). doi:10.1109/IEMBS.2009.5333116

55. Dash, S., Shelley, K. H., Silverman, D. G. & Chon, K. H. Estimation of respiratory rate from ECG, photoplethysmogram, and piezoelectric pulse transducer signals: A comparative study of time-frequency methods. *IEEE Trans. Biomed. Eng.* **57**, 1099–1107 (2010).

56. Chon, K. H., Dash, S. & Ju, K. Estimation of Respiratory Rate From Photoplethysmogram Data Using Time-Frequency Spectral Estimation. *IEEE Trans. Biomed. Eng.* **56**, 2054–2063 (2009).

57. Murray, R. M., Li, Z. & Shankar Sastry, S. *A mathematical introduction to robotic manipulation*. *A Mathematical Introduction to Robotic Manipulation* (CRC press, 2017). doi:10.1201/9781315136370

58. Berry, R. B. *et al.* AASM scoring manual updates for 2017 (version 2.4). *J. Clin. Sleep Med.* **13**, 665–666 (2017).

59. Watanabe, N., Reece, J. & Polus, B. I. Effects of body position on autonomic regulation of cardiovascular function in young, healthy adults. *Chiropr. Osteopat.* **15**, 19 (2007).

60. Toyota, S. & Amaki, Y. Hemodynamic evaluation of the prone position by transesophageal

echocardiography. *J. Clin. Anesth.* **10**, 32–35 (1998).

61. Pump, B., Talleruphuus, U., Christensen, N. J., Warberg, J. & Norsk, P. Effects of supine, prone, and lateral positions on cardiovascular and renal variables in humans. *Am. J. Physiol. - Regul. Integr. Comp. Physiol.* **283**, R174–R180 (2002).

62. Issa, F. G. & Sullivan, C. E. Upper airway closing pressures in snorers. *J. Appl. Physiol. Respir. Environ. Exerc. Physiol.* **57**, 528–535 (1984).

63. Aurégan, Y. & Depollier, C. Snoring: Linear stability analysis and in-vitro experiments. *J. Sound Vib.* **188**, 39–53 (1995).

64. Fajdiga, I. Snoring imaging could bernoulli explain it all? *Chest* **128**, 896–901 (2005).

65. Guan, W. *et al.* Clinical Characteristics of Coronavirus Disease 2019 in China. *N. Engl. J. Med.* **382**, 1708–1720 (2020).

66. Chow, E. J. *et al.* Symptom Screening at Illness Onset of Health Care Personnel With SARS-CoV-2 Infection in King County, Washington. *JAMA* **323**, 2087–2089 (2020).

67. Sterling, M., Rhee, H. & Bocko, M. Automated Cough Assessment on a Mobile Platform. *J. Med. Eng.* **2014**, (2014).

68. Kvapilova, L. *et al.* Continuous Sound Collection Using Smartphones and Machine Learning to Measure Cough. *Digit. biomarkers* **3**, 166–175 (2019).

69. Gopinathannair, R. & Olshansky, B. Management of tachycardia. *F1000Prime Rep.* **7**, 60 (2015).

70. Ma, Y. Relation between blood pressure and pulse wave velocity for human arteries. *PNAS* **115**, 11144–11149

71. Lee, K. *et al.* Mechano-acoustic sensing of physiological processes and body motions via a soft wireless device placed at the suprasternal notch. *Nat. Biomed. Eng.* **4**, 148–158 (2020).

72. Negård, N.-O., Schauer, T., Kauert, R. & Raisch, J. AN FES-ASSISTED GAIT TRAINING SYSTEM FOR HEMIPLEGIC STROKE PATIENTS BASED ON INERTIAL SENSORS. *IFAC Proc. Vol.* **39**, 315–320 (2006).

73. O'Keeffe, D. T., Gates, D. H. & Bonato, P. A Wearable Pelvic Sensor Design for Drop Foot Treatment in Post-Stroke Patients. in *2007 29th Annual International Conference of the IEEE Engineering in Medicine and Biology Society* 1820–1823 (2007). doi:10.1109/IEMBS.2007.4352667

74. Santos, S., Venema, B. & Leonhardt, S. Accelerometer-assisted PPG measurement during physical exercise using the LAVIMO sensor system. *Acta Polytech.* **52**, 80–85 (2012).

75. Pollreisz, D. & TaheriNejad, N. Detection and Removal of Motion Artifacts in PPG Signals. *Mob. Networks Appl.* (2019). doi:10.1007/s11036-019-01323-6

76. Wójcikowski, M. & Pankiewicz, B. Photoplethysmographic Time-Domain Heart Rate Measurement Algorithm for Resource-Constrained Wearable Devices and its Implementation. *Sensors (Basel).* **20**, 1783 (2020).

77. Pielka, M. *et al.* A rehabilitation system for monitoring torso movements using an inertial sensor. in *2019 Signal Processing: Algorithms, Architectures, Arrangements, and Applications (SPA)* 158–163 (2019). doi:10.23919/SPA.2019.8936790

78. Wheeler, D. S., Wong, H. R. & Shanley, T. P. *Pediatric critical care medicine : basic science and clinical evidence*. (Springer).

79. Xu, J., Murphy, S. L., Kochanek, K. D., Bastian, B. & Arias, E. Deaths: final data for 2016. *Natl. Vital Stat. Rep* **67**, 1–76

80. Bonner, O., Beardsall, K., Crilly, N. & Lasenby, J. There were more wires than him': the potential for wireless patient monitoring in neonatal intensive care. *BMJ Innov* **3**, 12–18

81. Bowdle, T. A. Complications of invasive monitoring. *Anesth. Clin* **N. A. 20**, 571–588

82. Scheer, B., Perel, A. & Pfeiffer, U. J. Clinical review: complications and risk factors of peripheral arterial catheters used for haemodynamic monitoring in anaesthesia and intensive care medicine. *Crit. Care* **6**, 199–204

83. Shwayder, T. & Akland, T. Neonatal skin barrier: structure, function, and disorders. *Dermatol. Ther* **18**, 87–103

84. Mutashar, S., Hannan, M., Samad, S. & Hussain, A. Analysis and optimization of spiral circular inductive coupling link for bio-implanted applications on air and within human tissue. *Sensors* **14**, 11522–11541

7. Appendix

I. Effect of conformal contact in signal transmission.

The conformal contact reduces the air-gap and delamination points in the skin device interface and enhances the signal transmission.

Speed of sound is:

$$\mathrm{v} = \sqrt{\frac{K}{\rho}} \tag{A.1}$$

where v, K, ρ is speed of sound, bulk modulus, density, acoustic impedance, reflection coefficient, transmittance coefficient.

Acoustic impedance of a material is:

$$\mathrm{Z} = \rho \mathrm{v} \tag{A.2}$$

By substituting equation A.1 to A.2, we obtain the expression of impedance in terms of material property:

$$\mathrm{Z} = \sqrt{K\rho} \tag{A.3}$$

The reflection coefficient of the acoustic wave at the interface between two materials is:

$$R = \left(\frac{\mathrm{Z}_2 - \mathrm{Z}_1}{Z_2 + Z_1}\right)^2 \tag{A.4}$$

and thus, the transmission coefficient is:

$$T = 1 - \mathrm{R} \tag{A.5}$$

Equation A.4 and A.5 tell us that the materials with close impedance make the acoustic signal transmission between the two bodies more effectively.

The skin has a wide range of bulk modulus: {53 kPa, 178 kPa, 1280 kPa }, and density of 1050 kg/m^3, whereas air has a bulk modulus of 142 kPa and density of 1.23 kg/m^3. As a result, two material has a high mismatch in the impedance. With the conformal contact, the silicone elastomer is in direct contact with the skin without any air gap trapped between the devices. The elastomer has a bulk modulus of 1000 kPa and a density of 1070 kg/m^3. With the conformal contact, we can improve the impedance matching between the device and the materials and improve the signal fidelity.